BIOCORROSION OF COPPER BY *OLEIDESULFOVIBRIO ALASKENSIS* G20 BIOFILMS IN STATIC AND DYNAMIC ENVIRONMENTS

by

Yagmur Keskin

A thesis submitted in partial fulfillment
of the requirements for the degree

of

Master of Science

in

Chemical Engineering

MONTANA STATE UNIVERSITY
Bozeman, Montana

January 2024

©COPYRIGHT

by

Yagmur Keskin

2024

All Rights Reserved

DEDICATION

I dedicate my thesis to my grandfather Bayram, whose wisdom will always help me stay strong; my parents Ayten and Veda, who have been unconditionally supportive in my endeavors.

ACKNOWLEDGEMENTS

First, I want to express my sincere gratitude to my advisor, Professor Brent Peyton, for his invaluable advice, constant support, and patience without which I could not have completed this dissertation. His immense knowledge and plentiful experience have encouraged me in all the time of my academic research and daily life.

I am deeply thankful to my co-advisor, Professor Matthew Fields for being very patient and supportive and for the time that he spent discussing the various aspects of this thesis. I consider myself to be extremely privileged to have been his student.

I would like to thank the other committee member Associate Professor Abbie Richards, who generously provided her knowledge and expertise to complete my graduate degree.
I would like to thank Dr. Chiachi Hwang, who carefully taught me how to culture anaerobes in the early days of my graduate studies and later. Special thanks to MSc Bret Davis from Imaging and Chemical Analysis Laboratory who patiently guided me in using Field Emission Scanning Electron Microscopy and helped me develop the pitting measurement technique using X-Ray attenuation. I also appreciate the time that Professor Recep Avci has spent in helping me with explaining the fundamentals of how Electron dispersion X-Ray works and fixing the problems that I had in measuring pit depths. I would like to thank to Ph.D Candidate Amit Acharjee for carefully preparing the copper coupons used in the static experiments and bringing his expertise in material science aspects to chapter 3.

I would like to thank to all my friends and lab mates from Peyton & Fields Lab.

TABLE OF CONTENTS

1. INTRODUCTION 1

Project Rationale 1
Background 2
Sulfate Reducing Bacteria 5
Discovery and Classification of Sulfate-Reducing Bacteria 6
Oleidesulfovibrio alaskensis G20 7
Microbiologically Influenced Corrosion of Copper by SRB 8
Why Copper? 11
Copper Toxicity and Sulfate-Reducing Bacteria (SRB) Biofilm Forms on Copper 12
Desulfovibrio alaskensis G20 Biofilms and Metal Interaction 13
Recent Strategies to Prevent Microbiologically Influenced Corrosion of Copper 14
1.Protective Coatings 14
2.Biocides and Corrosion Inhibitors 16
3.Cathodic Protection Techniques 17
4.Monitoring and Control 18

2. COPPER TOXICITY TO OLEIDESULFOVIBRIO ALASKENSIS IN THREE DISTINCT MEDIA 20

Description of Study 20
Experimental Methods 21
Growth Conditions and Batch Exposure 21
Copper Concentration Adjustments 22
Inoculum and Growth of Oleidesulfovibrio alaskensis G20 22
Quantification Copper Toxicity and Growth Kinetics of *Oleidesulfovibrio alaskensis* G20 23
Results and Discussion 25
Microbial Growth 25
Quantification of Copper Toxicity of *Oleidesulfovibrio alaskensis* G20 in LS4D - BAL 29
Quantification of Copper Toxicity of *Oleidesulfovibrio alaskensis* G20 in LS4D – EAL 31
Quantification of Copper Toxicity of *Oleidesulfovibrio alaskensis* G20 in LS4D – EDL 34
K_i Measurements 36
Conclusion 40

TABLE OF CONTENTS CONTINUED

3. EFFECTS OF SURFACE ROUGHNESS ON MICROBIOLOGICALLY INFLUENCED CORROSION (MIC) OF COPPER 101 BY OLEIDESULFOVIBRIO ALASKENSIS G20 41

Contribution of Authors and Co-Authors 41
Abstract 43
Introduction 43
Materials and Methods 47
Preparation of Copper Coupons 47
Inoculum Preparation and Batch Exposure 48
Coupon Harvesting 49
Protein and Carbohydrate Assays 50
Surface Analysis, Determination of Pit Depth and Mineral Layer Composition 50
Results 51
Optical Profilometry 51
Microbial Growth 52
FE-SEM analyses 56
XRD Analysis 60
Corrosion Rates 62
Pit Depth Evaluation 65
Discussion 67
Mineral Layer Development and Corroded Surface Morphology 67
3 µm Diamond Suspension Finish. 68
400 US Grit Finishing. 70
600 US Grit and 800 US Grit Finishing 71
Mineral Layer Composition 73
Conclusions 73
Credit Authorship Contribution Statement 75
Declaration of Competing Interest 75
Acknowledgements 75
References 76

4. RESPONSE OF OLEIDESIULFOVIBRIO ALASKENSIS BIOFILM GROWN ON COPPER (101) IN A DYNAMIC ENVIRONMENT 81

Description of Study 81
Experimental Methods 82
Reactor Set-up 82
Inoculum of Oleidesulfovibrio alaskensis G20 83
Biofilm and Coupons Harvesting 83
Preparation of Samples for Imaging 84

TABLE OF CONTENTS CONTINUED

Growth Parameter Measurements 85
Results and Discussion 85
Corrosion Rate and Pit Depth Analysis 90
Biofilm and Coupon Analysis Under FE-SEM 93
Conclusion 104

5. CONCLUSION 106

Project Outcomes 106
Copper Toxicity on Oleidesulfovibrio alaskensis G20 106
Effect of Surface Finishing on Microbiologically Influenced Corrosion of Copper 101 107
Response of *Oleidesulfovibrio alaskensis* Biofilms Grown on Copper (101) in CDC Reactors 108
Funding Acknowledgements 109

6. FUTURE WORK 110

Extended Duration Studies 110
Variation in Environmental Conditions 110
Different Bacterial Strains and Communities 111
Cu^{+2} as Corrosion Inhibitor or Nano Glass Coating 111
Genomic and Transcriptomic Analysis 111
Electrochemical Characterization 112
Advanced Imaging Techniques 112
Real-world Application Studies 112

REFERENCES CITED 114

APPENDICES 129

APPENDIX A: TABULATED DATA FROM COPPER TOXICITY 130

APPENDIX B: TABULATED PITTING ANALYSIS DATA FREFFECTS OF SURFACE ROUGHNESS ON MICROBIOLOGICALLY INFLUENCED CORROSION (MIC) OF COPPER (101) BY OLEIDESULFOVIBRIO ALASKENSIS G20 146

APPENDIX C:CU(II) DISSOLUTION TO BALCH TUBES AND CDC REACTORS 157

APPENDIX D: BIOINFORMATICS STUDY 160

LIST OF TABLES

Table Page

1. Table 2. 1: Results of copper effect on final cell density (OD_{600}), specific growth rate, doubling time(td) and the maximum specific growth rate of O.alaskensis in three distinct mediums (LS4D-BAL, EAL, EDL) in the presence of various copper concentrations. 26

2. Table 3. 1: Carbohydrate and protein contents in the suspension of Cu -free culture and for coupons prepared with different surface finish..... 54

3. Table 3. 2: Surface roughness of copper samples prepared with different surface finish. 55

4. Table 3. 3: Copper coupon corrosion rates calculated for different surface finish after biotic exposure to *O. alaskensis* G20 for 1 week. N is the number of samples tested per each surface finish, the "mean" is the average measured corrosion rate, "StDev" is the standard deviation and "95% CI" is the 95% confidence interval recorded for the as-received coupons and for each surface finish. 63

5. Table 3. 4: Tukey simultaneous tests for differences of means performed on the measured corrosion rates calculated for different surface finish after biotic exposure to *O. alaskensis* G20 for 1 week..... 64

6. Table 3. 5: Pit depth measurements performed on copper coupons with different surface finish after biotic exposure to *O. alaskensis* G20 for 1 week..... 65

7. Table 3. 6: Tukey simultaneous tests for differences of means performed on the pits' depth evaluated for different surface finish after biotic exposure to O. alaskensis G20 for 1 week 656

8. Table 4. 1: Copper coupon corrosion rates calculated after biotic and abiotic exposure to *O. alaskensis* for 7 days in CDC reactors. 90

9. Table 4. 2.: Pit depth measurements performed on copper coupons with copper (101) after biotic exposure to *O. alaskensis* G20 for 7 days in static and reactor conditions. 93

LIST OF TABLES CONTINUED

Table Page

10. Table A. 1: *Oleidesulfovibrio alaskensis* G20 cultures grown in LS4D BAL (60L:30S) in copper free tubes and in the presence of 6 µM copper ions (Cu^{+2}) for 7 days. 131

11. Table A.9: *Oleidesulfovibrio alaskensis* G20cultures grown in LS4D EDL (15L:50S) in the presence 24 µM tubes for 7 days 139

12. Table B. 1:The average of three pit depths for each pitting measurement for all coupons. 15050

13. Table B. 2: The maximum and average pit depths differed among the groups, as received (control), 400 US Grit, 600 US Grit, 800 US Grit, and fine 3-micron diamond polished. 15050

14. Table C. 1: The comparison of Cu(II) dissolution (µM), Surface area of the coupons (cm^2), volume of medium (mL), Protein/surface area of biofilms and protein content of planktonic cells from the static condition. 1599

LIST OF FIGURES

Figure Page

1. Figure1. 1: Schematic overview of Microbiology induced corrosion on copper metals caused by sulfate reducing bacteria in the presence of inorganic sulfate and hydrogen..... 10

2. Figure 2. 1:Experimental set-up for each distinct medium, balanced, electron acceptor, electron donor media in the presence of 6 µM, 12 µM, 16 µM, 24 µM of Cu(II) concentrations. 22

3. Figure 2. 2: Growth of *Oleidesulfovibrio alaskensis* G20 in balanced medium (30S:60L) in the presence of various copper concentrations: (a) control, Cu-free, (b) 6 µM Cu^{+2}, (c) 12 µM Cu^{+2}, (d) 16 µM Cu^{+2}, and (e) 24 µM Cu^{+2}, and based upon growth rate impacts a K_i of 13.1 µM is estimated under BAL growth conditions. 31

4. Figure 2. 3: Growth of *Oleidesulfovibrio alaskensis* in electron acceptor limited medium (50L:15S) in the presence of various copper concentrations: (a) control, Cu-free, (b) 6 µM Cu^{+2}, (c) 12 µM Cu^{+2}, (d) 16 µM Cu^{+2}, and (e) 24 µM Cu^{+2}, and based upon growth rate impacts a I_{50} of 13.9 µM was estimated under EAL growth conditions. 33

5. Figure 2. 4 Growth of *Oleidesulfovibrio alaskensis* G20 in electron donor limited medium (15L:50S) in the presence of various copper concentrations: (a) control, Cu-free, (b) 6 µM Cu^{+2}, (c) 12 µM Cu^{+2}, (d) 16 µM Cu^{+2}, and (e) 24 µM Cu^{+2}, and based upon growth rate impacts a I_{50} of 11.3 uM is estimated under the EDL growth condition..... 35

6. Figure 2. 5: Determination of K_i value in the EAL medium. Theoretical plot of the inverse of maximum specific growth rate (1/µ) in the presence of different copper concentrations in the batch cultures, 6 µM,12 µM,16, and 24 µM, and control, Cu-Free as a function of copper concentrations (Cu^{+2}). K_i of 12.19 µM was determined (R^2=0.75). 38

LIST OF FIGURES CONTINUED

Figure Page

7. Figure 3. 1: (a) Growth of *Oleidesulfovibrio alaskensis*, (b) copper ion [Cu^{+2}] dissolved concentration in the medium. Blue is the control (as received), brown is the 400 US grit, pink is the 600 US grit, yellow is 800 US grit polished, purple is the 3 µm diamond suspension copper dissolution (µM). 53

8. Figure 3. 2: 3D topography of copper samples prepared with different surface finish and corresponding distribution of asperities (a-a') as received, (b-b') 400 US grit, (c-c') 600 US grit (d-d') 800 US grit, (e-e') 3 µm diamond suspension polishing. 55

9. Figure 3. 3: FE-SEM imaging of coupon surface after abiotic exposure for 7 days to sterile and autoclaved LS4D media (a) As received, (b) 400 US grit, (c) 600 US grit, (d) 800 US grit and (e) 3µm diamond suspension finish. 58

10. Figure 3. 4: Mineral growth on different surface finish copper coupons after 1 week of batch exposure to *O. alaskensis* G20. as received (a), 400 US grit (b), 600 US grit (c), 800 US grit (d) 3 µm diamond suspension polishing (e)..... 59

11. Figure 3. 5: FE-SEM imaging of copper coupons cross sections after 1 week batch exposure to *O. alaskensis* G20 as received (a), 400 US grit (b), 600 US grit (c), 800 US grit (d) 3 µm diamond suspension (e) finish. 59

12. Figure 3. 6: Cross section morphology and EDX line scan date of as received (a) 400 US grit (b) 600 US grit (c) 800 US grit (d) and 3 µm diamond suspension (e) finished coupons after 1 week batch exposure to *O. alaskensis* G20..... 60

13. Figure 3. 7: FE-SEM imaging of as received (a) 400 US grit (b) 600 US grit (c) 800 US grit (d) and 3 µm diamond suspension (e) finished coupons after 1 week batch exposure to *O. alaskensis* G20 after removal of the mineral layer developed on the surface. 62

LIST OF FIGURES CONTINUED

Figure Page

14. Figure 3. 8: XRD spectra comparison for as received, 400 US grit, 600 US grit, 800 US grit and 3µm diamond suspension polished coupon surface after biotic exposure to *O. alaskensis* G20 for 1 week..... 67

15. Figure 4. 1: CDC CBR-90 Anaerobic Reactor design consisting of a sealed lid with gas and media inlet and outlet tubings, thermocouple probes, and Pyrex bowls, mounted on hotplates. The inside of the reactor consists of rods that held coupons and a centrally positioned magnet to facilitate media agitation.....83

16. Figure 4. 2: Images of copper coupons that have initially undergone sterilization and then inserted into the coupon holder inside a laminar flow hood (A), followed by the exposure of these coupons to O. alaskensis for a duration of 7 days (B), and the exposure of glass coupons to the bacterium for the same duration (C) 835

17. Figure 4. 3: The biofilm mass per cm^2 taken on day 7, day 9, and day 14 was shown in the columns, along with a 95% confidence range. 86

18. Figure 4. 4: Protein and hexose quantities of *O. alaskensis* biofilms cultivated on copper and glass coupons (µg/cm^2) with 95% CI throughout a period of 7, 9, and 14 days inside CDC reactors..... 87

19. Figure 4. 5:. The protein-to-surface area ratio (µg/cm2) was measured for three CDC reactors, as well as a control run (glass coupon) with % 95 confidience interval. For this experimental trial, identical inoculum and experimental settings were used, with four reactors being simultaneously operated. Note that the surface area of the copper was increased by a factor two (56.4 cm2) in comparison to the prior experiment in order to obtain more biomass for transcriptomic analysis. 89

20. Figure 4. 6: The SEM picture on the right shows the points at which EDX spectra were acquired in order to quantify the corrosion pit depths. The left image represents the outcome of MATLAB pit depth analyses. The integration of the EDX spectrums into MATLAB yielded a measurement of 4.7 microns of the pit. 93

LIST OF FIGURES CONTINUED

Figure Page

21. Figure 4. 7: SEM image of a coupon that has undergone abiotic exposure in a reactor for a duration of 7 days. 94

22. Figure 4. 8: SEM image of a coupon that has undergone abiotic exposure in a reactor for a duration of 9 days. 95

23. Figure 4. 9: SEM image of a coupon that has undergone abiotic exposure in a reactor for a duration of 14 days. 95

24. Figure 4. 10: SEM image of robust *O. alaskensis* biofilm generated 7-day exposure in CDC reactor. 96

25. Figure 4. 11: Biofilm jungle inside CDC reactors. The image shows a SEM picture of the robust growth of *O. alaskensis* biofilm on a coupon over a period of 7 days inside a CDC reactor, together with the corrosion products, Cu_2S, barely seen on the upper left and upper middle part of the picture. 96

26. Figure 4. 12: SEM image of robust *O. alaskensis* biofilm generated 9-day exposure in CDC reactor, together with the corrosion products, Cu_2S. 97

27. Figure 4. 13: SEM image of robust O. alaskensis biofilm generated on deposited corrosion products, Cu_2S for 14-day exposure in CDC reactor. 97

28. Figure 4. 14: SEM images (A) aggressive growth of O. alaskensis inside CDC reactor for 7 days, (B) a closer look of image A to robust *O. alaskensis* biofilm grown on Cu_2S mineral as corrosion byproducts. 98

29. Figure 4. 15: The image on the left (A) shows G20 biofilms developed on deposited corrosion products a copper surface (101) under static condition, whereas the image on the right (B) shows the biofilm produced on an identical copper surface (101) in a CDC reactor for a duration of 7 days. 99

LIST OF FIGURES CONTINUED

Figure Page

30. Figure 4. 16: Cells of *O. alaskensis* G20 grown on a copper coupon for duration of 7 days inside CDC reactor. 99

31. Figure 4. 17: Cells of *O. alaskensis* grown metal sulfide deposits on a glass coupon for a duration of 7 days inside a CDC reactor..... 100

32. Figure 4. 18: SEM image (A) shows copper coupon surface before the bacterial exposure, image (B) shows the copper surface 7-day bacterial exposure in the reactor and cleaned then sonicated it, soaked in 37% HCL..... 101

33. Figure 4. 19: SEM image (A) shows a localized pitting on the grain boundary at the end of 7 days exposure, (B) shows the diameter (3.023 μm) of the pit on the left image. 101

34. Figure 4. 20: SEM image of the wideness of intergranular corrosion measurements along with a crack on a copper coupon after 7-day exposure inside a CDC. 102

35. Figure A. 1: The exponential plots of growth (A) copper-free, (B) 6 μM of Cu(II) ions, (C) 12 μM of Cu(II) ions, (D) 16 μM of Cu(II) ions in LS4D-BAL medium. The cultures didn't show growth in the presence of 24 μM of Cu(II) ions in LS4D-BAL medium. $Y=Ae^{\mu x}$, each μ value refers to specific growth rate. 140

36. Figure A. 2: The exponential plots of growth of (A) copper-free, (B) 6 μM of Cu(II) ions, (C) 12 μM of Cu(II) ions, (D) 16 μM of Cu(II) ions and (E) 24 μM of Cu(II) ions in LS4D-EAL medium. $Y=Ae^{\mu x}$, each μ value refers to specific growth rate. 141

37. Figure A. 3: The exponential plots of growth of (A) copper-free, (B) 6 μM of Cu(II) ions, (C) 12 μM of Cu(II) ions, (D) 16 μM of Cu(II) ions and (E) 24 μM of Cu(II) ions in LS4D-EDL medium. $Y=Ae^{\mu x}$, each μ value refers to specific growth rate. 142

LIST OF FIGURES CONTINUED

Figure Page

38. Figure A. 4: The EDX chemical analysis of unfunctionalized surface of steel, control (A) and the functionalized surface (B) where the bacteria trapped to the surface. 1454

39. Figure A. 5: EDS layered image 1 (the unfunctionalized surface- control) and EDS layered image 2 (functionalized surface) show thick mat of biominerals including copper, zinc and iron (Images takend by Bret Davis and Dane Mansfield). 1445

40. Figure B. 1. Copper mass attenuation coefficients. 1499

41. Figure B. 2: (Left) image was captured from a as-recieved coupon. The brightness and contrast of this image were adjusted in order to identify the maximum pits, which are the darkest points in the center image. (Right) additionally, one of the pits was magnified to collect spectrums using EDX for further investigation of pitting. 15151

42. Figure C. 1: The dissolution of Cu(II) under abiotic static conditions was measured using two experimental setups: copper coupons with a total surface area of 1.52 cm2 and 15 mL medium tubes (A), and a CDC reactor with a total copper surface area of 25.2 cm2 and 400 mL medium (B). 158

43. Figure D. 1: AlgE on G20 membrane modelled using Pymol (left), AlgE on Pseudomonas aeruginosa membrane(right),..... 16161

ABSTRACT

This study presents a detailed examination of the intricate relationships between *Oleidesulfovibrio alaskensis* G20 and copper (101), emphasizing three interconnected perspectives: the kinetics of copper toxicity in three distinct media, the impact of surface finishing on microbiologically influenced corrosion (MIC), and the interaction of G20 biofilms and copper in CDC biofilm reactors. Initially, the study concentrates on the kinetic effects of copper toxicity on the growth of G20.

The research meticulously quantifies the detrimental impact of different copper (II) concentrations (6, 12, 16, and 24 μM) on bacterial growth kinetics in three media: LS4D balanced (BAL), electron acceptor-limited (EAL), and electron donor-limited (EDL). Using a non-competitive inhibition model, I_{50} (concentrations of copper causing 50% inhibition of bacterial growth) values were calculated to be 13.1, 13.87, and 11.31 μM for LS4D BAL, EAL, and EDL media, respectively.

The second part of the study shifts its focus to the effect of surface finishing on MIC of copper 101 by G20. The biofilm and corrosion pit depths were measured through a series of sophisticated analyses employing 3D optical profilometry, Scanning Electron Microscopy (SEM), Energy Dispersive X-Ray (EDX), and X-ray Diffraction Analysis (XRD). The research investigates how different levels of surface roughness, applied through metallographic grinding and polishing, influence corrosion. The findings demonstrate a clear pattern of both uniform and pitting corrosion across all surface finishes. Notably, a statistically significant decrease in corrosion rates was observed when the surface roughness of copper was altered from approximately 13μm to about 0.06μm.

Finally, the study explores the interaction between G20 biofilms and copper (101) into CDC reactors to understand biofilm development on copper surfaces and its subsequent impact on copper corrosion in a dynamic environment over periods of 7, 9, and 14 days. The results showed robust biofilm formation through hexose and protein analyses and SEM images displaying progressive increases in SRB cell accumulation over time. Localized pit depths were measured and compared to static conditions, and pits showed only a 20% increase in a dynamic environment. These findings offer an improved understanding of the complex interactions between G20 and MIC of copper.

CHAPTER ONE

INTRODUCTION

Project Rationale

MIC caused by sulfate-reducing bacteria (SRB) has been under investigation since 1934 when von Wolzogen Kühr and van der Vlugt identified SRB as the primary factor contributing to the extensive deterioration of iron pipes in the sulfate-rich soils of North Holland (Dennis & Garrelfs, 2014). Since then, numerous studies have been conducted to investigate the effects of SRB on corrosion in various materials, including carbon steel, iron, and copper. These studies have explored the growth characteristics of SRB, the impact of SRB biofilms on corrosion behavior, and the mechanisms underlying SRB-induced corrosion (Liu, et al., 2020; Sykopra, et al., 2020; Fatah, et al., 2019; Zhang, et al., 2023; Liu, et al., 2009; King, et al., 2013). Copper has been an essential metal for humans since prehistoric times due to its malleability, electrical and thermal conductivity, and antimicrobial properties. Copper and its many alloys have played a vital part in numerous civilizations, ranging from the ancient Egyptians to the Romans to modern-day societies all across the globe (Odler, et al., 2021).

Effective protection strategies must be implemented to reduce metal corrosion in the industry: new technologies must be developed to increase the practicality of manufacturing copper.

Over the course of the last decade, significant research has been conducted on understanding the interaction between copper metal surfaces and SRB biofilms, the response of

SRB to copper toxicity and copper surfaces mostly in stagnant environments (Javaherdashti & Akvan, 2019).

The work described herein contributes to ongoing research aimed at investigating MIC on copper surfaces and the impacts of surface roughness of copper metal in the presence of SRB. Further, the results presented here will increase the understanding of the initial biofilm-metal interactions in stagnant and dynamic environments. The scope of work here focuses on the following:

1. Copper toxicity kinetics to *Oleidesulfovibrio alaskensis* G20 in three distinct media.
2. Effects of surface roughness on microbiologically influenced corrosion of copper (101) by *Oleidesulfovibrio alaskensis* G20.
3. Interaction between *Oleidesulfovibrio alaskensis* G20 biofilms and copper (101) in flow through systems.

Background

Corrosion is a naturally occurring process that is typically characterized as the degradation of a metal surface or its qualities as a result of a response to its surrounding environment. Mainly it is an electrochemical process. An oxidation reaction occurs during this process, in which a metal (M) is reduced to M^+ and electrons are lost (Lower, 2023). Corrosion, like other natural disasters such as earthquakes or extreme weather, may cause harmful and costly damage to anything from vehicles, household appliances, and drinking water systems to pipelines, bridges, and public structures. Between 1980 and 2001, The United States has had 52 significant weather-related catastrophes, including hurricanes, tornadoes, tropical storms, floods, fires, droughts, and freezes, resulting in total normalized losses of more than $380 billion, an

average of $17 billion per year (Koch, et al., 2016). According to the most recent corrosion research in the United States, the yearly direct cost of metallic corrosion is $276 billion (Koch, et al., 2016). This amounts to 3.1% of the US Gross Domestic Product (GDP). The general assumption is that MIC contributes to 20% of total corrosion expenses, which equates to $55 billion in the United States each year. The total cost of corrosion is estimated to be 451,300$ billion, which is equivalent to 2.7% of the US GDP in 2013 (Koch, et al., 2016; Koch, et al., 2002) Significant improvements have been achieved in the field of corrosion prevention since the 1980s. Nevertheless, a continuing absence of efficient strategies to combat MIC continues to inflict detrimental consequences on the environment (Koch, et al., 2016).

Microbiologically influenced corrosion is often defined as the process of corrosion induced by the presence and metabolic activities of microorganisms. Microbial species, including bacteria and fungi, frequently generate biofilms on metallic surfaces, leading to the alteration of the metal surface and the present environment via the production of chemical compounds. Various studies have shown the presence of acid-producing bacteria, sulfate-reducing bacteria, and iron-reducing bacteria in drinking water, fuel transportation systems, and infrastructure where they are known to interact with metals (Zhu, et al., 2003; Muthukumar, et al., 2003). However, the major group is sulfate-reducing bacteria (SRB), whose anaerobic metabolism can result in corrosive metabolites and electrochemical conditions that induce MIC. The occurrence of chemical transformations may facilitate the development of localized attacks, resulting to the formation of pits and the process of dealloying. Additionally, these chemical changes may aggravate the phenomena of stress corrosion cracking, erosion corrosion, and hydrogen embrittlement. (Muthukumar, et al., 2003; Lane, 2005). Although MIC and non-microbial

corrosion are distinct phenomena, their fundamental mechanisms often display in common. As a result, the characteristics that explicitly establish corrosion as MIC lack adequate definition. The topic of MIC in water transportation, infrastructure, sewer systems, and oil-gas pipelines is a highly intricate subject that is influenced by several factors. These factors include the presence and characteristics of microbes, such as the type of bacteria and their activity, as well as the material composition, liquid chemistry, and the system's susceptibility to biocontamination. Due to the complex nature of the phenomenon, MIC is sometimes used as a comprehensive term to elucidate corrosion occurrences that are challenging to comprehend after all other explanations (Little & Lee, Microbiologically Influenced Corrosion, 2009) . Moreover, the origins and mechanisms of MIC lack clear understanding due to the prioritization of practical research over basic research. Practical research mostly focuses on diagnosing and addressing particular issues, leaving the fundamental aspects of MIC relatively unexplored. The lack of comprehensive study and agreement about the prevalence of MIC in the United States and worldwide creates uncertainty regarding the extent of the problem and the potential underreporting of instances. The underreporting of MIC may occur due to various factors. These include the deliberate withholding of information by corporations or government organizations, the decision of maintainers to not report MIC incidents due to perceiving it as a "hygiene issue" and wanting to avoid drawing attention or potential consequences from regulatory authorities, insufficient resources or qualified personnel to effectively investigate and document MIC occurrences (Mansfield & Sowards, 2015). Significant infrastructure failures brought on by MIC have been documented such as the 2006 Alaska pipeline disaster (Gu, 2012; Mansfield & Sowards, 2015), but minor occurrences that are less expensive, smaller in scope, or less well known may not

always be documented. Based on this information, MIC could potentially be more than 20% of the total corrosion and cost more than the amount, $ 55 billion. Thus, it makes the situation even worse than we anticipate.

While efforts can be made to control and mitigate MIC, complete control may not always be achievable due to the complex and dynamic nature of microbial communities and the environmental factors that influence their activity. Implementing preventive measures and adopting proactive maintenance practices are key strategies to minimize the impact of MIC in water sewer infrastructure and other affected systems. In recent years, effective protection strategies have been developed to avoid severe consequences of bio-corrosion (Javed, 2016).

The major group is sulfate-reducing bacteria, whose anaerobic metabolism can result in corrosive metabolites and electrochemical conditions that induce MIC. *O. alaskensis* G20 is in SRB group accelerating corrosion on metal surfaces. Although copper is known as antibacterial properties, *O. alaskensis* G20 overcomes copper toxicity and thrives on copper surfaces (Little & Lee, Microbiologically Influenced Corrosion, 2009).

Sulfate Reducing Bacteria

Sulfate-reducing bacteria (SRB) have played a significant role in shaping the Earth's biogeochemical cycles for billions of years. SRBs are a diverse group of microorganisms that reduce sulfate to hydrogen sulfide (H_2S) as part of their anaerobic respiration process. These bacteria have been present on Earth for at least 3.5 billion years, playing a critical role in shaping the planet's biogeochemical cycles, including the sulfur, carbon, and nitrogen cycles (Canfiel, et al., 2006).

The presence of sulfur isotope fractionation in ancient rock formations suggests that SRB was responsible for the early sulfur cycle, which contributed to the formation of the first continents (Sani, et al., 2001). The emergence of SRB is thought to have been an essential step in the evolution of life, as these bacteria played a crucial role in maintaining the redox balance of Earth's early oceans (Canfield & Teske, 1996).

Discovery and Classification of Sulfate-Reducing Bacteria

The discovery of SRB can be traced back to the 19th century when German scientist Christian Gottfried Ehrenberg first observed microorganisms capable of producing hydrogen sulfide from sulfate (Fernandez, Rua, Reyes, Cammack, & Hatchikian, 1989). However, it was not until 1895 that Martinus Beijerinck isolated and described the first SRB, *Spirillum desulfurica*ns and probably *Desulfovibrio vulgaris* strain *Hildenburg* has been researched the most in MIC related studies (Rickard, 2012; Muyzer & Stams, 2008).

SRB are now classified within the domain bacteria, with representatives in several phyla, such as *Proteobacteria, Firmicutes, Nitrospirae*, and *Thermodesulfobacteria* [25] and later study showed that SRB are classified into the phylum Firmicutes and the class Deltaproteobacteria based on their 16S rRNA gene sequences (Rabus, et al., 2013). However, recent genomic studies have revealed that SRB form a polyphyletic group, comprising at least four distinct clades: *Desulfovibrio, Desulfobacteraceae, Desulfobulbaceae*, and *Syntrophobacteraceae* (Kuever, 2014). These clades differ in their metabolic capabilities, physiological characteristics, and ecological preferences. For example, *Desulfovibrio* spp. are versatile SRB that can utilize a wide range of organic substrates as electron donors, while *Desulfobacteraceae* and *Desulfobulbaceae*

are specialized in utilizing specific substrates, such as fatty acids and alcohols, respectively (Kuever, 2014).

Although these bacteria share the ability to reduce sulfate, they exhibit a wide range of physiological and metabolic characteristics, which allows them to inhabit diverse environments, from marine sediments, hot springs, deep-sea hydrothermal vents to the intestinal tracts of animals. In marine sediments, SRB can be found in the upper layers of the sediment, where oxygen is depleted, and sulfate becomes the dominant electron acceptor (Rabus, et al., 2013). They also play a vital role in the sulfur cycle of freshwater ecosystems, where they participate in the anaerobic decomposition of organic matter (Müller, et al., 2015). In addition, SRBs are present in the gut microbiome of animals, where they contribute to the digestion of complex polysaccharides and the synthesis of essential amino acids (Rey, et al., 2010).

Oleidesulfovibrio alaskensis G20

Oleidesulfovibrio alaskensis G20, formerly known as *Oleidesulfovibrio desulfuricans G20*, was isolated from an oil well in Ventura County, California (Wall, et al., 1993). It is a member of SRB that has been extensively studied due to its role in biocorrosion, bioremediation, and its versatile metabolic capabilities (Mehta-Kolte, et al., 2019).

The genome of *O. alaskensis* G20 has been sequenced and annotated, providing valuable insights into its genetic makeup and metabolic potential. Comparative genomics studies have revealed similarities and differences between *O. alaskensis* G20 and other *Desulfovibrio* species, such as *D. vulgaris Hildenborough* (Keller, et al., 2014). The presence of transposon mutants and fitness profiling techniques has allowed researchers to investigate the genetic basis of various traits and stress responses in *O. alaskensis* G20. These studies have revealed that the molecular

mechanisms underlying nitrate stress responses and energy conservation in this bacterium (Korte, et al., 2014). Also, *O. alaskensis* G20 has been shown to have a wide range of metabolic capabilities, including the ability to corrode metals, reduce toxic metals, and participate in the sulfur and carbon cycles (Mehta-Kolte, et al., 2019). It has also been studied for its hydrogen sulfide production and its involvement in the taurine desulfonation pathway. A novel glycyl radical enzyme, which catalyzes the cleavage of isethionate into sulfite and acetaldehyde, ultimately leading to H_2S production, is identified (Peck, et al., 2019). The bacterium's lipid composition and hydrogen isotope fractionation have been investigated, providing insights into its energy metabolism and environmental interactions (Leavitt, et al., 2016). The origin and isolation of *O. alaskensis* G20 from an oil well highlight its adaptation to extreme environments and its potential applications in bioremediation and bioenergy production (Mehta-Kolte, et al., 2019). The availability of a large collection of mutants for this strain has facilitated genetic studies and the exploration of its energy metabolism (Price, et al., 2014).

Microbiologically Influenced Corrosion of Copper by SRB

Previously, there has been an assumption that the interplay between bacteria and metallic surfaces always leads to elevated levels of corrosion activity. MIC typically refers to the phenomenon whereby the corrosion rates are heightened as a result of bacterial presence, leading to an acceleration of both the anodic and/or cathodic corrosion reactions, but the underlying corrosion mechanism remains relatively unaltered. Copper and its alloys are often used in water distribution and pipe systems, heat exchangers, intake screens, splash zone sheathing, offshore buildings, chiller systems, and fire sprinkler systems (Little, et al., 2009; Little, et al., 1996). Copper corrosion in aqueous systems is highly dependent on the physico-chemical

characteristics of the water, such as pH, oxygenation level, and the presence of specific anions like carbonate, chloride, sulfate, or iron cations. It has been reported that, regardless of the composition of the alloy, bacteria would colonize on copper alloys exposed to natural seawater in only three weeks (Mansfeld & Little, 1992). Copper alloys' vulnerability to MIC-induced pitting and crevice corrosion was also demonstrated in a number of investigations (Little, et al., The Impact of Sulfate-Reducing Bacteria on Welded Copper-Nickel Seawater Piping Systems, 1988). Intergranular and/or pitting corrosion attack is caused by the disintegration and loss of the surface film, the formation of pits, and the heterogeneity of the local environment created by the biofilm (Huang, et al., 2004).

Despite having generally strong antibacterial and corrosion resistance, copper and its alloys are susceptible to MIC. MIC includes a close look of sulfate-reducing bacteria, which are ubiquitously present in various aquatic environments and soils and utilizing sulfate as a terminal electron acceptor, producing sulfide as a byproduct in the presence of organic substances or hydrogen (Barton & Fauque, 2009). MIC has been documented in several sectors such as chemical processing, oil and gas, and power production, sea water piping systems, occurring under diverse environmental conditions copper corrosion, specifically in the presence of sulfate-reducing bacteria, poses significant challenges and they are notorious for their role in microbial corrosion (Venzlaff, et al., 2013). Metal cation enhances metal surface anodic dissolution via cathodic depolarization. According to various research findings, copper is sensitive to a broad spectrum of exopolymers, including those generated by SRB biofilm-forming bacteria that colonize copper surfaces (Javed, 2016).

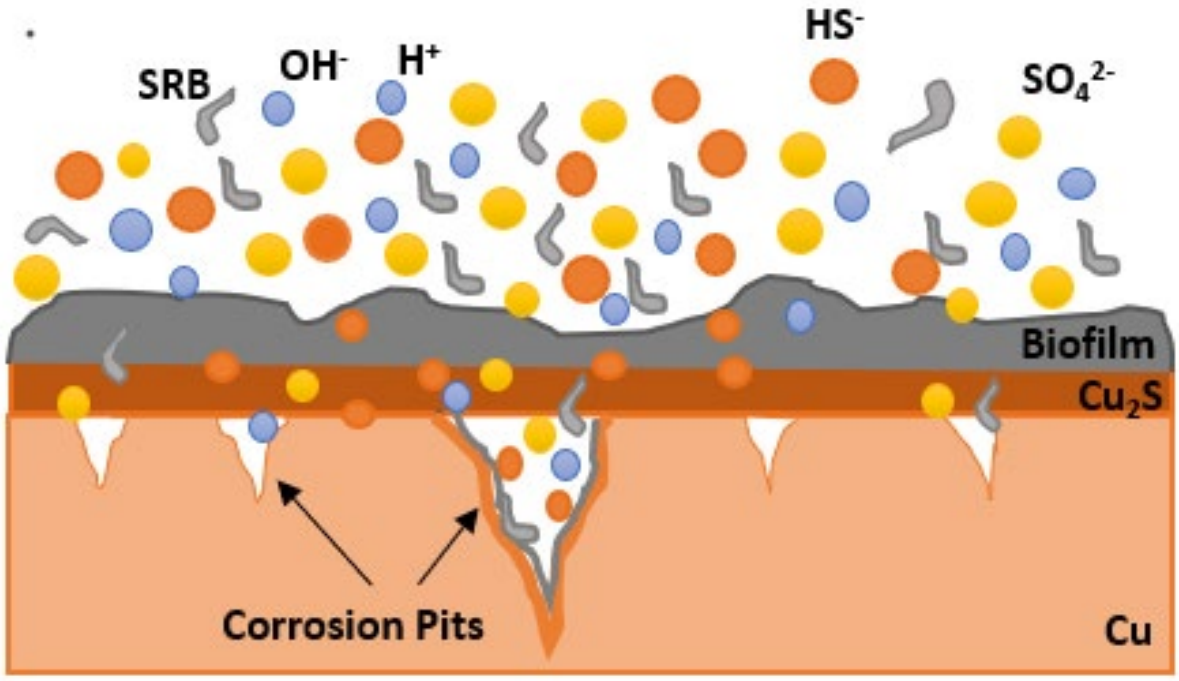


Figure1. 1: Schematic overview of Microbiology induced corrosion on copper metals caused by sulfate reducing bacteria in the presence of inorganic sulfate and hydrogen.

The corrosion process initiated by SRB generally begins when the bacteria attach to the metal surface and form a biofilm (Enning & Garrels, 2014). The produced sulfide, in the presence of water, can react with copper to form copper sulfide (Cu_2S). The general chemical reaction can be written as follows (Amendola & Acharjee, 2022):

$$2Cu\ (s) + H_2S\ (g) \rightarrow Cu_2S\ (s) + H_2\ (g)$$

This reaction leads to the dissolution of copper into the surrounding environment and the formation of copper sulfide on the surface, which is one of the primary mechanisms of corrosion damage caused by SRB.

At the anode, copper donates electrons, undergoing oxidation to form copper ions (Cu^+) that dissolve into the surrounding medium:

$$2Cu\ (s) \rightarrow Cu^{+} + 2e^{-}$$

This oxidation reaction is facilitated by the corrosive environment created by SRB and their metabolic byproducts (Mansfield & Sowards, 2015).

The cathodic reaction, which is associated with the generation of SRB, is considered to be an indirect process. This is because the ultimate metabolic product generated is HS, which then reacts with H^{+} to yield H_2S. The following reactions between copper and H_2S were previously identified as thermodynamically favorable (Bard, 1986; Puigdomenech, 2000)

$$HS^{-} + H^{+} + 2e^{-} \rightarrow S^{2-} + H_2$$

However, an intermediate product, $Cu(SH)_{ads}$ adsorbs on the Cu surface before the formation of Cu_2S as follows (J. Chen, 2017)

$$Cu^{+} + HS^{-} \rightarrow Cu(HS)_{ads} + e^{-}$$

$$Cu + Cu(HS)_{ads} + SH^{-} \rightarrow Cu_2S + H_2S + e^{-}$$

It's important to note that the corrosion process is not merely a chemical process but a complex interplay between biological and chemical mechanisms. For instance, the extracellular polymeric substances (EPS) produced by the SRB can enhance biofilm stability and interact with copper ions, accelerating their removal from the metal surface (Flemming, 2010).

Why Copper?

Ever since man's earliest days, copper has been one of the most important materials in his toolkit. In point of fact, one of the most important "ages" or phases in the progression of human history is called bronze, after a copper alloy. Copper and the various alloys that may be made from it have been very useful to several cultures throughout history, from the ancient Egyptians and Romans to the cultures of today all over the globe (Metals, 2022). Copper is one of the

metals that has been used for the longest amount of time and has been recognized as an essential component in the development of civilization. Copper has become an important industrial metal, ranking third behind iron and aluminum in terms of the quantity of metal that is consumed. Copper's features of high ductility, malleability, thermal and electrical conductivity, antimicrobial property and resistance to corrosion have contributed to copper's rise to prominence in the industrial sector (Flanagan, 2023). The majority of publications discuss the use of copper materials in various water systems. These systems include drinking water systems, marine and fluvial biofouling control, cooling systems, and wastewater treatment. The respective percentages of copper usage in these systems are 56%, 21%, 21%, 11%, and 3% (Gomes, et al., 2020). The use of copper as a material with antibacterial and/or antibiofilm characteristics in the field of healthcare and (bio)medical devices has been seeing a notable upward trend. Furthermore, the use of copper materials in membrane systems, such as reverse osmosis membranes, and dental care procedures has been subject to attention by the scientific community. However, these areas of research have been researched to a lesser degree, accounting for just 5% and 7% of the published works, respectively. The remaining 7% of the original research focused on various industries, including the petrochemical industry (1.7%) (Kalajahi, 2020), the building sector specifically connected to bricks (1.7%), food contacting surfaces (1.7%) and materials used in space travel (Gámez-Espinosa, et al., 2020; Gomes, et al., 2020).

Copper Toxicity and Sulfate-Reducing Bacteria (SRB) Biofilm Forms on Copper

The cultures of sulfur-reducing bacteria are shielded from the detrimental impacts of heavy metals due to the sulfide generated by their metabolic processes (Temple & Le Roux, 1964). The negative implications of copper toxicity on various forms of life are well-

documented. We know that copper toxicity can impede the growth and metabolic functions of SRB. Copper ions interfere with essential enzymatic activities, leading to the disruption of bacterial cell structure and function (Xie, et al., 2019). By deactivating enzymes, denaturing proteins, and competing with essential cations, heavy metals have a negative effect on bacterial communities (Syed, et al., 2021). Several factors influence the impact of dissolved metals. Binding to environmental constituents, interactions with ions, biosorption, and biotransformations are more likely to reduce the toxicity of metals (Babich & Stotzky, 1985).

Copper toxicity on biofilms, which are aggregates of microorganisms embedded within a self-produced matrix, exhibit different responses to copper compared to planktonic cells. Biofilms can resist copper toxicity due to their unique structure and the presence of extracellular polymeric substances which can bind and sequester copper ions, reducing their bioavailability (Harrison, et al., 2007). The impact of copper toxicity on SRB biofilms can, therefore, have implications for corrosion processes. Copper toxicity can hinder the growth and metabolism of SRB, potentially reducing the extent of MIC. However, the protective mechanisms of SRB biofilms, including metal sequestration by EPS, could counteract this effect (Harrison, et al., 2007; Sani, et al., 2001). The adaptation of SRB to contaminated environments could potentially help adapt to toxic copper environments.

Desulfovibrio alaskensis G20 Biofilms and Metal Interaction

Although the electron-transfer theory provides the most elegant explanation of MIC to yet, it ignores the potential that the organic part of the biofilm matrix may actually facilitate electron transfer from the metal to an electron acceptor like oxygen. Cathodic reactions may be catalyzed by a variety of substances, including metal ions bound by bacterial extracellular

polymeric substances and enzymes functioning inside the biofilm matrix. The biocorrosion process is expected to be influenced by both processes (Beech, et al., 2005).

The production of extracellular polymeric substances, which include macromolecules such as proteins, polysaccharides, nucleic acids, and lipids, promotes. The binding of metal ions by EPS requires an interaction with anionic functional groups, such as carboxyl, phosphate, sulfate, glycerate, pyruvate, and succinate groups (Roy, et al., 2022). The previously mentioned functional groups are often seen on the carbohydrates and proteins that form exopolymers. EPS also plays an important role in the maintenance of a biofilm. The extracellular polymeric substances to bind metal ions is fundamental to the determination of MIC and is dependent not only on the species of bacteria but also on the type of metal ion. (Kinzler, et al., 2003)

The binding strength of multidentate anionic ligands towards ions such as Ca^{2+}, Cu^{2+}, Mg^{2+}, and Fe^{3+} exhibits significant importance. Major shifts in the standard reduction potentials may arise due to the existence of metal ions in different oxidation states within the biofilm matrix, with the affinity shown towards these metal ions (Beech & Sunner, 2004).

Recent Strategies to Prevent Microbiologically Influenced Corrosion of Copper

1.Protective Coatings

The use of protective coatings, such as epoxy or polyurethane coatings, may provide a physical barrier between the metal surface and the corrosive environment. The potential of graphene as a coating material for protecting metals has been the subject of much research, owing to its exceptional ability to prevent the permeability of gases, vapors, and liquids (Ollik & Lieder, 2020). Nevertheless, it has been discovered that the presence of graphene might facilitate the process of metal corrosion. In order to tackle this issue, scholarly investigations have

prioritized the suppression of the corrosion-promoting characteristics shown by graphene. The integration of nanosized silicon oxide (SiO_2) into graphene has been seen to augment its resistance to corrosion by impeding the interaction between graphene and metal substrates (Wen, et al., 2015) . The incorporation of graphene into polymers, such as polyaniline, has shown enhanced corrosion inhibition capability and heightened adhesive strength of the coating on metallic substrates (Singhbabu, et al., 2015).

Graphene has been used as an additive in epoxy resin and polyurethane coatings to augment their corrosion resistance. The incorporation of reduced graphene oxide (rGO) into the epoxy resin primer has been seen as fixing the porosity in the coating, resulting in improved corrosion resistance (Wang & Cai, 2020).

The efficacy of graphene in preventing the corrosion of copper surfaces in various biological aquatic conditions has been established. The findings obtained from the cell viability experiments indicate that the presence of graphene significantly mitigates the harmful effects of copper by impeding corrosion processes and diminishing the production of Cu^{2+} ions (Zhang, et al., 2014).

A possible approach involves the production of superhydrophobic coatings, which have the ability to inhibit corrosion by maintaining air between corrosive fluids and solid surfaces. These coatings have an excellent ability for corrosion resistance and a low level of corrosion density, making them well-suited for the purpose of protecting industrial metals. Superhydrophobic surfaces composed of corrosion-resistant alloys, such as Zn-Ni and Zn-Co, have been successfully fabricated using electroplating techniques. These alloys provide superior protection to the substrate when compared to other coatings such as NiO, ZnO, and $Zn(OH)_2$

(Xiang, et al., 2018). The investigation of incorporating ZrO_2 particles into Ni coatings by electrodeposition has also been conducted, and it has been shown that a larger ZrO_2 concentration results in enhanced corrosion resistance. The corrosion potential of the coatings exhibits a shift towards a more optimistic direction, leading to an improvement in corrosion resistance (Arghavanian & Ahmadi, 2013).

These advancements in protective coatings offer promising strategies for preventing corrosion and preserving metal surfaces.

2.Biocides and Corrosion Inhibitors

The use of biocides and corrosion inhibitors has the potential to effectively regulate microbial proliferation and alleviate the corrosive consequences caused by microorganisms. Biocidal agents have the ability to selectively target certain microbes, while corrosion inhibitors function by mitigating the rate of corrosion via the formation of a protective layer on the surface of the metal. The inhibitory efficacy of 1,2,3-Benzotriazole (BTAH),1-hydroxybenzotriazole (BTAOH) and 5-(3-aminophenyl) tetrazole (APT) on copper corrosion has been examined and both inhibitors have reduced corrosion (Sherif, et al., 2008; Kokalj, et al., 2010).

The inhibitory effects of triazoloazepinium bromide SRBs and other corrosive microorganisms have been identified via recent research. It effectively decreases the rate of microbial copper corrosion. The development of iron-reducing bacteria, denitrifying bacteria, and ammonifying bacteria is inhibited by the biocide via the elevation of the redox potential of the corrosive medium to 170 mV (Amendola & Acharjee, 2022).

Another study demonstrated that BTAH and tetrakis (hydroxymethyl)phosphonium sulfate (THPS) were used as highly effective two corrosion inhibitors. The first mixture included

a solution containing 3.33 millimolar (mM) of BTAH and 0.245 mM of THPS. Alternatively, the subsequent composition involved a solution containing 6.5 mM of APT and 0.245 mM of THPS. The potentiodynamic polarization investigation yielded findings indicating that both formulations resulted in a change of the corrosion potential towards more positive values, therefore leading to a reduction in the corrosion current density. In particular, while using formulation (1), examinations conducted on microbial count indicated the absence of sulfate-reducing bacteria cells. Also, the absence of corrosion products on the surface remained evident, even during a prolonged immersion in saltwater for a duration of 90 days (Kumar & Rao, 2016).

3.Cathodic Protection Techniques

Cathodic protection is a commonly used method for managing corrosion in various structures, such as marine and subterranean structures, water storage tanks, gas pipelines, oil platform supports, and other facilities that are susceptible to corrosive conditions (Matcor, 2023). The fundamental concept behind cathodic protection is mitigating the deterioration or oxidation of metal in a corrosive solution by the application of a cathodic current or potential. This process effectively moves the metal towards a state of resilience. Cathodic protection has the potential to mitigate corrosion of metallic materials, hence potentially reducing corrosive wear in instances where the corrosion process is effectively controlled (Matcor, 2023). Nevertheless, when subjected to a cathodic potential (under potentiostatic conditions) or a controlled current (under galvanostatic conditions), the characteristics of a material may be altered, resulting in a corrosion-induced wear behavior that deviates from anticipated outcomes (Akonko, et al., 2005).

The correlation between cathodic protection and the corrosion rate is demonstrated. To acquire data for the purpose of improving the parameters of cathodic protection, an investigation

was conducted to determine the corrosion rate under different on-potentials and interfering AC voltages. The findings obtained in this study provide evidence that the corrosion rate may be effectively reduced by maintaining an off-potential more negative than -0.85 V vs. copper/copper sulfate ($Cu/CuSO_4$) electrode (CSE), while ensuring that the on-potential falls within the range of -1.2 V CSE (Büchler & Schöneich, 2009).

For steel structures, cathodic protection is an effective method for mitigating or preventing corrosion by inducing cathodic polarization of the metal via the use of either an external power source or sacrificial anodes. The implementation of cathodic protection on engineering infrastructure, such as underground pipelines and offshore platforms, has become an obligatory measure for ensuring long-term corrosion prevention (Yang & Cheng, 2017).

4.Monitoring and Control

The implementation of corrosion control and monitoring measures is of utmost importance in the context of upstream oil and gas pipelines. The successful use of these methodologies has the potential to mitigate corrosion incidents and empower operators to make well-informed judgments and promptly address corrosion risks (Ameh, et al., 2017).

The integration of corrosion data obtained from current field observations is being used to supplement design information for upcoming oil and gas fields. This endeavor aims to establish corrosion management approaches that are suitable for enhancing the operational lifespan of pipelines and optimizing production efficiency (Ossai, 2012). In order to mitigate the occurrence of microbiologically influenced corrosion (MIC) and other related forms of corrosion, such as stress corrosion cracking (SCC), it is recommended that hydrostatic testing of carbon steel pipes be conducted in a manner that optimizes the future service conditions of the

pipeline. This can be achieved by employing appropriate water sources, implementing adequate filtration measures, minimizing exposure to extreme temperatures, and eliminating the presence of air pockets (Ossai, 2012).

CHAPTER TWO

COPPER TOXICITY TO OLEIDESULFOVIBRIO ALASKENSIS IN THREE DISTINCT MEDIA

Description of Study

Copper's toxicity to microorganisms, including SRBs, is an important aspect of environmental microbiology and biochemistry. Soluble Cu (II) metal ions can significantly inhibit the metabolic activity of SRBs. But also, SRBs have been observed to tolerate copper toxicity. The threshold hazardous concentration of Cu (II) ions is important to understand copper tolerance of *Oleidesulfovibrio alaskensis* G20. When a G20 culture is exposed to Cu (II) ions, depending on the concentration, it may exhibit copper toxicity through longer lag times or decreased growth rate (Sani, et al., 2001). These effects become more apparent as the copper concentration is increased. Here I observed copper toxicity to *O. alaskensis* G20 at concentrations from 0 to 24 μM Cu (II) by adding copper to the growth medium from the beginning of the experiment. The aim of this work was to formulate mathematical expressions that integrate the detrimental impacts of Cu (II) into the kinetics of *O. alaskensis* G20 growth in three distinct media: 1) stoichiometrically balanced electron donor/acceptor (BAL) ratio, 2) electron acceptor limited (EAL) and 3) electron donor limited (EDL) LS4D medium (Franco & Fields, 2018). This chapter presents the experimental design, the observed results of Cu inhibition, and the quantitative impacts on *O. alaskensis* G20 growth through modifications to kinetic expressions of growth and inhibition by copper on *O. alaskensis* G20. This chapter also

presents a theoretical discourse on the impact of energy state of the cell and the ability to tolerate Cu exposure.

Experimental Methods

Growth Conditions and Batch Exposure

The sulfate-reducing bacteria (SRB) medium was prepared as described by a former scientist at CBE (Franco & Fields, 2018) with 10.39 g/L PIPES buffer disodium salt (Sigma-Aldrich #P3768), 1.63 g/L $MgCl2*6H_2O$ (Research Products International M24000), 1.07 g/L NH_4Cl, 0.09 g/L CaCl2*2H2O (Sigma-Aldrich #A9434) into nanopore water. The pH of the medium was adjusted to 7.2 using a 2 M solution of HCl. It was anaerobically dispensed 14 mL into each Balch tube (Franco & Fields, 2018). The tubes were each sealed with a clean rubber stopper and crimped with an aluminum cap. The sealed tubes were then autoclaved in the liquid cycle at 121 °C for 20 minutes. A total volume of 0.236 mL sterilized pre-mix solution containing 0.015 mL of Thauers vitamins, 0.188 mL of trace minerals and 0.033 mL of 1M potassium phosphate solution was added to each tube after sterilization. The recipe was modified by altering the concentrations of lactate and sulfate. To conduct the experiments in an electron donor and acceptor balanced condition (BAL, 60 (lactate):30 (sulfate), 60 mM of sodium lactate (Sigma Aldrich #L1375), and 30 mM of Sodium sulfate, anhydrous ≥99.0% (ACS, MP Lot No. QR14759) were added to each tube. For electron acceptor limited (EAL) settings, the lactate and sulfate concentrations were adjusted to 50 mM lactate and 15 mM sulfate. For electron donor limited (EDL) conditions, the lactate and sulfate concentrations were adjusted to 15 mM lactate and 50 mM sulfate (Franco & Fields, 2018).

Resazurin (1%vol) 0.64 mg/L (Research Products International C36200) was also added to the medium solution to serve as a general indicator of the oxidative-reduction potential (ORP) (Clark, 2006.).

Copper Concentration Adjustments

For each growth condition, initial copper concentrations were anaerobically adjusted to 6 µM, 12 µM, 16 µM, 24 µM using 10 mM copper (II) chloride stock solution pre-inoculation (Figure 2.1).

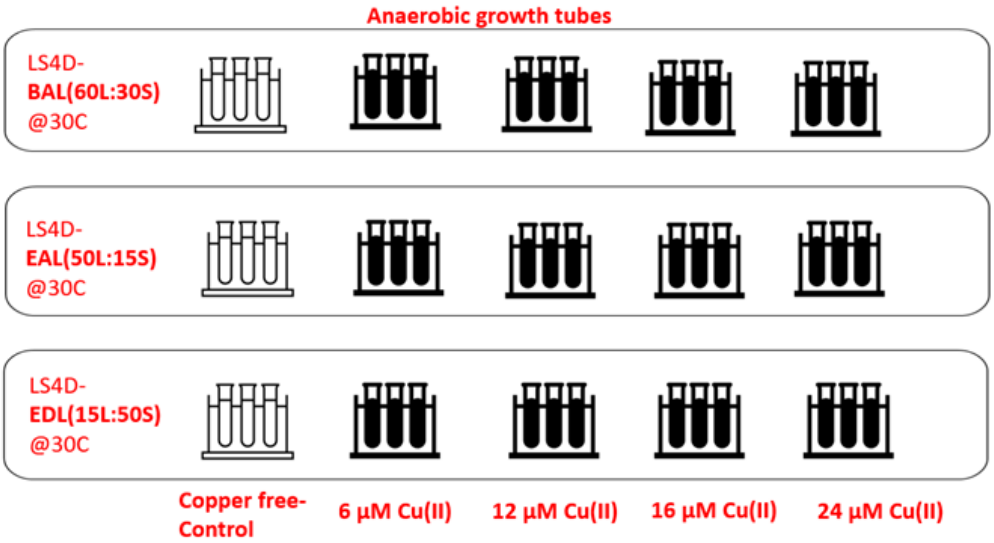


Figure 2. 1:Experimental set-up for each distinct medium, balanced, electron acceptor, electron donor media in the presence of 6 µM, 12 µM, 16 µM, 24 µM of Cu(II) concentrations.

Inoculum and Growth of Oleidesulfovibrio alaskensis G20

For all exposures, the inoculum of *O. alaskensis* G20 stored at -80°C in glycerol stock was thawed at room temperature and cultivated into previously prepared anaerobic Balch tubes as previously described (Franco & Fields, 2018) with LS4D BAL medium (14 mL). Cultures were grown till mid-exponential phase, reaching between approximately 0.4-0.45 OD_{600}, at 30

°C, and then 0.1-0.2 ml of this culture was inoculated into 9 ml Balch tube containing the respective anaerobic medium. The cultures were again harvested at the mid-exponential phase to inoculate previously prepared tubes. Sulfide was removed from the inoculum prior to inoculation of the tubes as previously described (Klonowska, 2008.). To remove sulfide, the cultures were centrifuged at 4900×g for 14 minutes at room temperature in anaerobic Balch tubes. To obtain G20 cell pellets, the supernatant was removed using a sterile needle linked to a vacuum bottle under constant flow of N_2 gas for a constant anoxic pressure. G20 cell pellets were then re-suspended in 9 ml fresh anoxic medium containing sulfate and lactate concentrations of the LS4D BAL, EAL, EDL growth conditions and re-washed. The cell pellets were re-suspended and added into 9 ml tubes containing LS4D BAL, EDL, EAL medium to concentrate the cell suspension for inoculation into the respective as previously described (Franco & Fields, 2018). The optical density (600 nm) of the tubes was measured using a Thermo Scientific, Genesys 10S UV-VIS Spectrophotometer to monitor the growth in a dark static water batch at 30 °C.

Quantification Copper Toxicity and Growth Kinetics of *Oleidesulfovibrio alaskensis* G20

For each tube, equation 1 was used to calculate the maximum specific growth rate (μ_{max}) using OD_{600} (X_1 and X_2) during the time interval (t_2-t_1) estimated for the steepest part of exponential growth:

$$\mu_{max} = \frac{\ln\left(\frac{X_2}{X_1}\right)}{(t_2 - t_1)} \qquad t_2 > t_1 \qquad \text{(Eq. 1)}$$

Log-scale exponential growth curves were created to determine specific growth rates and cell doubling time (td).

$$t_d = \frac{\ln(2)}{\mu} \qquad \text{(Eq. 2)}$$

This research assumes that copper functions as a noncompetitive inhibitor, resulting in a decrease in the maximum specific growth rate without affecting the half-saturation coefficients ($S_{lactate}$ and $S_{sulfate}$) .

Non-competitive inhibition kinetics for electron acceptor-limited cultures grown in LS4D EAL can be linearized when $S_{Lactate} >> K_{Lactate}$, by plotting reciprocal of maximum specific growth rate in the presence of different copper concentrations versus I (total Cu concentration) (Okabe, et al., 1995):

$$\frac{1}{\mu^{i}_{max}} = \frac{1}{\mu_{max}} + \frac{I}{\mu_{max} K_i} \quad \text{(Eq. 3)}$$

where μ_{max} =maximum specific growth rate (h^{-1}), I =copper concentration (μM), K_i= inhibition coefficient (μM), μ^{i}_{max}= maximum specific growth rate in the presence of copper (h^{-1}). Therefore, the x-intercept of a best-fit line is equal to negative K_i.

The electron donor and acceptor used in this study were sodium sulfate and sodium lactate, which were present in three distinct different ratios for the respective growth conditions (BAL, EAL, and EDL.) In this scenario, an inhibitor is assumed to undergo a reaction with both substrates. Given the nature of this mechanism, the reaction could possibly be characterized as a rapid equilibrium or random mechanism behaving as a noncompetitive inhibitor binding to both substrates, therefore allowing the use of the following equations previously developed by (Cheng & Prusoff, "Relationship between the inhibition constant (KI) and the concentration of inhibitor which causes 50 per cent inhibition (I50) of an enzymatic reaction., 1973):

$$V_0 = \frac{V_{max} * S_L * S_S}{(K_{iL} * K_S + K_L * S_S + K_S * S_L + S_L * S_S)} \quad \text{(Eq.4)}$$

$$V_I = \frac{V_{max} * S_L * S_S}{(K_{iL} * K_S + K_L * S_S + K_S * S_L + S_L * S_S *)(1 + \frac{I}{K_I})} \quad \text{(Eq.5)}$$

Where V_0 = velocity in the absence of the inhibitor and V_I = velocity in the presence of inhibitor, V_{max} = maximum velocity, S_L=lactate concentration, S_S=sulfate concentration, K_L= Michaelis constant of lactate, K_S= Michaelis constant of sulfate, K_{iL}=dissociation constant of lactate. When equation 4 is substituted into equation 5, the value of I_{50} does not depend on substrate concentrations and the relationship between K_i and I_{50} (the concentration of inhibitor required to produce 50% inhibition) is (Brandt, Laux, & Yates, 1987):

$$K_i = I_{50} \quad \text{(Eq.6)}$$

Thus, K_i values of BAL and EAL are equivalent to I_{50} (Cheng & Prusoff, "Relationship between the inhibition constant (KI) and the concentration of inhibitor which causes 50 per cent inhibition (I50) of an enzymatic reaction., 1973).

To find the Cu concentration required to produce 50% inhibition of growth rate, the maximum specific growth rate observed in the presence of different copper concentrations was plotted as a function of inhibitor concentrations (Sani, et al., 2001).

Results and Discussion

Microbial Growth

The influence of increasing copper concentrations on cell doubling times and total final cell density of batch cultures in three medium conditions, namely LS4D-BAL, EAL, and EDL, is evident in Table 2.1. As expected, the experimental results indicate that the ultimate cell density was higher in the respective control group without copper in three different growth conditions. Based on the results, the final biomass yields of EAL and EDL had a decrease of roughly 42% and 50% respectively, in comparison to BAL cultures without copper (Table 2.1). The observed lower yields for EAL and EDL compared to BAL are expected given the sub-optimal ratios (3.33

and 0.3, respectively versus 0.5 for BAL) that can support growth and survival. In the absence of lactate as a substrate, the electron transport and metabolic activity of *O. alaskensis* G20 can be dramatically altered. The Qmo and Qrc complexes are two electron transfer systems that are functionally vital to *O. alaskensis* G20.

Table 2. 1: Results of copper effect on final cell density (OD_{600}), specific growth rate, doubling time(td) and the maximum specific growth rate of *O.alaskensis* G20 in three distinct mediums (LS4D-BAL, EAL, EDL) in the presence of various copper concentrations.

	Final cell density (OD_{600})	**$\mu(h^{-1})$**	**$\mu_{max}(h^{-1})$**	**td(h)**
BAL (60L:30S) + 0 µM Cu^{+2}	1.085 +/-0.018	0.1	0.136 +/-0.013	6.9
BAL (60L:30S) + 6 µM Cu^{+2}	0.879 +/-0.732	0.089	0.109 +/-0.047	7.7
BAL (60L:30S) + 12 µM Cu^{+2}	0.838 +/-0.697	0.034	0.120+/-0.03	20.38
BAL (60L:30S) + 16 µM Cu^{+2}	0.459 +/- 0.716	0.016	0.057+/-0.005	41.25
BAL (60L:30S) + 24 µM Cu^{+2}	0.046 +/-0.002	NA	NA	NA
EAL (50L: 15S) + 0 µM Cu^{+2}	0.628+/-0.06	0.104	0.130+/-0.016	6.6
EAL (50L: 15S) + 6 µM Cu^{+2}	0.815+/-0.044	0.068	0.121+/-0.031	10.1
EAL (50L: 15S) + 12 µM Cu^{+2}	0.855+/-0.059	0.064	0.096+/-0.041	10.8
EAL (50L: 15S) + 16 µM Cu^{+2}	0.843+/-0.031	0.030	0.058+/-0.43	23.2
EAL (50L: 15S) + 24 µM Cu^{+2}	0.537+/-0.414	0.013	0.095+/-0.019	50.2
EDL (15L: 50S) + 0 µM Cu^{+2}	0.533+/-0.012	0.102	0.149+/-0.030	6.7

Table 2.1 Continued

EDL (15L: 50S)+ 12 µM Cu^{+2}	0.658+/-0.032	0.057	0.07+/-0.05	12.0
EDL (15L: 50S)+ 16 µM Cu^{+2}	0.251+/-0.404	0.018	0.032+/-0.021	37.6
EDL (15L : 50S)+ 24 µM Cu^{+2}	0.306+/-0.475	NA	NA	NA

The Qmo complex transfers electrons from the MQ pool to the cytoplasmic APS reductase (AprBA), which is necessary for the sulfate reduction pathway for SRB. In greater detail, the process of lactate oxidation by strain G20 involves the generation of a reduced thiol-disulfide redox pair(s) and ferredoxin. These products are energetically linked to the reduction of H+ by periplasmic formate dehydrogenase and hydrogenase through a flavin-based reverse electron bifurcation process, also known as electron confurcation. Additionally, a menaquinone (MQ) redox loop facilitates the reverse flow of electrons, which is mediated by the membrane-bound Qmo and Qrc complexes. This electron transfer system enables higher rates of lactate oxidation in the presence of elevated hydrogen levels and facilitates the use of formate as the primary electron exchange mediator (Keller, et al., 2014; Duarte, et al., 2018). The results showed that the EAL and EDL conditions caused sub-optimal biomass yields due to unbalanced ratios of electron donors and acceptors although maximal growth rates were not significantly different from the BAL condition (Table 2.1).

The absence of lactate is most likely the cause of the 50% decrease in sulfate reduction in EDL copper-free cultures compared to BAL copper- free cultures. *O. alaskensis* G20 enabled to reduce sulfate, due to the lack of channeling electrons from the MQ pool to the cytoplasmic APS

reductase (AprBA) and a 50% decrease in sulfate concentration in EAL medium caused a 42% decrease in cell density.

The cell densities in the EAL condition exhibited a 23 and 26% increase when exposed to concentrations of 6 and 12 μM Cu(II), respectively (Table 2.1). In contrast, the final cell densities observed in the BAL condition exhibited a drop of 19% compared to BAL copper free cultures under identical conditions. The cell density of the EDL condition exhibited a 16% increase when exposed to concentrations of 6 and 12 μM Cu(II), as compared to the EDL copper-free condition. The slight increases in optical density could also be due to metal precipitation (increasing Cu), and this coincides with previous work previous work that showed significant cell lysis did not occur (Sani, et al., 2001). When exposed to 6 and 12 uM Cu(II), *O. alaskensis* G20 can tolerate copper toxicity better under the limited substrates conditions, the limiting of lactate (EDL) or sulfate (EAL).

In the presence of 16 μM Cu (II), the final cell densities of BAL and EDL conditions were reduced by 57% and 53%, respectively. However, the cell density seen in the EAL condition exhibited a 25% increase when compared to the EAL control group, when subjected to similar experimental settings, albeit the generation time for EAL was increased almost 4-fold (Table 2.1). Upon exposure to a concentration of 24 μM Cu(II), the cell density of EAL exhibited a decrease of 15%, accompanied by an additional increase in the generation time to 50.2 h, compared to the EAL control culture (6.6 h). In contrast, BAL cultures exhibited no detectable growth, while only a single replicate demonstrated growth under the EDL condition in the presence of 24 μM Cu(II). The growth exhibited variability and prolonged doubling time when copper concentrations were increased in the three growth conditions (Table 2.1).In the presence

of copper, in addition to the metal toxicity, the lack of growth (little sulfide production typically associated with SRB growth) also causes prolonged exposure to higher redox potentials (> -100 mV) (Sani, et al., 2001) in the growth medium that also likely contributes to reduced growth.

Despite the fact that Cu(II) has been known to be an inhibitor of periplasmic hydrogenase (Fernandez, Rua, Reyes, Cammack, & Hatchikian, 1989; Fitz & Cypionka, 1991), this work reveals that threshold concentrations of copper ions (24 μM for EAL) differ for cells grown under EAL and EDL conditions, and the data suggests that cells likely utilize altered routes of electron transfer when trying to balance carbon and energy allocation.

In order to assess the impact of Cu(II) toxicity in the BAL, EAL, and EDL conditions, the extent of inhibition on the maximum growth rate was determined at various amounts of Cu(II) (Figure 2.2B, Figure 2.3B, and Figure 2.4B, respectively). The least-squares lines for BAL, EAL, and EDL conditions were calculated, with R^2 values of 0.99, R^2=0.95, and R^2=0.99, respectively. These lines were then used to determine the concentration of Cu(II) adequate to inhibit maximum growth rate of *O. alaskensis* G20 by 50%, which was referred to as the I50 value. Increasing Cu(II) levels decreased G20 growth and biomass yields, and the growth responses were different for each of the growth conditions.

Quantification of Copper Toxicity of *Oleidesulfovibrio alaskensis* G20 in LS4D - BAL

This phase of the research was to determine the impact of copper toxicity by measuring the inhibition of *Oleidesulfovibrio alaskensis* G20 growth in LS4D-BAL(60L:30S) media. This was determined by assessing the decrease in maximum specific growth rates. The figure labeled as Fig 2.2. illustrates the growth trends of *O.alaskensis* G20 in LS4D-BAL medium ranging from 0 to 24 μM.

As seen in Figure 2.2B, the lag phases observed in the presence of 6 μM Cu(II) were found to be longer compared to the copper-free control. In the presence of Cu(II), the maximum specific growth rate was reduced by approximately 19 and 34.5% compared to the copper-free control for 6 and 12 μM Cu(II), respectively. At a concentration of 16 μM Cu(II), the growth rate showed a substantial decrease. Furthermore, the lag time for one tube increased to 120 hours, and the maximum specific growth rate was lowered by 58% compared to the copper-free control. In addition, no measurable growth was observed in the other two tubes. The results demonstrate that when subjected to identical circumstances, the presence of Cu(II) at a concentration of 24 μM resulted in full inhibition of growth (Figure 2.2A) and I_{50} value was 13.1 μM (Figure 2.2B).

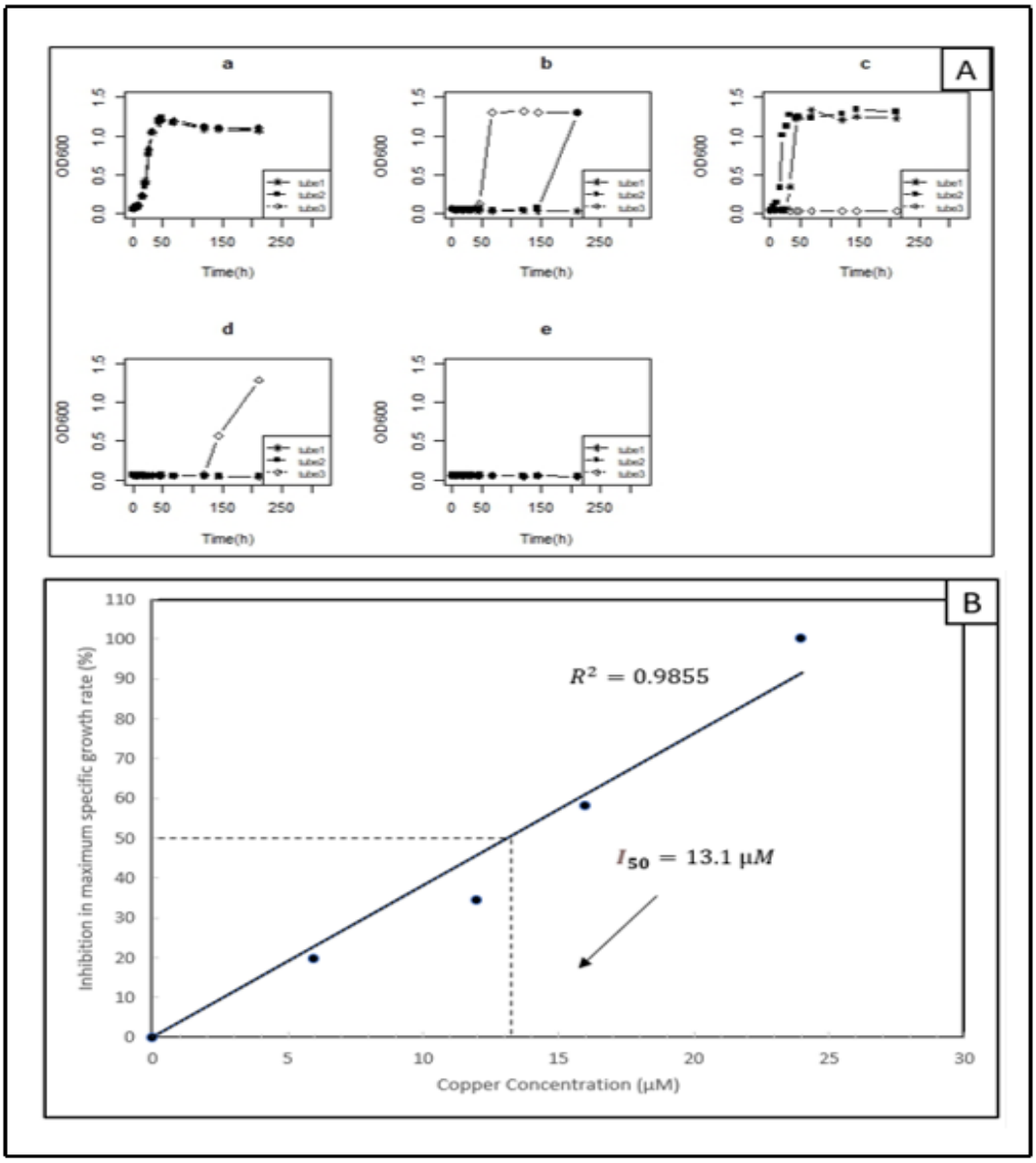


Figure 2. 2: Growth of *Oleidesulfovibrio alaskensis* G20 in balanced medium (30S:60L) in the presence of various copper concentrations: (a) control, Cu-free, (b) 6 µM Cu^{+2}, (c) 12 µM Cu^{+2}, (d) 16 µM Cu^{+2}, and (e) 24 µM Cu^{+2}, and based upon growth rate impacts a K_i of 13.1 µM is estimated under BAL growth conditions.

Quantification of Copper Toxicity of
Oleidesulfovibrio alaskensis G20 in LS4D – EAL

The percentage inhibition in the maximum growth rate was determined at various amounts of Cu(II) LS4D EAL (50L:15S) media. These results were then shown in Figure 2.4B

with the growth profile in Figure 2.4A. As seen in Fig 2.4A, the lag phases observed in the presence of 6 μM Cu(II) were found to be almost 20 hours longer compared to the control. The lag phases were longer in the 16 μM Cu(II) culture. In the presence of Cu(II), the maximum specific growth rate was reduced by approximately 7 and 26% compared to the copper-free control for 6 and 12 μM Cu(II), respectively. At a concentration of 16 μM Cu(II), the growth rate showed a substantial decrease (70%). Furthermore, the lag time increased to 68 hours, and the maximum specific growth rate was lowered by 55% compared to the copper-free control. However, all replicates exhibited growth, but in LS4D BAL cultures, only a single tube shown growth, although with a prolonged lag phase. The results demonstrate that the presence of Cu(II) at a concentration of 24 μM resulted in full inhibition of growth as the cultures grown in LS4D BAL and EDL media. This inhibition was evident as no measurable growth was detected for a duration of up to 211 hours observation. While cells grown under the EAL condition tolerated Cu exposure, lag periods were still observed longer and the I_{50} value for EAL condition was 13.9 μM (Figure 2.3B).

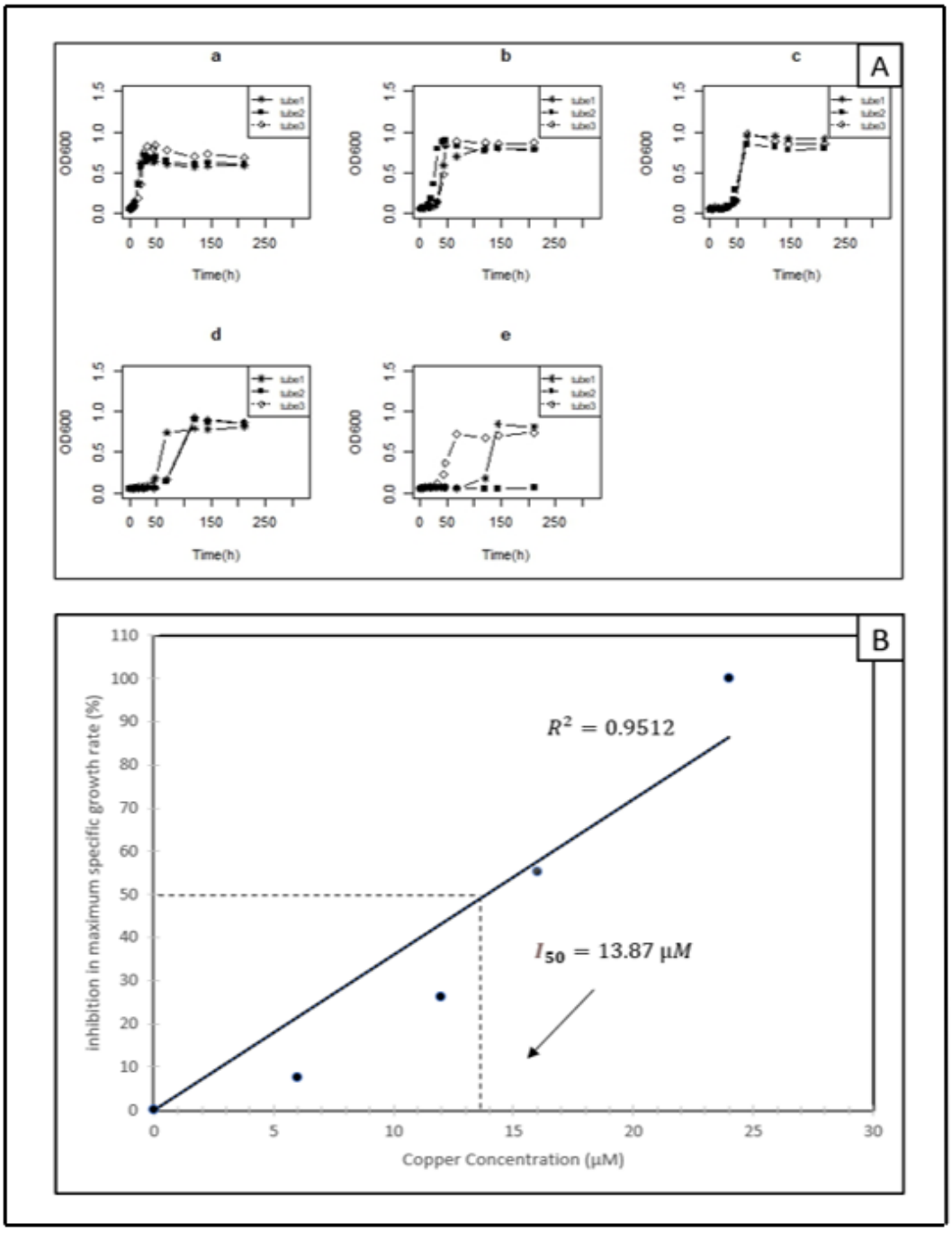


Figure 2. 3: Growth of *Oleidesulfovibrio alaskensis* G20 in electron acceptor limited medium (50L:15S) in the presence of various copper concentrations: (a) control, Cu-free, (b) 6 µM Cu^{+2}, (c) 12 µM Cu^{+2}, (d) 16 µM Cu^{+2}, and (e) 24 µM Cu^{+2}, and based upon growth rate impacts a I_{50} of 13.9 µM was estimated under EAL growth conditions.

Quantification of Copper Toxicity of
Oleidesulfovibrio alaskensis G20 in LS4D – EDL

For the EDL growth condition, the lag phases observed in the presence of 6 μM Cu(II) started to be longer compared to the copper-free control. Also, in the presence of 6 and 12 μM Cu(II), all experimental tubes exhibited measurable growth. In the presence of Cu(II), the maximum specific growth rate was reduced by approximately 30 and 53% compared to the copper-free control for 6 and 12 μM Cu(II), respectively. At a concentration of 16 μM Cu(II), the growth exhibited a similarly significant decline to that observed under the BAL condition. In addition, the lag time for one tube increased considerably, and the maximum specific growth rate was lowered by 78% compared to the copper-free control. Also, measurable growth was not observed in the other replicates (Figure 2.4B). The results demonstrate that the presence of Cu(II) at a concentration of 24 μM resulted in full inhibition of growth under the EDL growth conditions. This inhibition was evident as no measurable growth was detected for a duration of up to 211 hours observation. While cells grown under the EDL condition tolerated Cu exposure, lag periods were still observed and the I_{50} value for the EDL condition was lower (11.3 μM) compared to the other growth conditions (Figure 2.4B).

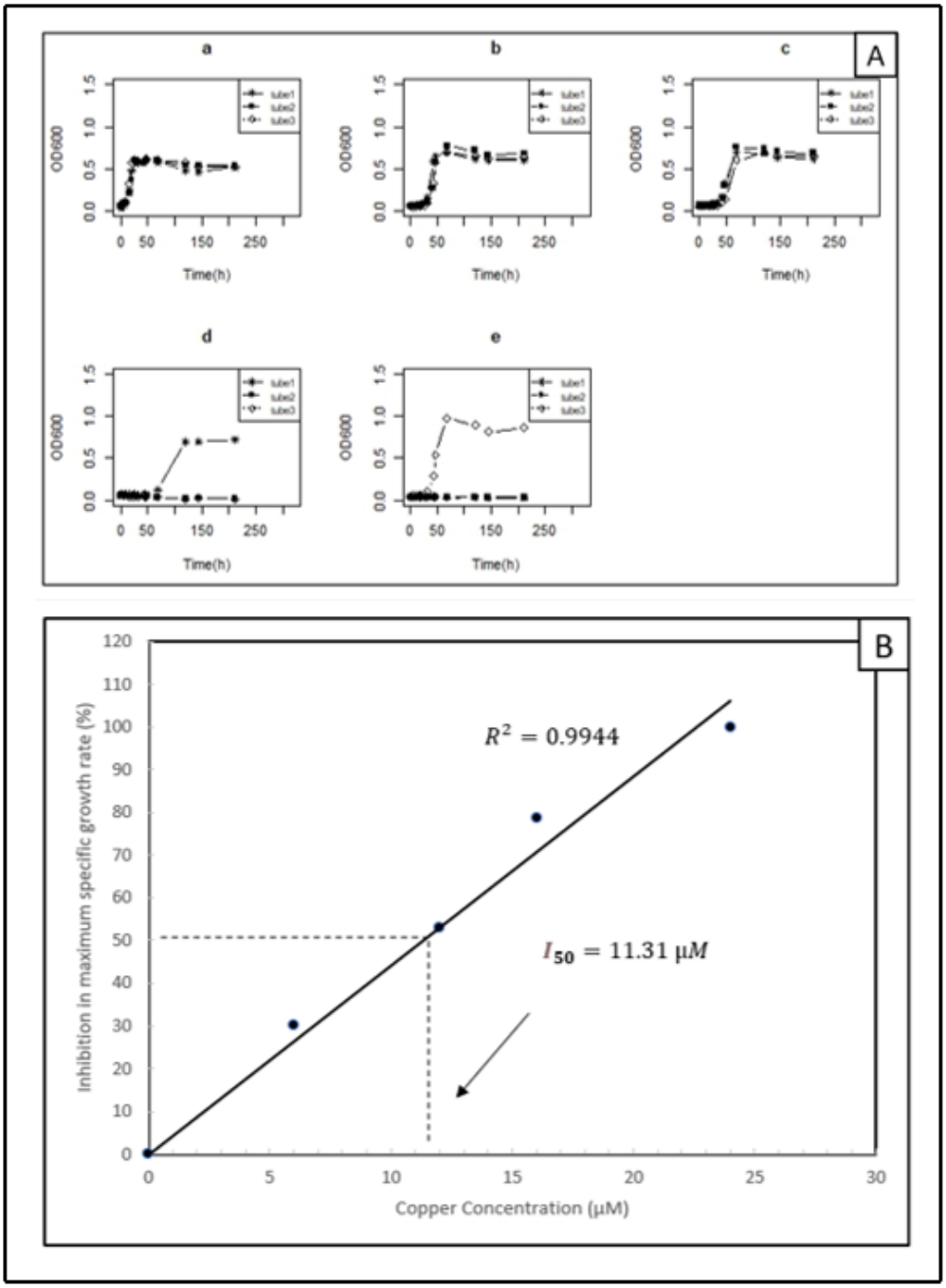


Figure 2. 4 Growth of *Oleidesulfovibrio alaskensis* G20 in electron donor limited medium (15L:50S) in the presence of various copper concentrations: (a) control, Cu-free, (b) 6 µM Cu^{+2}, (c) 12 µM Cu^{+2}, (d) 16 µM Cu^{+2}, and (e) 24 µM Cu^{+2}, and based upon growth rate impacts a I_{50} of 11.3 uM is estimated under the EDL growth condition.

The authors, Okabe and Characklis (Okabe, et al., Sulfide product inhibition of Desulfovibrio desulfuricans in batch and continuous cultures, 1995), have presented evidence suggesting that the kinetics of sulfide inhibition should be taken into account in environments with high sulfide concentrations, including SRBs. Under the tested growth conditions, copper has a strong attraction towards sulfide ions, leading to the creation of solid copper sulfide precipitates, and the local pH will play a crucial role in the sulfur chemistry. The pK_a value of hydrogen sulfide (H_2S) is approximately 7.0, and based on the pH of 7.2 in LS4D medium, it can be inferred that half the concentration of HS^- does not have a harmful influence on the growth of *O. alaskensis*. The available sulfide ions can react with copper ions that results in copper sulfide precipitates, and thus continued growth (associated sulfide production) alleviates potential copper toxicity.

K_i Measurements

In the case of noncompetitive inhibitors, it is seen that the inhibition constant is unaffected by changes in substrate concentrations (Cheng & Prusoff, "Relationship between the inhibition constant (KI) and the concentration of inhibitor which causes 50 per cent inhibition (I50) of an enzymatic reaction., 1973). For the case of some lactate-consuming SRBs, the K_i value has been shown to be equivalent to I_{50} when substrate concentrations significantly exceed $K_{lactate}$ and $K_{sulfate}$ (Cheng & Prusoff, 1973; Okabe, et al., 1995; Song, et al., 1998).). In a previous study, the $K_{sulfate}$ and $K_{lactate}$ half-saturation coefficients were found to be 1.8 mg/L($1.87e^{-5}$ mM)-and 2.35 mg/L ($2.6e^{-5}$ mM)-respectively (Okabe, et al., Sulfide product inhibition of Desulfovibrio desulfuricans in batch and continuous cultures, 1995), under the similar experimental conditions that were much lower than the substrate concentrations (BAL

60S:30L, EAL 50L:15S, EDL 15L:50S mM) used in this study. The experimental settings used in our study fit to the noncompetitive inhibition hypothesis. The K_i values obtained for the BAL, EAL, and EDL conditions equate to I_{50} values of 13.1, 13.87, and 11.31 μM, respectively. The equation 3., which represents the non-competitive inhibition model for sulfate-limited and lactate-excessive condition (EAL), was employed to determine the inhibition coefficient for the maximum specific growth rates of *O. alaskensis* culture on LS4D EAL media with the aim of assessing the compatibility between the obtained K_i values from the equation 3 and the expected values using I_{50}. For the EAL condition, an estimated K_i value of 11.9 uM was similar to the I_{50} value of 13.9 uM (Figure 2.5). A previous study identified the copper inhibition constant of 17.9 mM (Utgikar, et al., 2003), which is significantly greater than the inhibition constants found in this study. It is important to note that under the described conditions, cells were washed to remove sulfides in order to assess initial cellular responses. Therefore, lower values should be expected.

The non-competitive inhibition model equation (equation 3) was used to calculate the inhibition coefficients (K_i values) for the maximum specific growth rates of *O. alaskensis* culture on LS4D EAL media. Because the use of a non-competitive inhibition model has been documented in prior investigations to characterize the kinetics of inhibition and half-saturation coefficients of the substrates were determined to be $K_{sulfate}$ =1.8 mg/L($1.87e^{-5}$ mM) and $K_{lactate}$ =2.35 mg/L ($2.6e^{-5}$ mM) using comparable experimental conditions (Okabe, et al., Sulfide product inhibition of Desulfovibrio desulfuricans in batch and continuous cultures, 1995). For noncompetitive inhibitors, the inhibition constant is independent of substrate concentrations, and

$K_i = I_{50}$ when substrate concentrations are considerably greater than $K_{lactate}$ and $K_{sulfate}$ (Okabe, et al., 1995; Song, et al., 1998; Cheng & Prusoff, 1973).

As seen in Figure 2.5 with the square of the correlation coefficient $R^2 = 0.75$, the determined Ki was 11.9 µM. This value is not significantly different from I_{50}=13.87 µM.

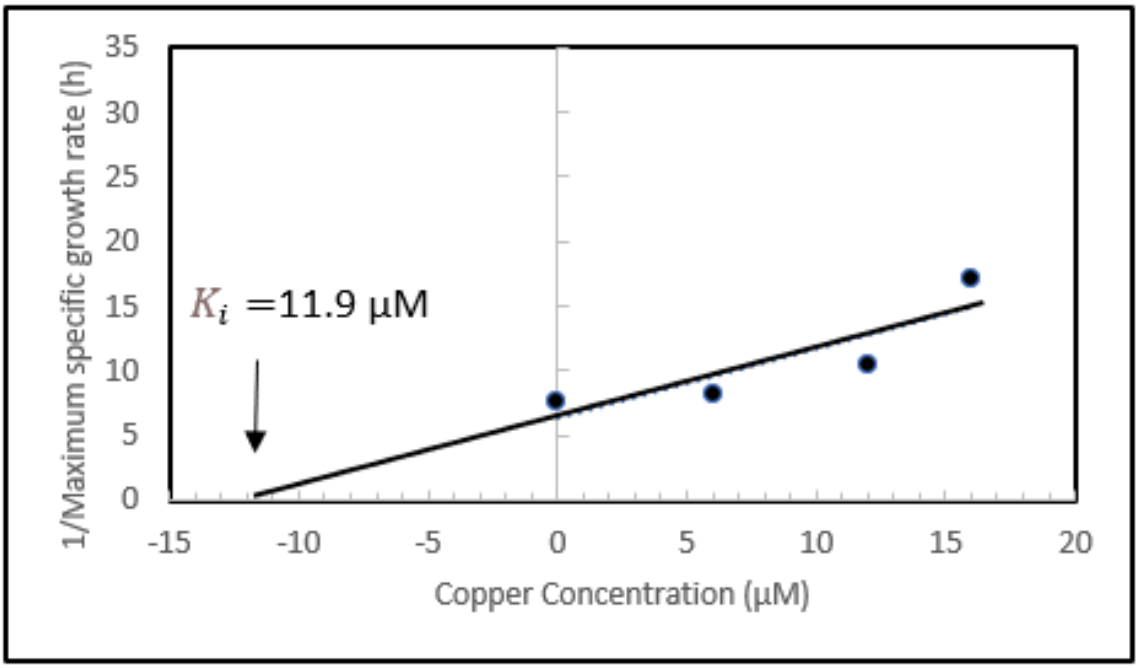


Figure 2. 5: Determination of K_i value in the EAL medium. Theoretical plot of the inverse of maximum specific growth rate (1/µ) in the presence of different copper concentrations in the batch cultures, 6 µM,12 µM,16, and 24 µM, and control, Cu-Free as a function of copper concentrations (Cu^{+2}). K_i of 12.19 µM was determined (R^2=0.75).

The presented results showed the I_{50} values of Cu(II) for *O. alaskensis* G20 to be 13.1, 13.9, and 11.3 µM for BAL, EAL, and EDL growth conditions, respectively. Sani and Peyton (Sani et al., 2001 reported that a concentration of 16 µM Cu(II) was found to cause a 50% inhibition of bacterial growth. However, an alternative medium named MTM (Sani, et al., 2001) was used. According to a different paper on the effective treatment of electroplating wastewater utilizing an anaerobic batch test, 1.6 mM Cu(II) was the concentration that caused a 50%

decrease of SRB sulfate removal efficiency (Song, et al., 1998). No inhibition in sulfate reduction was detected at doses of Cu(II) up to 79 μM. It is important to acknowledge that the researchers used a mixed SRB culture and an anaerobic growth medium that consisted of elements previously shown to have a significant impact on metal precipitation (Sani, et al., 2001).

Our reported results demonstrated the impact of energy-source ratios on cellular growth as well as the implications on cellular responses to metals. In previous work with *Desulfovibrio vulgaris Hildenborough* and Cr(VI), the EAL condition displayed slower growth and longer lag times compared to BAL and EDL conditions (Franco & Fields, 2018). In a separate study with G20 biofilms on carbon steels, differences in corrosion rates were observed between the EAL and EDL conditions, and the EDL condition promoted higher corrosion rates (Krantz, et al., 2019). In the presented results with G20 and copper, although the I_{50} values were similar for the three growth conditions, the EAL growth condition had improved tolerance to the presence of copper. These results indicate that the initial cellular responses of SRBs to different metals can be metal-dependent and are greatly impacted by available exogenous resource ratios. In natural and man-made environments, microorganisms are challenged with dynamic nutrient availabilities that are seldom 'balanced'; therefore, experiments under relevant nutrient conditions are important to inform assessments of biological responses to metals in the environment, particularly for a metal such as copper that is heavily used in numerous applications.

Fit curves exhibited an R^2 of more than 0.90 in most cases (only two of them 0.89 and 0.88) and did not differ from any experimental data point by more than 10%.

Conclusion

This study provides a detailed quantitative analysis of the kinetic impact of Cu(II) toxicity on *Oleidesulfovibrio alaskensis* G20, focusing on the integration of Cu(II) effects into the kinetics of copper in three different growth media, LS4D BAL, EAL, EDL. The findings indicate a concentration-dependent toxicity of Cu(II), where increased copper concentrations result in inhibited growth rates, reduced cell densities, and prolonged lag periods. Particularly in EAL conditions, cell densities initially increase at lower Cu(II) concentrations but decrease significantly at higher concentrations. The study also establishes that *O. alaskensis* G20 tolerates copper toxicity better under EAL conditions, suggesting an adaptive response to copper stress. Additionally, the inhibition constant (K_i) values of the noncompetitive inhibition model for three mediums reveal an understanding of Cu(II) toxicity, with lower values than those reported in previous studies. This research thus offers crucial insights into copper toxicity dynamics, highlighting the variable impact of Cu(II) depending on environmental and media conditions.

CHAPTER THREE

EFFECTS OF SURFACE ROUGHNESS ON MICROBIOLOGICALLY INFLUENCED CORROSION (MIC) OF COPPER 101 BY OLEIDESULFOVIBRIO ALASKENSIS G20

Contribution of Authors and Co-Authors

Manuscript in Chapter 3

Author: Yagmur Keskin

Contributions: Formal analyses, investigation, data curation, writing-original draft

Co-Author: Amit Acharjee

Contributions: Formal analyses, investigation, data curation, writing-original draft

Co-Author: Dr. Roberta Amendola

Contributions: Conceptualization, methodology, validation, writing-original draft, writing-review and editing, supervision

Co-Author: Dr. Matthew Fields
Contributions: Conceptualization, methodology, validation, writing-original draft, writing-review and editing, supervision

Co-Author: Dr. Brent Peyton

Contributions: Conceptualization, methodology, validation, writing-original draft, writing-review and editing, supervision

Manuscript Information

Authors: Amit Acharjee, Yagmur Keskin, Matthew W. Fields, Brent M. Peyton and Roberta Amendola

International Biodeterioration & Biodegradation

Status of Manuscript: [Put an x in one of the options below, then delete instruction in brackets]
☐ Prepared for submission to a peer-reviewed journal
☒ Officially submitted to a peer-reviewed journal
☐ Accepted by a peer-reviewed journal
☐ Published in a peer-reviewed journal

International Biodeterioration & Biodegradation
Date of submission: 1/4/2024

Abstract

Copper has become an important industrial metal, ranking third behind iron and aluminum in terms of quantity that is utilized, and the features of high ductility, malleability, thermal and electrical conductivity, antimicrobial property, and resistance to corrosion have contributed to the prominence of copper in the industrial sector (Flanagan, 2023). Despite the inherent, anti-microbial characteristics of copper, effective protection strategies must be implemented-to reduce metal corrosion, particularly for water-saturated, anoxic environments that are conducive to SRB growth. The presented work evaluates the effect of surface finishing on microbiologically influenced corrosion (MIC) of copper caused by exposure to *Oleidesulfovibrio alaskensis* G20, a model sulfate-reducing bacterium. 3D optical profilometry, Scanning Electron Microscopy (SEM), Energy Dispersive X-Ray (EDX), and X-ray Diffraction Analysis (XRD) were used to investigate corrosion morphology and product development on copper with different surface properties. Uniform and pitting corrosion were observed for all surface finishes, but the degree and localization of corrosion differed. The surface roughness affected the growth kinetics of the mineral layer, the morphology, and the pitting development. A statistically significant change in the corrosion rate as well as cellular/mineral layers was observed when the roughness of the copper surface was decreased from ~13 μm to ~0.06 μm. The results demonstrated that surface roughness can impact the extent, localization, and mineralization of polycrystalline copper by sulfate-reducing bacteria.

Introduction

Corrosion is a physiochemical metal deterioration process that progresses in a series of redox reactions (anodic oxidation, cathodic reduction) where pure metal and/or alloys undergo a

chemical change from ground to an ionized state due to transfer of electrons from the metal to an external acceptor. When such deterioration is guided by the presence of a microbial biofilm consisting of microbial cells and extracellular polymeric substances (EPS), the process is called microbiologically influenced corrosion (MIC) (Beech & Gaylarde, 1999, Chen et al., 2014). In the most recent available estimate, the annual cost of damage due to corrosion is approximately 2.5 trillion USD globally and MIC is considered to be responsible for about 20% of the total expenditure and for 50% of all pipeline infrastructure failures (Wang et al., 2014; Liu et al., 2016; (Javaherdashti, 1999) However, as microorganisms can grow and survive in a wide variety of environments characterized by water activity, minimal amounts of nutrients and life-permitting temperatures, it is likely that MIC and abiotic corrosion processes coexist; therefore, cost and mechanism differentiation between biotic and abiotic processes can be difficult (Little et al., 2020).

Copper has become an important industrial metal, ranking third behind iron and aluminum in terms of quantity that is utilized, and the features of high ductility, malleability, thermal and electrical conductivity, antimicrobial property, and resistance to corrosion have contributed to the prominence of copper in the industrial sector (Flanagan, 2023). Copper is widely used in many industrial and domestic applications (*e.g.*, marine structures, premise plumbing) due to corrosion resistance; however, despite being widely used due to antimicrobial properties, it is not immune to MIC and many cases of copper MIC have often been related to catastrophic infrastructure failures (Chen et al., 2014; Wagner & Little, 1993; Güngör et al., 2015; Trevors & Cotter, 1990; Javed et al., 2016). Many variables can impact the rate and extent

of corrosion, including the type of metal, the environmental conditions, and the associated microorganisms, but the exact relationships are difficult to delineate.

Sulfate reducing bacteria (SRB), present in many natural water and soil environments, have been linked to half of all MIC related cases (Yuan et al., 2013; Lee et al., 1995). The predominant type of damage associated with MIC is pitting corrosion which has long been regarded as an MIC signature (Pope & Morris, 1995; Sarioğlu et al., 1997). Pitting can lead to material perforation and compromise mechanical properties as the "root" of the pit can act as a stress magnifier leading to catastrophic failures. Oil and gas production and marine infrastructures are among the many industries suffering substantial financial loss caused by MIC (Dou et al., 2020; Talha et al., 2019; Brauer et al., 2017). Among the different mechanisms proposed to explain MIC of copper and copper alloys, Type II defined as metabolite MIC (M-MIC) caused by the secretion of corrosive metabolites, was recently accepted as the most probable (Javed et al., 2016; Dou et al., 2020; Wang et al., 2020; Dou et al., 2018). M-MIC does not necessarily depend on the biofilm for energy directly (*i.e.*, electron extraction), as metabolites like organic acids and sulfides can react with the metal substrate extracellularly causing the development of a mineral layer. The production of sulfide by SRB is indirect, as the final metabolic product is HS^-, which then combines with H^+ to form H_2S (pK_a of 7.0) (Perrin, 1982). The following reactions between copper and H_2S were previously identified as thermodynamically favorable (Puigdomenech & Taxen, 1970; Bard et al., 2017):

$$2Cu\ (s) \rightarrow 2Cu^{+} + 2e^{-} \qquad \text{Anodic} \qquad (1)$$

$$HS^{-} + H^{+} + 2e^{-} \rightarrow S^{2-} + H_2 \qquad \text{Cathodic} \qquad (2)$$

$$2Cu\ (s) + H_2S\ (g) \rightarrow Cu_2S\ (s) + H_2\ (g) \qquad (3)$$

Chen et al. showed that, before the formation of Cu_2S is achieved, an intermediate product, $Cu(SH)_{ads}$ adsorbs on the Cu surface as follows (Chen et al., 2011; Chen et al., 2010; Chen et al., 2017):

$$Cu^+ + HS^- \rightarrow Cu(HS)_{ads} + e^- \quad (4)$$

$$Cu + Cu(HS)_{ads} + HS^- \rightarrow Cu_2S + H_2S + e^- \quad (5)$$

The copper corrosion rate is therefore mostly defined by the sulfide concentration [HS^-] available in the local environment (Chen et al., 2017; Dou et al., 2020; King et al., 2017). Previous research showed that in stagnant conditions, [HS^-] also defined the morphology of the Cu_2S layer, namely a dense single layer with a well-defined crystalline structure that was formed at high [HS^-] while a porous Cu_2S layer was instead developed at relatively low [HS^-] (Chen et al., 2017; King et al., 2017).

In the last few decades, the rapid growth of nucleic acid-based methods for profiling microbial communities introduced a wide range of genomic techniques that are now used as tools aiding MIC diagnostics (*e.g.*, SSU rRNA gene sequencing, metagenomics). While informative, detection and prediction of MIC based solely on the profile of the microbial community residing in a system has proven challenging due to microbial diversity both in terms of genomics and eco-physiology. Moreover, the role of substrate material intrinsic properties, such as surface topography, microstructure, and native oxide layers, etc., on the biofilm formation and consequently on the intensity of MIC have been limited. For example, surface finish plays an important role in the corrosion behavior of metals (Alvarez et al., 2010; Abosrra et al., 2009; Burstein & Pistorius, 1995).The surface finish of a material is, in most cases, defined by the surface roughness which represents the measurements of the finely spaced micro-irregularities

on surface texture (*e.g.*, surface grooves produced by grinding/polishing). On average, for metals able to develop a passive layer, such as copper, a decrease in surface roughness can increase abiotic corrosion resistance (Alvarez et al., 2010; Abosrra et al., 2009; Burstein & Pistorius, 1995). However, the relationship between intrinsic properties of metallic substrate (i.e., roughness) and the rate of corrosion in the presence of microorganisms is seldom considered.

In this work, the effect of different surface roughness on the MIC of copper was evaluated. 3D optical profilometry, Field Emission Scanning Electron Microscopy (FE-SEM), Energy Dispersive X-Ray (EDX), X-ray Diffraction Analysis (XRD) and EDX X-ray attenuation pit depth analysis were used to investigate the corrosion morphology and product development. Corrosion rates were also calculated (ASTM Standard G1-03). Copper dissolution rates, copper toxicity, and biofilm yields were also measured to understand the effect of surface roughness on *Oleidesulfovibrio alaskensis* G20 growth. Results demonstrated that surface roughness did not significantly impact cellular growth or biofilm association but did impact the corrosion localization, extent, and mineralization associated with microbial growth, and the results suggest that modulation of surface properties could be an inexpensive approach to reduce copper MIC.

Materials and Methods

Preparation of Copper Coupons

Coupon finishes were selected based on the roughness attainable in standard machining operations under traditional (*i.e.*, milling) and non-traditional processes (*i.e.*, superfinishing) (Grzesik et al., 2010). C101 copper coupons with composition Cu-99.99%wt. (min) and oxygen 0.0005%wt. (max) were cut from a bar to the dimensions of 10x10x2mm using electrical discharge machining (EDM) process to minimize defects such as mechanical deformation that

may later influence the corrosion behavior. Coupons were then ground and polished on both sides to four different surface finishes: 400 US grit, 600 US grit, 800 US grit and 3-micron diamond suspension polishing using metallographic procedures with an Allied High Tech MetPrep 3 Grinder/Polisher equipped with a PH_3 power head. "As received" coupons without any surface modification were also used for comparison. To remove any polishing residue, ultrasonic cleaning was performed in a two-step process with 100% acetone (Fisher Chemical Lot#187993) and 100% methanol (Fisher Chemical Lot#217743) for 10 minutes each. Prior to abiotic and biotic exposures, all coupons were sterilized in a biosafety cabinet by dipping in ethanol solution (70% v/v) prepared with pure ethyl alcohol (Sigma-Aldrich Lot # SHBL 3646) and sterile nanopure water. This step was followed by exposure to UV light for 3 minutes for each side of the sample during drying in a biosafety cabinet.

Inoculum Preparation and Batch Exposure

The anoxic bacterial growth medium (LS4D) was prepared with 10.39 g/L PIPES buffer disodium salt (Sigma-Aldrich #P3768), 1.63 g/L MgCl2*6H_2O (Research Products International M24000, 1.07 g/L NH_4Cl, 0.09 g/L (Sigma-Aldrich #A9434). $CaCl_2$*2H_2O, 0.64 mg/L(Research Products International C36200) as previously described (Krantz et al., 2019). The pH of the medium was adjusted to 7.2 using a 2 M solution of HCl and 14 mL was anaerobically dispensed into each tube. The tubes were flushed with N_2/CO_2 (80%/20%), sealed with a butyl-rubber stopper, crimped with an aluminum cap, and autoclaved. A total volume of 0.24 mL sterilized pre-mix solution containing 0.01 mL of Thauers vitamins, 0.19 mL of trace minerals, and 0.03 mL of 1M potassium phosphate solution was added to each tube after sterilization. To conduct the experiments under an electron donor and acceptor balanced condition that uses 60 mM

lactate:30 mM sulfate as previously described (Franco et al., 2018). Resazurin (0.1% v/v) was also added to the medium solution to serve as a general indicator of the oxidative-reduction potential (ORP) (Krantz et al., 2019; Clark et al., 2006). For soluble copper toxicity with planktonic cells, bacterial cultures were centrifuged anoxically, washed with anoxic phosphate buffer, and re-suspended in anoxic growth medium as previously described (Franco et al., 2018).

For both abiotic and biotic exposures, three coupons for each type of surface finish, for a total of fifteen coupons, were anaerobically placed in sterile growth medium in Balch tubes using a biosafety cabinet with sparging of sterile N_2 gas. The tubes were then sealed with a sterile rubber stopper and crimped with an aluminum seal cap. Blank coupon tubes were co-incubated to ensure sterility during coupon processing. For biotic copper coupon exposures, *O. alaskensis* G20 was cultivated in previously prepared anaerobic tubes with LS4D medium for approximately 16 hours at 30°C and 0.1-0.2 ml of the culture was inoculated into each prepared tube containing the medium with one copper coupon. The same procedure was used for soluble copper toxicity assays without copper coupons and washed cell suspensions. The optical density (600 nm) was measured using a Thermo Scientific, Genesys 10S UV-VIS Spectrophotometer. For abiotic exposures, three coupons of the as received and of each type of surface finish were also anaerobically exposed to sterile LS4D media in batch tubes to ensure that no corrosion or surface deterioration occurred over the tested period.

Coupon Harvesting

Abiotic and biotic tubes were carefully placed into the fume hood after 7 days experiment period. The aluminum seal caps and stoppers were removed, the coupons removed and rinsed with sterile, anoxic medium, and quickly processed for different analyses. The post-incubation

coupons used for microscopy and 3D profilometry analysis were also placed in vacuumed tubes. Removal of the thin biofilms and of the mineral layer resulting from the exposures was performed by ultrasonic cleaning with hydrochloric acid (HCl) (Fisher Chemical Lot#179019) for 1 minute. Preliminary FE-SEM analyses were performed to confirm that this procedure did not introduce any additional surface damage which may later affect MIC evaluation.

Protein and Carbohydrate Assays

Protein concentrations of total biomass were measured using the Qubit Protein Assay Kit (Life Technologies, Eugene, Oregon, USA) on final time-point samples (Krantz et al., 2019). Hexose sugars were measured by the colorimetric cysteine–sulfuric acid method with glucose as the standard as previously described (Chaplin, 1986). Briefly, vortexed samples were heated at 100ºC for 3 minutes then rapidly cooled to room temperature using an ice bath. Samples and standards (300 µL) were transferred into a 96 well plate and absorbance was measured at 415 nm.

Surface Analysis, Determination of Pit Depth and Mineral Layer Composition

A Filmetrics Profilm 3D Optical Profilometer was used to evaluate the surface topography, the distribution of asperities and the surface roughness of as received and prepared copper coupons prior to abiotic and biotic exposures. No further sample preparation was performed for the measurements. White light beam setting was used for the profilometer analysis. For the SEM imaging of all copper coupons, a ZEISS SUPRA 55VP FE-SEM microscope (Carl Zeiss Microimaging, GmbH, Gottingen) was used. No sample preparation was performed for the imaging of as received and prepared samples before exposure, while the

coupons surface morphologies and the pitting developed following biotic exposure were evaluated after the HCl cleaning process described previously.

To assess the distribution, thickness, and morphology of the formed mineral layer, analysis of metallographically prepared cross sections was also performed for all exposed samples. The coupons were attached to a thin glass slide using an epoxy resin (Epoxy bond 14; Allied High Tech Products). The cross-section side of the coupons were polished up to 1 micron diamond suspension polishing using Allied High Tech MULTIPREP Polishing system. EDX (Princeton Gamma-Tech, Inc, Rocky Hill, NJ) was used to evaluate the pit depth using the X-ray attenuation methodology on HCl cleaned coupons and to identify the elemental composition of the mineral layer of prepared cross sections as previously described (Chaplin, 1986). To further characterize the developed mineral layer, grazing incidence X-Ray diffraction GI-XRD analysis was performed using Bruker Nano Analytics D8 Advance XRD on all coupons after the biotic exposure experiments and prior to HCl cleaning. A grazing incidence angle of 0.8° was used for characterizing the thin mineral layer developed on all coupons after biotic exposures. Statistical analysis from the biotic exposure experiments was carried out using MiniTab 21.4 (MiniTab, LLC). Statistical significance was determined via Tukey simultaneous tests for differences of means to determine the effects of each surface finish on corrosion rates and pit depth.

Results

Optical Profilometry

In order to achieve copper surfaces with different roughness, polycrystalline copper surfaces were polished with 400, 600, 800 US grit as well as 3 μm diamond suspensions. The as-received samples are characterized by random distribution of surface features most likely

related to the manufacturing process of the copper bars (Figure 3.2a). A homogeneous distribution of unidirectional grinding marks is observed for the 400, 600 and 800 US grit (Figure 3.2 b-d) with asperities decreasing in size with increasing US grit values (Figure 3.2 b'-d'). Uniform distribution of asperities in the range 0.03-0.07 μm was observed for 3 μm diamond suspension polished samples. The surface roughness was highest for as-received material at approximately 13 μm and decreased 4-fold for the copper polished with 400 US grit (Table 3.2). The 600 US grit polished surface had 10-fold lower roughness, and the 800 US grit polish had over 70-fold lower roughness (Table 3.2). The surface polished with 3 μm diamond suspension had the lowest roughness that was over 200-fold lower than as-received copper (Table 3.2). The results demonstrated that polishing dramatically decreased surface roughness for polycrystalline copper, and that polishing with 800 US grit or 3 μm diamond suspensions resulted in roughness below the average cell size of *O. alaskensis* G20.

Microbial Growth

Many systems that use copper materials can experience semi-batch conditions where intermittent microbial growth and metabolite production can occur. Therefore, we performed batch growth experiments under sulfate-reducing conditions with the model sulfate-reducing bacterium, *Oleidesulfovibrio alaskensis* G20, in which cells could grow and also interact with the copper surfaces. The *O. alaskensis* G20 growth rate and biomass yield was not significantly different in the presence of the copper coupons with different surface finishes over the 7 d time period (Figure 3.1). The protein level for culture without a copper coupon was 94.8 μg/ml while the as-received coupon culture had a reduced level of 78.2 μg/ml (18% reduction in presence of copper coupon) (Table 3.1). The 400 US grit treated coupon had a slightly lower biomass yield

(20% lower compared to no copper) whereas the next three treatments (600, 800, and 3 μm) had biomass yields closer to the no-copper control (7 to 10% reduction in protein levels) (Table 3.1). The carbohydrate levels were more similar between treatments (within 5-10% of no copper controls) (Table3.1).

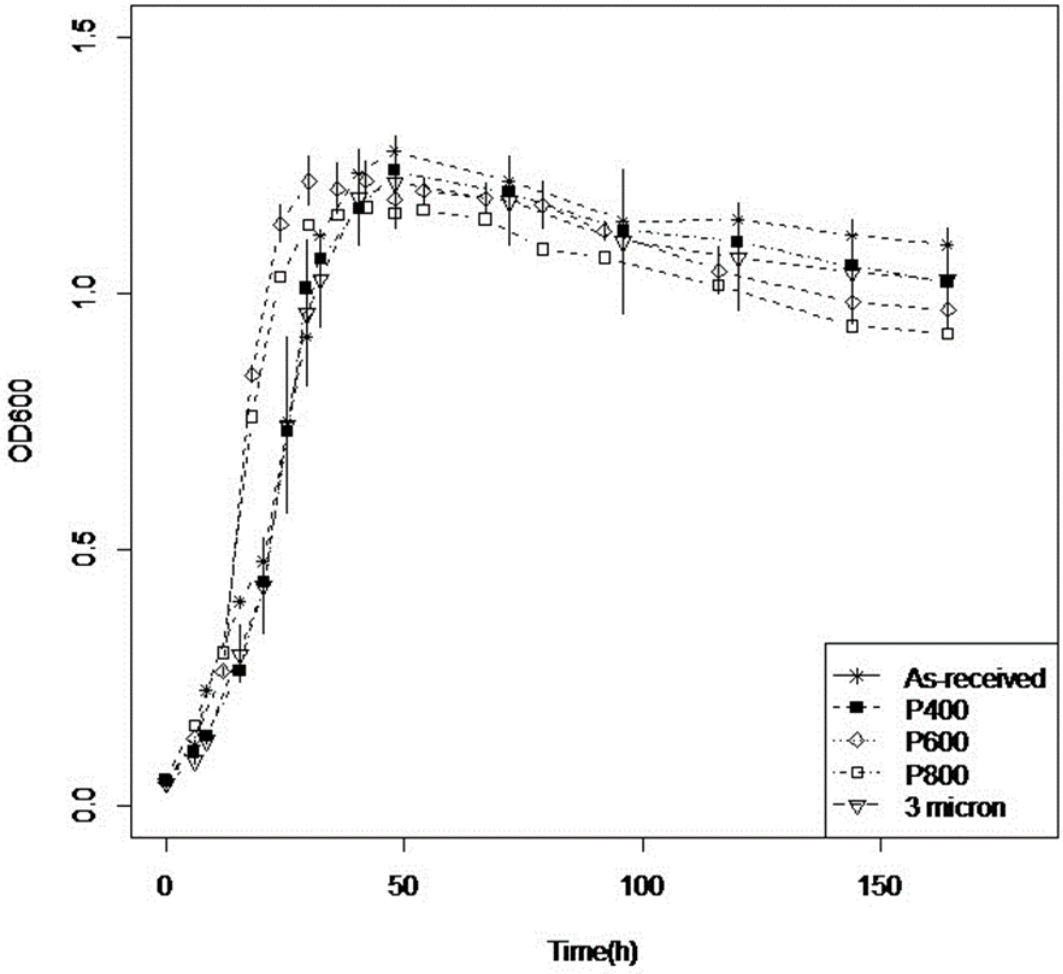


Figure 3. 1: (a) Growth of *Oleidesulfovibrio alaskensis* G20

Table 3. 1: Carbohydrate and protein contents in the suspension of Cu-free culture and for coupons prepared with different surface finish.

Factor	N	Carbohydrate Mean (mg/ml)	Carbohydrate StDev	Carbohydrate 95% CI	Protein Mean (µg/ml)	Protein StDev	Protein 95% CI
Cu-free control	3	2.247	0.256	(1.611, 2.884)	94.867	10.458	(68.887, 120.846)
As received	3	1.979	0.431	(0.908, 3.051)	78.200	0.872	(76.034, 80.366)
400 US Grit	3	2.232	0.698	(0.497, 3.967)	75.267	5.220	(62.298, 88.235)
Factor	N	Carbohydrate Mean (mg/ml)	Carbohydrate StDev	Carbohydrate 95% CI	Protein Mean (µg/ml)	Protein StDev	Protein 95% CI
800 US Grit	3	2.273	0.158	(1.880, 2.666)	88.833	2.139	(83.521, 94.146)
3 µm diamond suspension	3	2.251	0.133	(1.921, 1.582)	85.800	7.006	(68.397, 103.203)

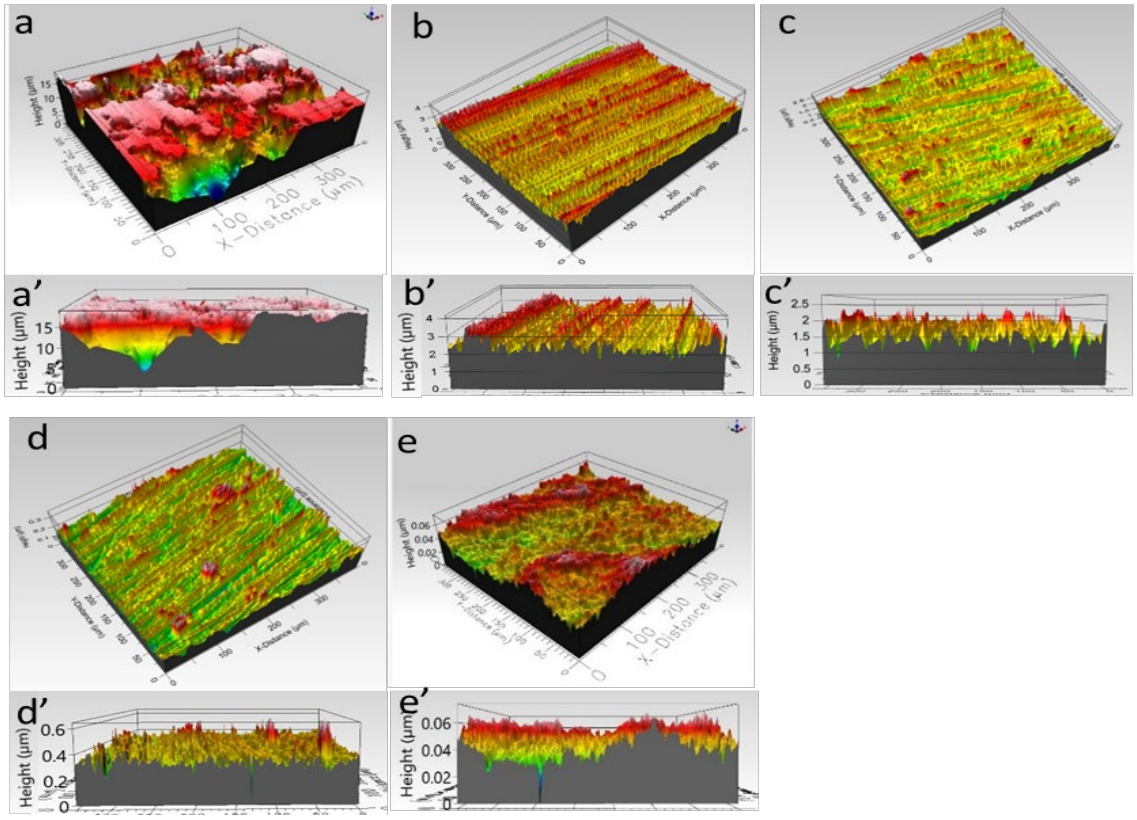


Figure 3. 2: 3D topography of copper samples prepared with different surface finish and corresponding distribution of asperities (a-a') as received, (b-b') 400 US grit, (c-c') 600 US grit (d-d') 800 US grit, (e-e') 3 µm diamond suspension polishing.

Table 3. 2: Surface roughness of copper samples prepared with different surface finish.

Surface finish	Roughness (µm)
As received	12.94
400 US grit	2.95
600 US grit	1.23
800 US grit	0.18
3 µm diamond suspension	0.06

FE-SEM analyses

Coupons with different surface roughness were incubated in growth medium without cells (abiotic control) for 7 d. Coupon mass loss was negligible and surface observations via Field Emission-Scanning Electron Microscopy showed surfaces that were unaltered (Figure 3.3). In addition, surfaces were similar to topographies observed via 3D optical profilometer pre-incubation (Figure 3.2 a-e). After 1 week of incubation with *O. alaskensis* G20 cells, uniform mineral growth was observed for the as-received samples (Figure 3.4a). The 400 US grit finished samples were characterized by random distributions of small and large sized individual crystals (Figure 3.4b). For the 600 US grit, 800 US grit and 3µm diamond suspension finished samples, the surface morphology presented individual crystals regions comparable to the 400 US grit samples along with dense mineral regions with a morphology comparable to the as-received samples (Figures 3.4 c-e). For the 3 µm diamond suspension finished samples both regions are characterized by smaller sized crystals when compared to the other surface finishes (Figure 3.4 e). In order to determine thickness of mineral layer on different surfaces, FE-SEM cross-sections were imaged for all surface finishes. For all samples, the cross-sectional morphology consisted of a continuous mineral layer in close proximity to the copper surface with scattered individual crystals varying in size (Figure 3.5 a-e). The as-received surfaces had a more even coverage that was approximately 1 to 3 µm thick and appeared to fill-in the asperity of the surface (Figure 3.5a). For the 400, 600, and 800 US girt treated samples, the mineral film did not appear to be as tightly associated, and the film thickness was not as uniform (Figure 3.5b-3.5d). Interestingly, the 3 µm diamond-treated sample did not have uniform coverage, and any mineral film coverage was localized to specific areas (Figure 3.5e).

The mineral layer was observed to be compact and non-porous for the as-received, and 3 μm polished samples with a thickness of approximately 3 μm and 0.5 μm, respectively (Figure 6a and e). The 400 US grit finished samples showed an overall dense approximately 2 μm thick layer with the presence of a few small diameter pores (< 1μm) randomly distributed (Figure 3.6b). The same composition, identified by the presence of Cu and S, was revealed for all mineral layers as well as for the scattered crystals (Figures 3.6a, b, and e). For the 600 and 800 US grit finished samples, a compound layered structure was revealed. The 600 US grit finished samples were characterized by an approximately 1μmdense layer in contact with the copper surface followed by a layer formed of approximately 3 μm sized adjacent single crystals (Figure 3.6c). The 800 US grit finished samples showed an approximately 2.5 μm thick layer with a porous-like morphology in contact with the copper surface followed by an approximate 1 μm dense top layer (Figure 3.6d). The Cu and S based composition was confirmed for both the 600 US grit and the 800 US grit finished samples in the compound layers as well as the single crystals. For the 800 US grit finished samples, a Cu-enriched region was observed between the porous-like and the dense portions of the compound layer (Figure 3.6d).

The mineral film layer was removed from biotic exposed coupons via HCl cleaning (REF) in order to discern underlying surface deterioration/degradation. When compared to Figures 3.3a-e (after abiotic exposure), uniform corrosion along with distributed pitting corrosion was observed for all samples. The size and distribution of the pitting varied with the surface finish. Nesting pits were observed for the as-received and the 400 US grit finished samples. For both finishes, the external pit diameter was between 3 and 6 μm while the internal pit diameter was estimated between 1 and 3 μm (Figures 3,7a and 3.7b). For the 600 US grit and the 800 US

grit finished samples, single pits with a diameter between 1 and 2 µm were observed over the entire surface (Figures 3.7c and 3.7d). No specific trend was observed in the pit distribution. Intergranular corrosion was observed for the 3 µm diamond suspension polished samples with little degradation (pits <1µm) randomly distributed on the actual grains (Figure 3.7e).

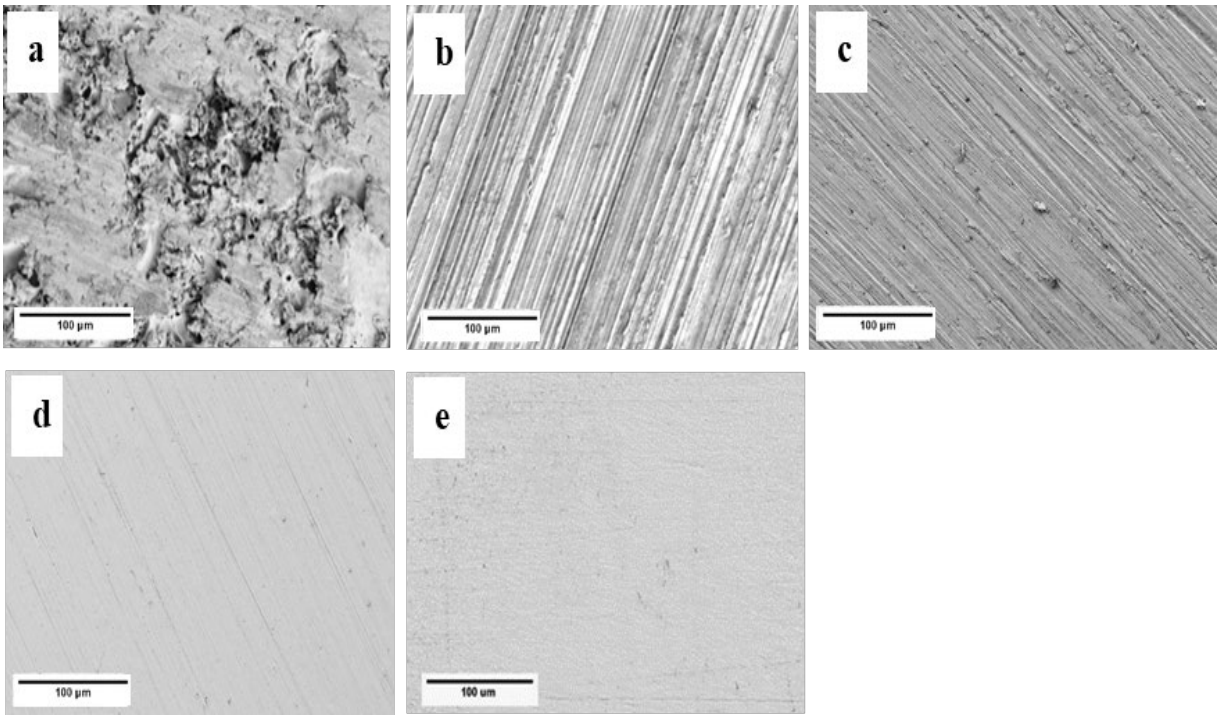


Figure 3. 3: FE-SEM imaging of coupon surface after abiotic exposure for 7 days to sterile and autoclaved LS4D media (a) As received, (b) 400 US grit, (c) 600 US grit, (d) 800 US grit and (e) 3µm diamond suspension finish.

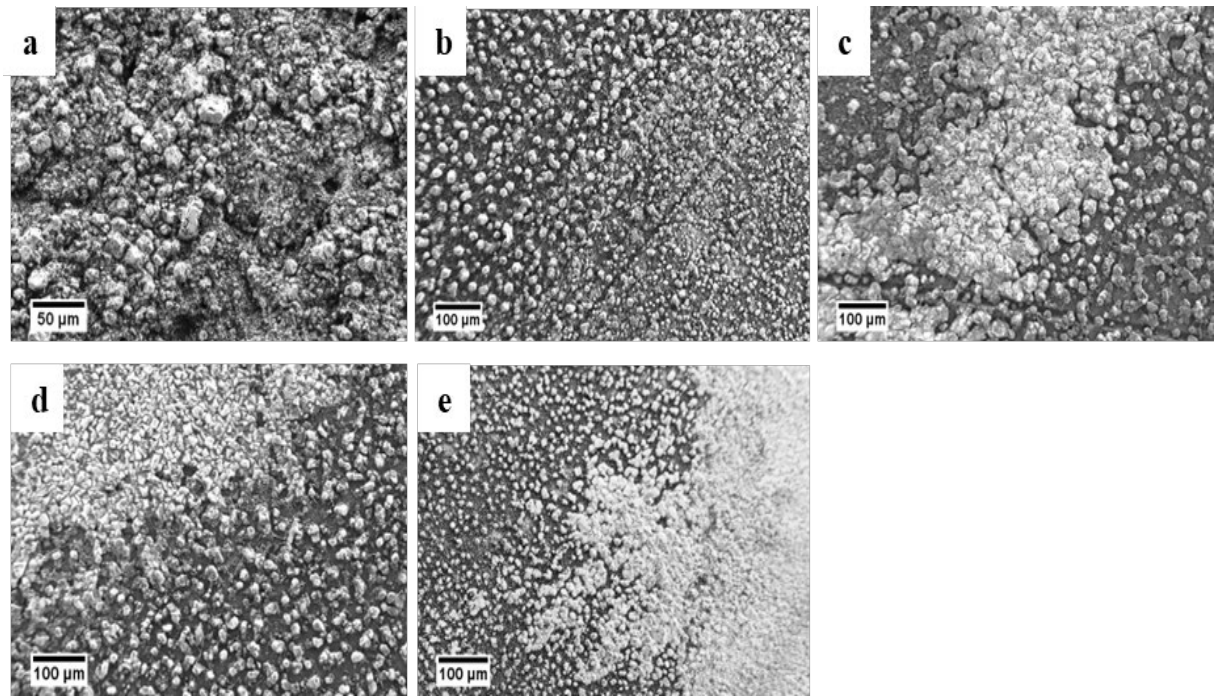


Figure 3. 4: Mineral growth on different surface finish copper coupons after 1 week of batch exposure to *O. alaskensis* G20. as received (a), 400 US grit (b), 600 US grit (c), 800 US grit (d) 3 µm diamond suspension polishing (e).

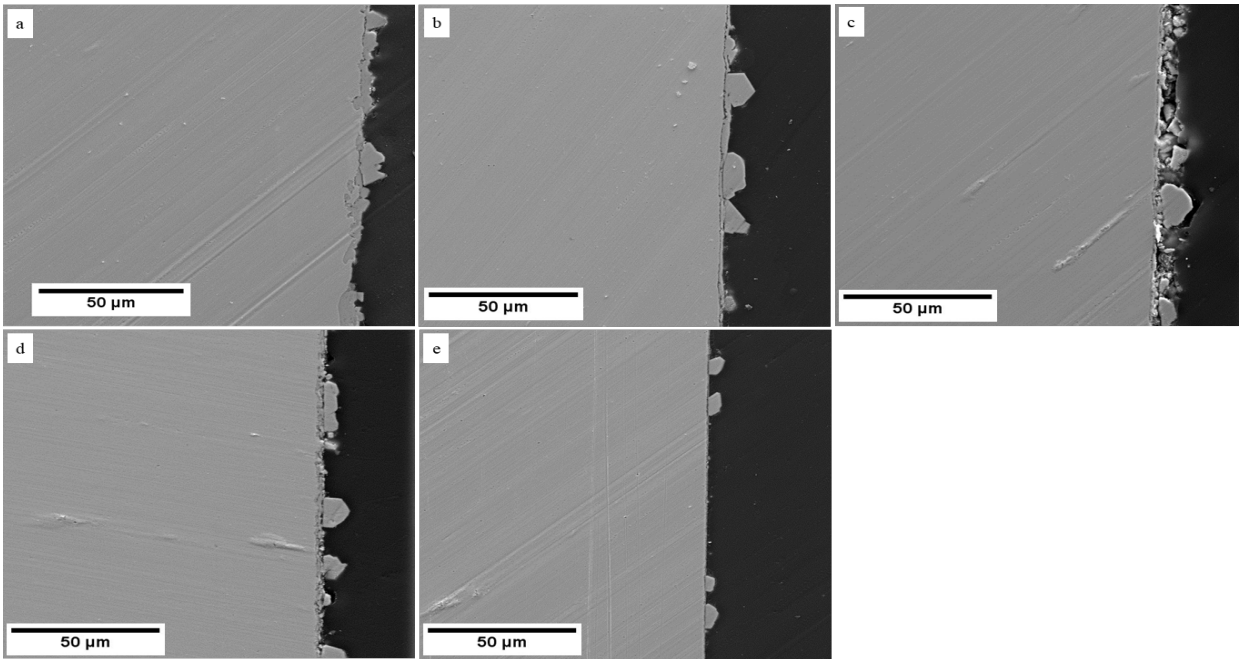


Figure 3. 5: FE-SEM imaging of copper coupons cross sections after 1 week batch exposure to *O. alaskensis* G20 as received (a), 400 US grit (b), 600 US grit (c), 800 US grit (d) 3 µm diamond suspension (e) finish.

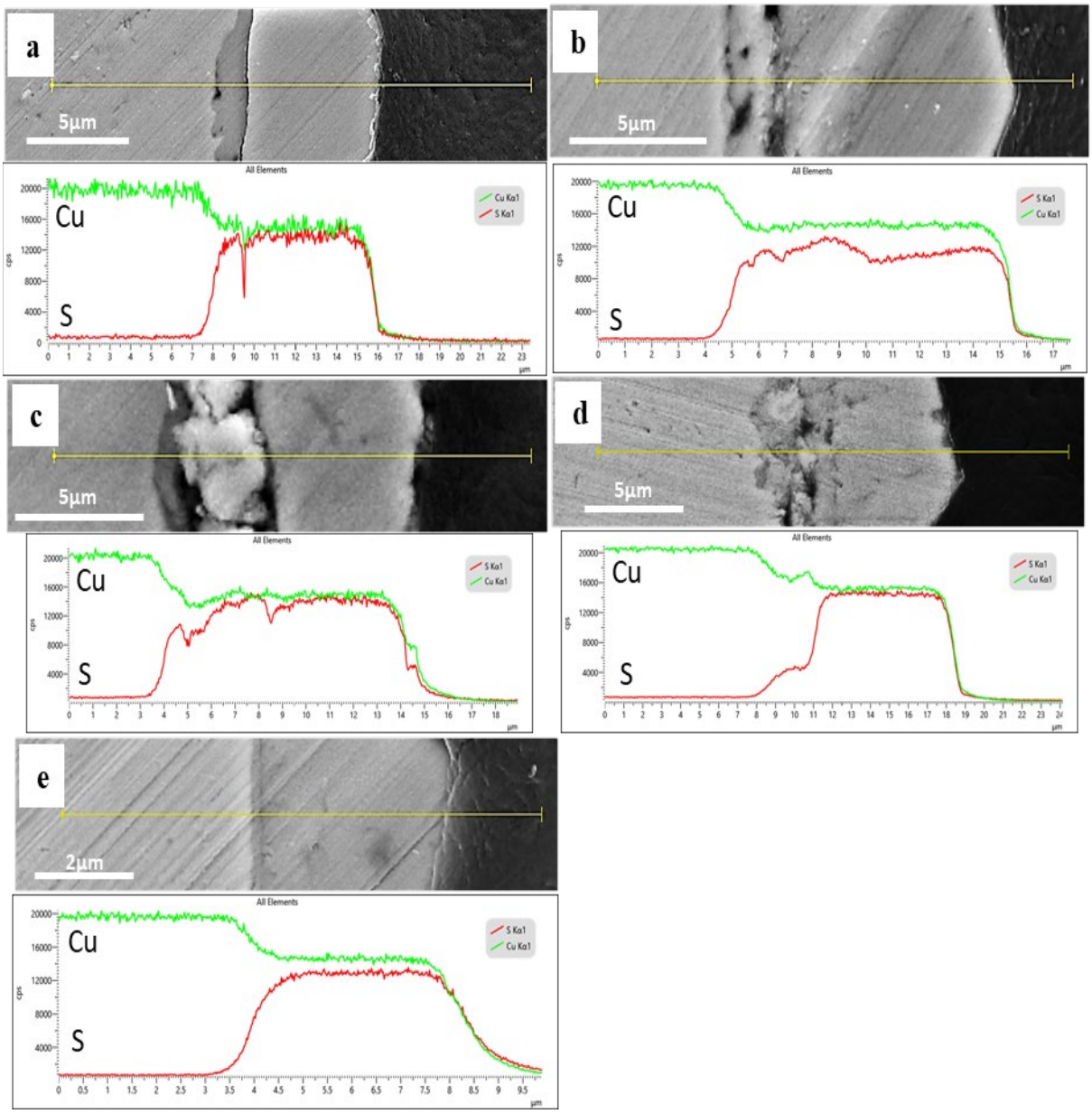


Figure 3. 6: Cross section morphology and EDX line scan date of as received (a) 400 US grit (b) 600 US grit (c) 800 US grit (d) and 3 µm diamond suspension (e) finished coupons after 1 week batch exposure to *O. alaskensis* G20

XRD Analysis

Mineral composition was determined for the mineral films on the different copper surfaces via x-ray diffraction (Figure 3.8). All mineral films contained copper (I) sulfide (Cu_2S)

also known as chalcocite. However, two different types of crystal structures were observed, namely monoclinic (low chalcocite) and hexagonal (high chalcocite). The presence of digenite Cu_xS with x=1.79-1.84 was also detected. The monoclinic phase (low-chalcocite) typically forms at a temperature below 104°C while the hexagonal phase (high-chalcocite) typically forms between 104° and 436°C (Kumar & Nagarajan, 2011; Wei et al., 2012). The transition between the two structures without involving elevated temperature is achievable by oxidative dissolution of copper from the low chalcocite structure (Kumar & Nagarajan, 2011), and the results suggested that *O. alaskensis* G20 could impact the formation of hexagonal chalcocite at the tested growth conditions (sulfate-reducing at lower temperatures in the presence of solid copper).

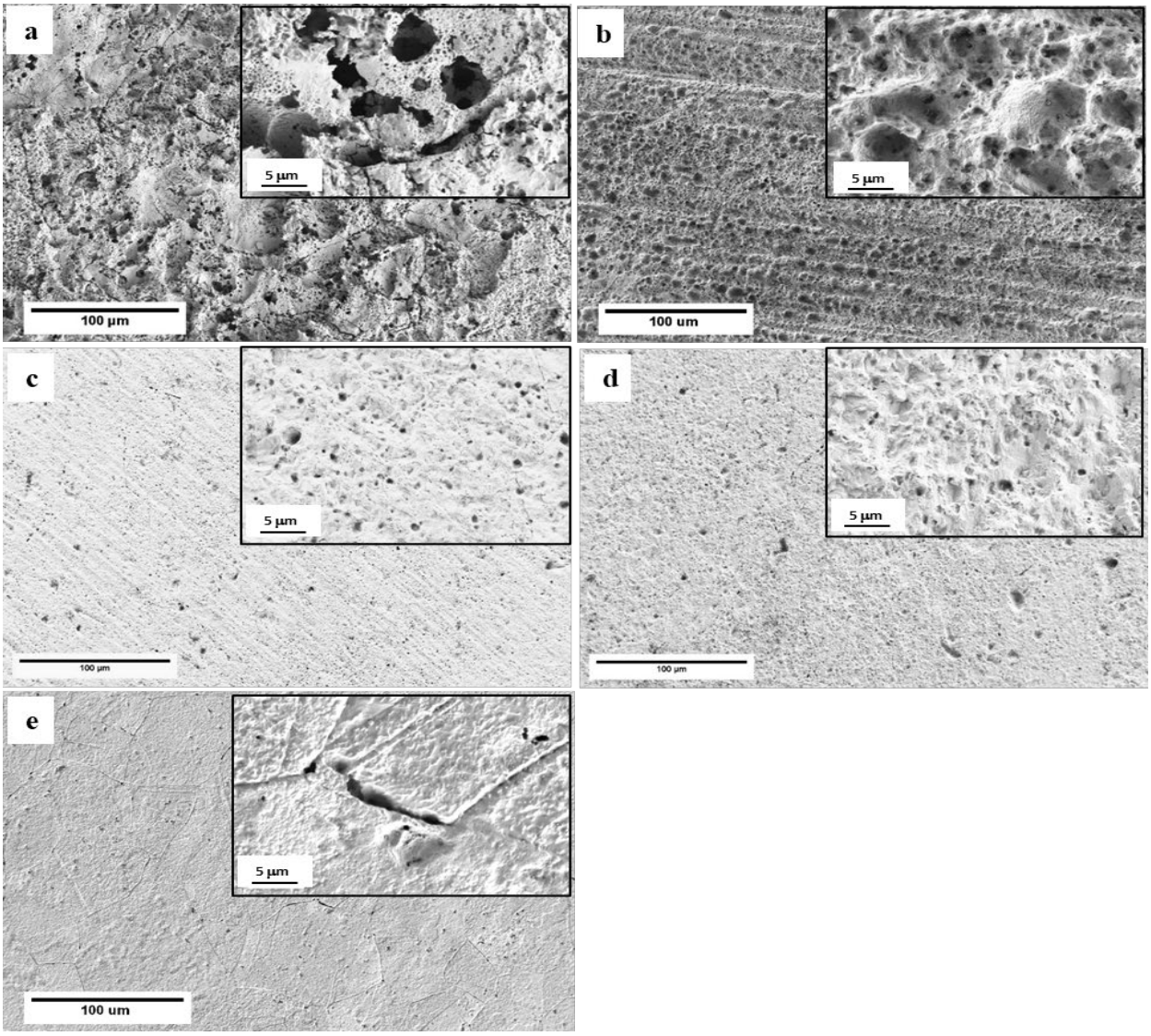


Figure 3. 7: FE-SEM imaging of as received (a) 400 US grit (b) 600 US grit (c) 800 US grit (d) and 3 µm diamond suspension (e) finished coupons after 1 week batch exposure to *O. alaskensis* G20 after removal of the mineral layer developed on the surface.

Corrosion Rates

The corrosion rates for all surface finishes were calculated from the mass loss measurement, as per ASTM Standard G1-03, using equation 6 (ASTM G1-03, 2017). Mass loss measurements were performed by weighing the coupons before abiotic and biotic exposure and after HCl cleaning. As noted above, weight loss was not observed after 1 week abiotic exposures

to sterilized LS4D medium. The corrosion rates calculated for the 400 US grit, 600 US grit, 800 US grit finished coupons and 3 mm diamond suspension polished coupons were reduced by 48%, 52%, 62% and 75% respectively, when compared to as-received coupons. The results indicated that a decrease in the surface roughness caused a decline in the overall copper corrosion rates.

$$Corrosion\ Rate(\frac{mm}{year}) = \frac{8.76\times10^4\times Mass\ loss(g)}{Area\ (cm^2)\times Time\ of\ exposure\ (hours)\times Density(\frac{g}{cm^3})} \quad (6)$$

Table 3. 3: Copper coupon corrosion rates calculated for different surface finish after biotic exposure to *O. alaskensis* G20 for 1 week. N is the number of samples tested per each surface finish, the "mean" is the average measured corrosion rate, "StDev" is the standard deviation and "95% CI" is the 95% confidence interval recorded for the as-received coupons and for each surface finish.

Factor	N	Mean (mm/year)	StDev	95% CI
As Received	3	0.41	0.06	(0.2659, 0.5488)
400 US grit	3	0.21	0.09	(0.0719, 0.3549)
600 US grit	3	0.19	0.19	(0.052, 0.335)
800 US grit	3	0.16	0.03	(0.0137, 0.2967)
3-micron diamond suspension	3	0.10	0.11	(-0.0387, 0.2443)

Pooled StDev = 0.109978

The Tukey simultaneous test for differences of means was also performed on the corrosion rates. The adjusted p-values of the as-received samples and the 400 US grit, 600 US grit and 800 US grit finished samples are greater than 0.05 which indicated that the variation observed in the corrosion rates was not statistically significant while, the adjusted p-value calculated for the 3µm diamond suspension polished samples was less than 0.05 indicating that

the difference observed in the corrosion rate for this specific surface finish was statistically significant. This indicated the surface roughness, as summarized in Table 3.2, did not have a significant effect on the corrosion rate until it was decreased from 12.94 µm (as-received samples) to 0.058 µm (3 µm diamond suspension polished samples) which corresponds to a highly finished surface (e.g. superfinishing).

Table 3. 4: Tukey simultaneous tests for differences of means performed on the measured corrosion rates calculated for different surface finish after biotic exposure to *O. alaskensis* G20 for 1 week

Difference of Levels	Difference of Means	SE of Difference	95% CI	T-Value	Adjusted P-Value
400 US grit - As Received	-0.1940	0.0898	(-0.4892, 0.1013)	-2.16	0.269
600 US grit - As Received	-0.2137	0.0898	(-0.5090, 0.0816)	-2.38	0.198
800 US grit - As Received	-0.2522	0.0898	(-0.5474, 0.0431)	-2.81	0.105
3-micron - As Received	-0.3046	0.0898	(-0.5998, -0.0093)	-3.39	0.043
600 US grit - 400 US grit	-0.0197	0.0898	(-0.3150, 0.2755)	-0.22	0.999
800 US grit - 400 US grit	-0.0582	0.0898	(-0.3535, 0.2371)	-0.65	0.963
3-micron - 400 US grit	-0.1106	0.0898	(-0.4058, 0.1847)	-1.23	0.735
800 US grit - 600 US grit	-0.0385	0.0898	(-0.3337, 0.2568)	-0.43	0.992
3-micron - 600 US grit	-0.0909	0.0898	(-0.3861, 0.2044)	-1.01	0.844
3-micron - 800 US grit	-0.0524	0.0898	(-0.3476, 0.2429)	-0.58	0.975

Individual confidence level = 99.18%

Pit Depth Evaluation

The pit depth evaluation was performed using the X-ray attenuation methodology in EDX spectra as previously described (Chaplin, 1986). Pits were randomly selected on the coupon surfaces and a minimum of eight pits were evaluated for each surface finish. Multiple measurements (a minimum of three) were conducted on the same pit to minimize uncertainties introduced by the X-ray production statistics. The statistical evaluation performed on the corrosion rates was duplicated on the evaluated pit depth. The results showed that the 400 US grit sample had a 53% reduction in pit depth compared to the as-received coupon (Table 3.5). The 600 and 800 US grit samples had 75% and 58% reduction in pit depth, respectively, compared to the as-received coupon while the 3 µm diamond suspension polished coupons had a 68% reduction compared to the as-received coupons ($p<0.05$) (Table 3.6). The other treatments were not statistically significant from each other (Tukey simultaneous test).

Table 3. 5: Pit depth measurements performed on copper coupons with different surface finish after biotic exposure to *O. alaskensis* G20 for 1 week

Factor	N	A total of EDX spectrum	Mean (mm)	StDev	95% CI
As Received	10	30	4.303	1.924	(3.597, 5.010)
400 US	9	27	2.028	0.478	(1.284, 2.773)
600	8	24	1.066	0.736	(0.277, 1.856)
800	10	30	1.785	0.785	(1.078, 2.491)
3micron	10	30	1.376	0.880	(0.670, 2.082)

Pooled StDev = 1.10672

Table 3. 6: Tukey simultaneous tests for differences of means performed on the pits' depth evaluated for different surface finish after biotic exposure to O. alaskensis G20 for 1 week

Difference of Levels	Difference of Means	SE of Difference	95% CI	T-Value	Adjusted P-Value
400 US – As Received	-2.275	0.509	(-3.724, -0.826)	-4.47	0.001
800 - As Received	-2.519	0.495	(-3.929, -1.108)	-5.09	0.000
3micron - As Received	-2.928	0.495	(-4.338, -1.517)	-5.91	0.000
600 - 400 US	-0.962	0.538	(-2.494, 0.571)	-1.79	0.394
800 - 400 US	-0.243	0.509	(-1.692, 1.206)	-0.48	0.989
3micron - 400 US	-0.652	0.509	(-2.101, 0.797)	-1.28	0.703
800 - 600	0.718	0.525	(-0.778, 2.214)	1.37	0.651
3micron - 600	0.310	0.525	(-1.186, 1.806)	0.59	0.976
3micron - 800	-0.409	0.495	(-1.819, 1.002)	-0.83	0.921

Individual confidence level = 99.32%

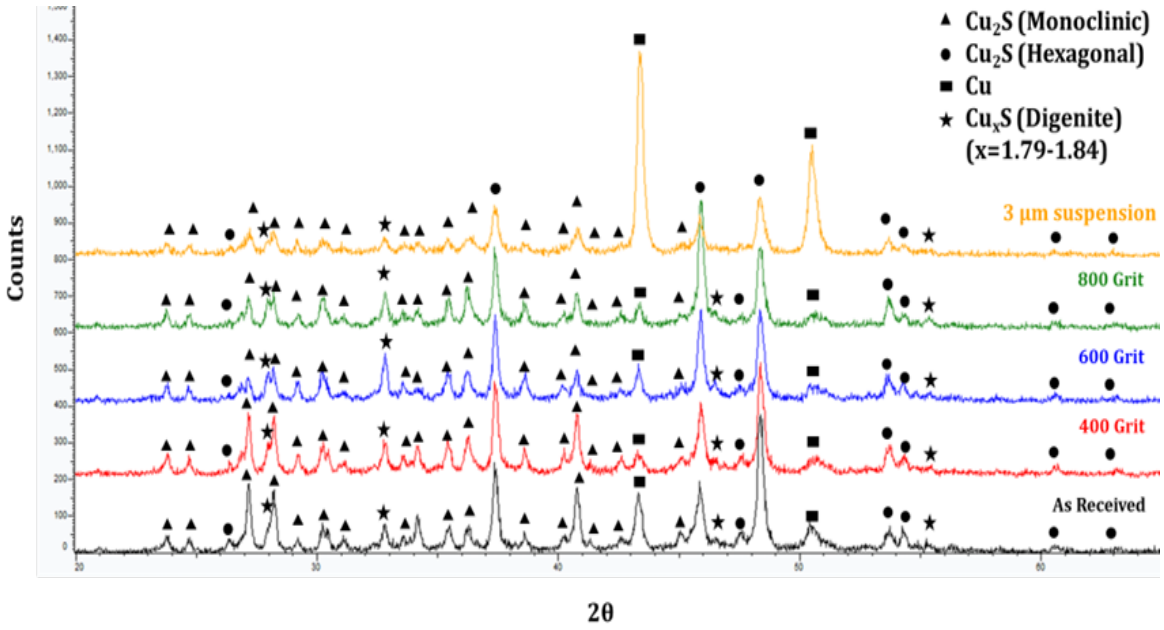


Figure 3. 8: XRD spectra comparison for as received, 400 US grit, 600 US grit, 800 US grit and 3µm diamond suspension polished coupon surface after biotic exposure to *O. alaskensis* G20 for 1 week.

Discussion

Mineral Layer Development and Corroded Surface Morphology

Although Cu(I) dissolution produces the majority of reported corrosion products, Cu(II) dissolutions can also be a sign of corrosion (Wei et al., 2012). A similar trend was observed in copper dissolution concentrations in abiotic experiments with the different surfaces. The average Cu^{2+} dissolution concentrations (µM) were reduced by 15%, 19%, 17% and 28% for 400 US grit, 600 US grit, 800 US grit and 3 µm diamond suspension coupons when compared to as-received coupons. These results suggest that the altered surface roughness impacts copper dissolution under the tested conditions that could ultimately impact mineral formation at the copper surface in the presence of *O. alaskensis* G20. Due to the difficulty of determining Cu^{2+} ions in

suspension cultures due to sulfide production, the copper dissolution concentrations and rates were not measured for biotic tubes.

3 µm Diamond Suspension Finish.

Despite the statistical analyses that indicated that surface roughness did not have a significant effect on the corrosion rate until highly polished surface finish was achieved (3 µm diamond polish), the FE-SEM analyses showed that roughness affected the mineral growth morphology at the coupon surface as well as the corroded surface morphology after the mineral layer was removed. The surface roughness decreased with a decrease in the size of asperities resulting from smoother surface finish (Figures 3.2a'- e'), and such asperities or irregularities increase the overall interfacial area that may act as micro-reaction sites for corrosion. This can be impacted by both preferential local dissolution of the substrate and by trapping corrosion products (Grzesik et al., 2010) (Zuo et al., 2002).

The large interfacial area generated by the higher values of the surface roughness on the as-received coupons may enhance the Cu diffusive flux from the coupon, as well as cause high local [HS^-] within the asperities. In this condition, the kinetics of reactions 4 and 5 are controlled by the diffusion of Cu(I) from the coupon (Chen et al., 2011; Chen et al., 2017) and may have supported the rapid development of a homogeneous and non-porous crystalline deposit approximately 3 µm thick, visible in cross-sections (Figures 3.5a and 3.6a). This phenomenon may also be responsible for the highest corrosion rates (Table 3.3) and the complex nesting pits' morphology (Figure 3.7a) when compared to the other surface finishes with reduced roughness.

On the contrary, the highly finished surface of the 3 µm diamond suspension polished coupons was characterized by a very flat morphology where the availability of any feature with a

volume sufficient to generate a preferential corrosion site was negligible (Figure 3.2a), and these features likely contributed to the reduced corrosion rate (75%) (Table 3.3) when compared to the as-received coupons. This reduction was well reflected by the development of an approximately 0.5 μm thick, well adherent, non-porous and uniform mineral layer shown in the cross sections (Figures 3.5e and 3.6e). The interfacial kinetics governed by the release of Cu(I) (reaction 4) were likely slower when compared to the as-received coupons because of the reduced interfacial area. The pitting attack was also reduced for the 3 μm diamond suspension coupons as even small diameter pits were scarcely observed over the surface (Figure 3.7e).

Despite this remarkable reduction achieved in the corrosion rate and pitting attack, intergranular corrosion was observed for the smoothest surface (Figure 3.7e). The flat surface resulting from the polishing process was free of preparation artifacts (Figure 3.3e) hence the copper microstructure was exposed while it was "masked" by the higher roughness for the other finishes. Within the microstructure, the grain boundaries presented higher atomic disorder which likely caused the increased chemical reactivity responsible for the preferential attack. While denser crystalline regions of the mineral film were developed in some areas over the surface (Figure 3.4e), this phenomenon did not seem to significantly affect the growth of the mineral layer as the variation in its thickness along the cross section was negligible (Figure 3.4e). However, as previous research in abiotic conditions showed that non-uniform growth of the mineral resulted in micro-galvanic couples between the more-dense cathodic and less-dense anodic areas (Chen et al., 2017), the mineral layer may have enhanced the corrosive attack at the grain boundaries by accelerating the Cu(I) dissolution and transport from the anodic locations to cathodic locations. The presence of intergranular corrosion should be carefully considered

particularly if the material's application involves the occurrence of mechanical stresses (*e.g.*, pipeline) as it may lead to catastrophic failure of a system.

400 US Grit Finishing.

After exposure, the 400 US grit surface was characterized by alternating regions of large and small sized individual crystals (Figure 3.4b) which do not present any apparent trend. An approximate 2 μm thick, well adherent, and non-porous mineral film is formed along the cross section of the coupons (Figure 3.5b and 3.6b). The reaction kinetics presented for the as-received coupons also apply to this surface finish; the corrosion rate and localized pitting attacks were reduced (Tables 3.3 and 3.5) when compared to the as received coupons likely because of the decreased size of the asperities which resulted in a smaller interfacial area available to generate micro-reaction sites. The pitting attack seemed to be preferentially located along the grinding marks and the nesting pit morphology observed for the as received coupons persisted (Figure 3.7b).

It is generally accepted that as roughness increases, bacterial attachment and biofilm formation are facilitated as the interfacial area available for bacterial attachment is larger and provides a better scaffold for adhesion (Zheng et al., 2021; Yoda et al., 2014 Yu et al., 2016; Yao et al., 2020). Although improved bacterial adhesion was expected for the coupons presenting higher surface roughness namely, the as-received and 400 US grit coupons (Table 3.2), it is proposed that the growth of the uniform and dense mineral film had more impact than biofilm development because the corrosion of copper in a sulfide solution is rapid (Chen et al., 2011) and initiated as soon as HS^- was released to the environment by SRB.

600 US Grit and 800 US Grit Finishing.

For both 600 US grit and 800 US grit finishing, the asperities were evenly distributed over the coupon surface (Figures 3.2 c'-d'). As the overall volume of the preferential reaction sites was further reduced, the corresponding corrosion rates and localized pitting attacks were lowered when compared to the 400 US grit coupons (Tables 3.3 and 3.5) but remained higher than the 3μm diamond suspension polished coupons. For both finishes, after biotic exposure the surface presented a non-uniform mineral layer characterized by the presence of dense crystalline regions randomly distributed over the surface (Figures 3.4c-d). As described earlier, such a phenomenon may have resulted in the establishment of micro-galvanic couples where the denser regions acted as cathodes. The sustainment of these couples ultimately could have resulted in HS^- depletion from the solution (Chen et al., 2017).

For both the 600 and 800 US grit finishes, the cross sections revealed (Figures 3.5c-d) the presence of an adherent layer approximately 4μm thick characterized by a porous morphology (Figures 3.6c-d). This is typical of slower linear growth kinetics controlled by HS^- diffusion in the solution and of environments where the $[HS^-]$ is relatively low (Chen et al., 2017; King et al., 2017) which well agrees with an environment created by the presence of the previously described micro-galvanic couples. As the linear reaction kinetics are slower when compared to the parabolic ones, bacterial attachment and the development of the biofilm may become concurrent with the growth of the mineral layer. This phenomenon may change the surface morphology as well as the transport phenomena involved in mineral growth by possibly increasing the local HS^- concentration underneath the film and by creating additional preferential cathodic sites due to biological components (*e.g.*, EPS) that can bind copper ions (Geesey et al., 1986; Angell & Chamberlain, 1991).

For the 600 US grit finish, a non-porous 1µm thick layer in contact with the copper surface followed by a layer formed of approximately 3 µm sized adjacent individual crystals were observed (Figure 3.6c). The larger crystals likely resulted from slower linear kinetics when compared to the parabolic ones. As this compound layer was characterized by the presence of large pores and open interstices between crystals, HS^- would have diffused inward from the bulk solution to the copper surface. Due to the small volume of the pores, new micro-sites were likely created where the local [HS^-] concentration was higher than in the bulk liquid. In this condition, the reaction kinetics would be parabolic and would have supported the development of the dense internal ~ 1µm thick layer of Cu_2S.

For the 800 US grit finishing coupons, the cross sections showed an approximate 2.5 µm thick layer with a porous-like morphology in contact with the copper surface followed by an approximate 1 µm dense top layer (Figures 3.6d). The reaction kinetics were likely the same as the 600 US grit samples, however the release of Cu(I) (reaction 4) was slower because of the high surface finish, similarly to what was discussed for the 3µm diamond suspension polished coupons. The small porosity of the layer, along with the presence of the top dense deposit, would have hindered the inward diffusion of HS^-. Within the pores, the products of reaction 4 were still present; however, it is possible that Cl^- ions in solution increased the solubility of Cu as follows (Chen et al., 2017; Dou et al., 2020):

$$Cu(SH)_{ads} + 2Cl^- \rightarrow CuCl_2^- + HS^- \qquad (7)$$

This newly formed cuprous-chloro complex ion, would then precipitate as Cu_2S when transported from the pores to a region at the surface where the concentration of dissolved HS^- is higher according to the following reaction (Chen et al., 2010; Chen et al., 2017):

$$2CuCl_2^- + HS^- \rightarrow Cu_2S + 4Cl^- + H^+ \qquad (8)$$

This proposed mechanism would explain the presence of the top compact and non-porous mineral layer and is also supported by previous findings (Chen et al., 2014). For both the 600 US grit and the 800 US grit finished coupons, the pitting attack consisted of single small diameter pits distributed over the surface (Figures 3.7c-d), the nesting morphology was not observed.

Mineral Layer Composition

The presence of digenite, which was previously identified as the intermediate species for oxidative dissolution in sulfide environments, supports the low to high chalcocite transition according to reaction 9 (Zhang et al., 2020):

$$(2\text{-}x)\ Cu_2S + x\ H_2S \rightarrow 2Cu_{2-x}S + 2xH^+ + 2xe^- \qquad (9)$$

It is unlikely that the formation of digenite would occur earlier than the low chalcocite structure as its formation is not thermodynamically favorable (Wei et al., 2012). The presence of a developing biofilm which would cause increased local HS^- concentration may have also contributed to reaction 9. This reaction may occur within the EPS matrix, which is known to contain metal-binding sites and can facilitate metal-sulfide precipitation (Guibaud et al., 2003). Differences in the ability of each chalcocite structure to protect the substrate from further corrosion are yet to be determined.

Conclusions

This work evaluated the effect of different surface roughness achieved through metallographic grinding (400, 600 and 800 US grit) or polishing (3µm diamond suspension) on

the MIC of copper 101 caused by 1-week batch exposure to *O. alaskensis* G20. All surface finishes were compared to the as-received coupons. Overall, the following observations can be made: (i) Uniform corrosion along with pitting corrosion was observed for all surface finishes, (ii) a statistically significant change in the corrosion rate was found only when the surface roughness was decreased from ~13 µm(as received coupons) to approximately 0.06 µm(3µm diamond suspension polished coupons); (iii) however, intergranular corrosion was observed with the diamond suspension finish, (iv) a statistically relevant decrease in pit depth was found for all finishes when compared to the as-received sample with no specific trend for pit depth among the different surface finishes, and (v) a change in the surface roughness affected the growth kinetics and morphology of the Cu_2S layer, as well as the pitting morphology. With respect to the mineral layers, the as-received, 400 US grit finish and 3µm diamond suspension polished coupons were characterized by the presence of a dense Cu_2S layer likely resulting from rapid parabolic growth kinetics while a porous Cu_2S layer resulting from slower linear growth kinetics was observed for the intermediate finishes (600 and 800 US grit finished coupons). For the 600 and the 800 US grit finished coupons, a thin compact, non-porous layer was observed along with the porous one. For the 600 US grit finished coupons this layer developed at the interface with the copper substrate, while for the 800 finished coupons it grew as outer layer over the porous one. In both cases, the presence of such layers was related to the chemical species found in the pores of the adjacent layer and their diffusional flux. Complex pitting morphology consisting of nesting pits was observed for the as received and the 400 US grit finish coupons while single isolated pits were found for the 600 and 800 US grit finishes as well as for the 3 µm diamond suspension polished samples. The developed mineral layer was identified as Cu_2S (chalcocite) for all

coupons. However, monoclinic (low chalcocite) and hexagonal (high chalcocite) crystal structures were both observed, and the oxidative dissolution of low chalcocite required for the transition from the low to the high structure was confirmed by the presence of the intermediate product digenite. The mechanisms of chalcocite formation and its specific role within biofilms are not yet fully understood, and further research is needed to elucidate these processes.

Credit Authorship Contribution Statement

Amit Acharjee: formal analyses, investigation, data curation, writing-original draft Yagmur Keskin: formal analyses, investigation, data curation, writing-original draft Matthew Fields: conceptualization, methodology, validation, writing-review and editing, supervision, funding acquisition, project administration Brent Peyton: conceptualization, methodology, validation, writing-review and editing, supervision Roberta Amendola: conceptualization, methodology, validation, writing-original draft, writing-review and editing, supervision

Declaration of Competing Interest

We declare that we have no financial and personal relationships with other people or organizations that can inappropriately influence our work, there is no professional or other personal interest of any nature or kind in any product, service and/or company that could be construed as influencing the position presented in, or the review of, the manuscript entitled.

Acknowledgements

This work was financially supported by the United States National Science Foundation (NSF # 1920954).

References

Abosrra, L., Ashour, A. F., Mitchell, S. C., & Youseffi, M. (2009). Corrosion of mild steel and 316L austenitic stainless steel with different surface roughness in sodium chloride saline solutions. *Simulation of Electrochemical Processes III*. https://doi.org/10.2495/ecor090161

Alvarez, R. B., Martin, H. J., Horstemeyer, M. F., Chandler, Mei. Q., Williams, N., Wang, P. T., & Ruiz, A. (2010). Corrosion relationships as a function of time and surface roughness on a structural AE44 magnesium alloy. *Corrosion Science*, *52*(5), 1635–1648. https://doi.org/10.1016/j.corsci.2010.01.018

Angell, P., & Chamberlain, A. H. L. (1991). The role of extracellular products in copper colonisation. *International Biodeterioration*, *27*(2), 135–143. https://doi.org/10.1016/0265-3036(91)90005-c

ASTM G1-03. (2017). Standard Practice for Preparing, Cleaning, and Evaluating Corrosion Test Specimens. *B. Stand*, *3*(2). https://doi.org/https://doi.org/10.1520/G0001-03R17E01

Avci, R., Davis, B. H., Wolfenden, M. L., Kellerman, L. R., Lucas, K., Martin, J., & Deliorman, M. (2015). A practical method for determining pit depths using X-ray attenuation in EDX Spectra. *Corrosion Science*, *93*, 9–18. https://doi.org/10.1016/j.corsci.2014.12.018

Bard, A. J., Parsons, R., & Jordan, J. (2017). *Standard Potentials in Aqueous Solution*. https://doi.org/10.1201/9780203738764

Beech, I. B., & Gaylarde, C. C. (1999). Recent advances in the study of biocorrosion: An overview. *Revista de Microbiologia*, *30*(3), 117–190. https://doi.org/10.1590/s0001-37141999000300001

Brauer, J. I., Celikkol-Aydin, S., Sunner, J. A., Gaylarde, C. C., & Beech, I. B. (2017). Metabolomic imaging of a quaternary ammonium salt within a marine bacterial biofilm on Carbon Steel. *International Biodeterioration & Biodegradation*, *125*, 33–36. https://doi.org/10.1016/j.ibiod.2017.08.007

Burstein, G. T., & Pistorius, P. C. (1995). Surface roughness and the metastable pitting of stainless steel in Chloride Solutions. *CORROSION*, *51*(5), 380–385. https://doi.org/10.5006/1.3293603

Chaplin, M. F. (1986). Carbohydrate analysis - M. F. chaplin, J. F. Kennedy - Oxford ... https://global-oup-com.libproxy.ucl.ac.uk/academic/product/carbohydrate-analysis-9780199634491

Chen, J., Qin, Z., & Shoesmith, D. W. (2010). Kinetics of corrosion film growth on copper in neutral chloride solutions containing small concentrations of sulfide. *Journal of The Electrochemical Society*, *157*(10). https://doi.org/10.1149/1.3478570

Chen, J., Qin, Z., & Shoesmith, D. W. (2011). Long-term corrosion of copper in a dilute anaerobic sulfide solution. *Electrochimica Acta*, *56*(23), 7854–7861. https://doi.org/10.1016/j.electacta.2011.04.086

Chen, J., Qin, Z., & Shoesmith, D. W. (2014). Key parameters determining structure and properties of sulphide films formed on Copper Corroding in anoxic sulphide solutions. *Corrosion Engineering, Science and Technology*, *49*(6), 415–419. https://doi.org/10.1179/1743278214y.0000000188

Chen, J., Qin, Z., Martino, T., & Shoesmith, D. W. (2017). Non-uniform film growth and micro/macro-galvanic corrosion of copper in aqueous sulphide solutions containing chloride. *Corrosion Science*, *114*, 72–78. https://doi.org/10.1016/j.corsci.2016.10.024

Chen, J., Qin, Z., Wu, L., Noël, J. J., & Shoesmith, D. W. (2014). The influence of sulphide transport on the growth and properties of copper sulphide films on copper. *Corrosion Science*, *87*, 233–238. https://doi.org/10.1016/j.corsci.2014.06.027

Chen, S., Wang, P., & Zhang, D. (2014). Corrosion behavior of copper under biofilm of sulfate-reducing bacteria. *Corrosion Science*, *87*, 407–415. https://doi.org/10.1016/j.corsci.2014.07.001

Clark, M. E., He, Q., He, Z., Huang, K. H., Alm, E. J., Wan, X.-F., Hazen, T. C., Arkin, A. P., Wall, J. D., Zhou, J.-Z., & Fields, M. W. (2006). Temporal transcriptomic analysis as *desulfovibrio vulgaris* Hildenborough transitions into stationary phase during electron donor depletion. *Applied and Environmental Microbiology*, *72*(8), 5578–5588. https://doi.org/10.1128/aem.00284-06

Dou, W., Jia, R., Jin, P., Liu, J., Chen, S., & Gu, T. (2018). Investigation of the mechanism and characteristics of copper corrosion by sulfate reducing bacteria. *Corrosion Science*, *144*, 237–248. https://doi.org/10.1016/j.corsci.2018.08.055

Dou, W., Pu, Y., Han, X., Song, Y., Chen, S., & Gu, T. (2020). Corrosion of CU by a sulfate reducing bacterium in anaerobic vials with different headspace volumes. *Bioelectrochemistry*, *133*, 107478. https://doi.org/10.1016/j.bioelechem.2020.107478

Franco, L. C., Steinbeisser, S., Zane, G. M., Wall, J. D., & Fields, M. W. (2018). Cr(VI) reduction and physiological toxicity are impacted by resource ratio in desulfovibrio vulgaris. *Applied Microbiology and Biotechnology*, *102*(6), 2839–2850. https://doi.org/10.1007/s00253-017-8724-4

Geesey, G. G., Mittelman, M. W., Iwaoka, T., & Griffiths, P. R. (1986). Role of Bacterial Exopolymers in the Deterioration of Metallic Copper Surfaces. *Perform*, *25*, 37–40.

Grzesik, W., Kruszynski, B., & Ruszaj, A. (2010). Surface integrity of machined surfaces. *Surface Integrity in Machining*, 143–179. https://doi.org/10.1007/978-1-84882-874-2_5

Guibaud, G., Tixier, N., Bouju, A., & Baudu, M. (2003). Relation between extracellular polymers' composition and its ability to complex CD, Cu and Pb. *Chemosphere*, *52*(10), 1701–1710. https://doi.org/10.1016/s0045-6535(03)00355-2

Güngör, N. D., Çotuk, A., & Dışpınar, D. (2015). The effect of desulfovibrio sp.. Biofilms on corrosion behavior of copper in sulfide-containing solutions. *Journal of Materials Engineering and Performance*, *24*(3), 1357–1364. https://doi.org/10.1007/s11665-015-1388-2

Javaherdashti, R. (1999). A review of some characteristics of MIC caused by sulfate-reducing bacteria: Past, present and future. *Anti-Corrosion Methods and Materials*, *46*(3), 173–180. https://doi.org/10.1108/00035599910273142

Javed, M. A., Neil, W., McAdam, G., & Wade, S. A. (2016). MICROBIOLOGICALLY INFLUENCED CORROSION OF COPPER AND ITS ALLOYS. *Corros. Assoc. Paper*, *84*, 489.

King, F., Chen, J., Qin, Z., Shoesmith, D., & Lilja, C. (2017). Sulphide-transport control of the corrosion of copper canisters. *Corrosion Engineering, Science and Technology*, *52*(sup1), 210–216. https://doi.org/10.1080/1478422x.2017.1300363

Krantz, G. P., Lucas, K., Wunderlich, E. L.-, Hoang, L. T., Avci, R., Siuzdak, G., & Fields, M. W. (2019). Bulk phase resource ratio alters carbon steel corrosion rates and endogenously produced extracellular electron transfer mediators in a sulfate-reducing biofilm. *Biofouling*, *35*(6), 669–683. https://doi.org/10.1080/08927014.2019.1646731

Kumar, P., & Nagarajan, R. (2011). An elegant room temperature procedure for the precise control of composition in the Cu–S System. *Inorganic Chemistry*, *50*(19), 9204–9206. https://doi.org/10.1021/ic201133a

Lee, W., Lewandowski, Z., Nielsen, P. H., & Hamilton, W. A. (1995). Role of sulfate-reducing bacteria in corrosion of Mild Steel: A Review. *Biofouling*, *8*(3), 165–194. https://doi.org/10.1080/08927019509378271

Little, B. J., Blackwood, D. J., Hinks, J., Lauro, F. M., Marsili, E., Okamoto, A., Rice, S. A., Wade, S. A., & Flemming, H.-C. (2020). Microbially influenced corrosion—any progress? *Corrosion Science*, *170*, 108641. https://doi.org/10.1016/j.corsci.2020.108641

Liu, H., Gu, T., Zhang, G., Cheng, Y., Wang, H., & Liu, H. (2016). The effect of Magneticfield on biomineralization and corrosion behavior of carbon steel induced by iron-oxidizing bacteria. *Corrosion Science*, *102*, 93–102. https://doi.org/10.1016/j.corsci.2015.09.023

Perrin, D. D. (1982). *Ionisation Constants of Inorganic Acids and Bases in Aqueous Solution* (2nd ed.). Pergamon Press Ltd.

Pope, D. H., & Morris, I. E. A. (1995). Some experiences with microbiologically influenced corrosion of pipelines, Mater. *Perform*, *34*. https://doi.org/https://doi.org/10.2172/793996

Puigdomenech, I., & Taxen, C. (1970, January 1). *Thermodynamic data for copper. implications for the corrosion of copper under repository conditions*. inis.iaea.org. http://inis.iaea.org/Search/search.aspx?orig_q=RN%3A32010691

Sani, R. K., Peyton, B. M., & Brown, L. T. (2001). Copper-induced inhibition of growth of *desulfovibrio desulfuricans* G20: Assessment of its toxicity and correlation with those of zinc and lead. *Applied and Environmental Microbiology*, *67*(10), 4765–4772. https://doi.org/10.1128/aem.67.10.4765-4772.2001

Sarioğlu, F., Javaherdashti, R., & Aksöz, N. (1997). Corrosion of a drilling pipe steel in an environment containing sulphate-reducing bacteria. *International Journal of Pressure Vessels and Piping*, *73*(2), 127–131. https://doi.org/10.1016/s0308-0161(97)00022-7

Talha, M., Ma, Y., Kumar, P., Lin, Y., & Singh, A. (2019). Role of protein adsorption in the Bio Corrosion of metallic implants – a review. *Colloids and Surfaces B: Biointerfaces*, *176*, 494–506. https://doi.org/10.1016/j.colsurfb.2019.01.038

Trevors, J. T., & Cotter, C. M. (1990). *Review Copper toxicity and uptake in microorganisms*.

Wagner, P., & Little, B. (1993). *Impact of Alloying on Microbiologically Influenced Corrosion-A Review*.

Wang, D., Liu, J., Jia, R., Dou, W., Kumseranee, S., Punpruk, S., Li, X., & Gu, T. (2020). Distinguishing two different microbiologically influenced corrosion (MIC) mechanisms using an electron mediator and hydrogen evolution detection. *Corrosion Science*, *177*, 108993. https://doi.org/10.1016/j.corsci.2020.108993

Wang, H., Ju, L.-K., Castaneda, H., Cheng, G., & Zhang Newby, B. (2014). Corrosion of carbon steel C1010 in the presence of iron oxidizing bacteria acidithiobacillus ferrooxidans. *Corrosion Science*, *89*, 250–257. https://doi.org/10.1016/j.corsci.2014.09.005

Wei, S. H., Xu, Q., Huang, B., Zhao, Y., Yan, Y., & Noufi, R. (2012). tability and Electronic Structures of CuxS Solar Cell Absorbers: Preprint, in: IEEE Photovolt. Spec. Conf. Austin, TX.

Yao, W.-L., Lin, J. C., Salamanca, E., Pan, Y.-H., Tsai, P.-Y., Leu, S.-J., Yang, K.-C., Huang, H.-M., Huang, H.-Y., & Chang, W.-J. (2020). Er,CR:YSGG laser performance improves biological response on titanium surfaces. *Materials*, *13*(3), 756. https://doi.org/10.3390/ma13030756

Yoda, I., Koseki, H., Tomita, M., Shida, T., Horiuchi, H., Sakoda, H., & Osaki, M. (2014). Effect of surface roughness of biomaterials on Staphylococcus epidermidis adhesion. *BMC Microbiology*, *14*(1). https://doi.org/10.1186/s12866-014-0234-2

Yu, P., Wang, C., Zhou, J., Jiang, L., Xue, J., & Li, W. (2016). Influence of surface properties on adhesion forces and attachment of*streptococcus mutans*to zirconia*in vitro*. *BioMed Research International*, *2016*, 1–10. https://doi.org/10.1155/2016/8901253

Yuan, S., Liang, B., Zhao, Y., & Pehkonen, S. O. (2013). Surface Chemistry and corrosion behaviour of 304 stainless steel in simulated seawater containing inorganic sulphide and sulphate-reducing bacteria. *Corrosion Science*, *74*, 353–366. https://doi.org/10.1016/j.corsci.2013.04.058

Zhang, Y., Zhao, H., Qian, L., Sun, M., Lv, X., Zhang, L., Petersen, J., & Qiu, G. (2020). A brief overview on the dissolution mechanisms of sulfide minerals in acidic sulfate environments at low temperatures: Emphasis on electrochemical cyclic voltammetry analysis. *Minerals Engineering*, *158*, 106586. https://doi.org/10.1016/j.mineng.2020.106586

Zheng, S., Bawazir, M., Dhall, A., Kim, H.-E., He, L., Heo, J., & Hwang, G. (2021). Implication of surface properties, bacterial motility, and hydrodynamic conditions on bacterial surface sensing and their initial adhesion. *Frontiers in Bioengineering and Biotechnology*, *9*. https://doi.org/10.3389/fbioe.2021.643722

Zuo, Y., Wang, H., & Xiong, J. (2002). The aspect ratio of surface grooves and metastable pitting of stainless steel. *Corrosion Science*, *44*(1), 25–35. https://doi.org/10.1016/s0010-938x(01)00039-7

CHAPTER FOUR

RESPONSE OF OLEIDESIULFOVIBRIO ALASKENSIS BIOFILM GROWN ON COPPER (101) IN A DYNAMIC ENVIRONMENT

Description of Study

Sulfate-reducing bacteria (SRB) have increased activity in environments abundant in sulfates, such as marine ecosystems, where they perform an essential role in linking the sulfur and carbon cycles. SRB are recognized for the ability to generate robust biofilms on metallic surfaces in dynamic environments and contribute significantly to microbially-influenced corrosion (MIC) dependent upon biofilm distribution and density. Furthermore, the existence of electron acceptors and donors at unbalanced ratios can influence the growth and activity of SRB and can influence the extent and rate of metal interactions, including MIC. The present study investigated the corrosion of polycrystalline copper 101 when exposed to *Oleidesulfovibrio alaskensis* G20 for different durations of 7, 9, and 14 days within a CDC biofilm reactor system. Protein and carbohydrate measurements on copper and glass coupons increased for days 9 and 14, compared to day-7, likely due to a continuous inflow of nutrients and outflow of planktonic cells. However, the carbohydrate to protein ratio was in a lower range for copper than the ratio for the glass coupons. In terms of corrosion rates, there was a marked increase in biotic conditions, with rates rising by 187.5% and 412.5% for days 9 and 14 compared to day 7, significantly higher than the increase observed in abiotic conditions.

Experimental Methods

Reactor Set-up

In order to cultivate biofilms on copper coupons (as-received), a CBR-90 Anaerobic Biofilm Reactor, CDC Reactor, (Figure 4.1) was set up in a fume hood. It consisted of up of eight rods that contained detachable coupons (square-shaped coupons, 10mm x 10mm x 2mm and rectangular-shaped coupons, 47mm x 15mm x 2mm) where the biofilm was generated. They were constantly subjected to shear stress and renewable nutrients in order to simulate the conditions seen in their natural environments or industrial systems.

In a biological safety cabinet (sterile conditions), copper coupons were placed into rods, previously immersed into a 70% ethanol solution, and exposed to UV radiation for three minutes on each side before being inserted into the reactor. Sterile N_2 (1 bar) was introduced to the reactor's gas atmosphere (0.2 m, Whatman®). After 10 minutes of deoxygenation with N_2 gas, sterile and deoxygenated LS4D (BAL, 60L:30S) medium was pumped into the reactor. The reactor was positioned on a hot plate within a water container maintained at 30°C and low agitation (50 rpm). These conditions sustained microbial activity throughout the duration of the experiment.



Figure 4. 1: CDC CBR-90 Anaerobic Reactor design consisting of a sealed lid with gas and media inlet and outlet tubings, thermocouple probes, and Pyrex bowls, mounted on hotplates. The inside of the reactor consists of rods that held coupons and a centrally positioned magnet to facilitate media agitation.

Inoculum of Oleidesulfovibrio alaskensis G20

After the temperature was adjusted, a 40 mL syringe connected to the sealed reactor lid was used to inoculate the reactor. In order to enable for surface colonization, the reactors were incubated in batch mode for approximately 16-18 hours, after which a peristaltic pump was used to maintain continuous flow (flow rate= 1 ml/min; D=0.15/h). Over the course of continuous growth (14 d), coupon samples were removed for pit depth, protein, carbohydrate analyses and high-resolution biofilm imaging.

Biofilm and Coupons Harvesting

The biofilm coupons were taken out from the reactor at 7, 9, and 14 d, and subsequently, the biofilm was rapidly removed from the coupon using a sterile scraper. The biomass was collected and suspended in 3 ml of chilled deionized water (dH_2O), followed by homogenization

by a process of freezing and thawing (Krantz, et al., 2019). Removal of the biofilm and of the mineral layer resulting from the exposures was performed by ultrasonic cleaning with hydrochloric acid (HCl) for 1 minute. Preliminary FE-SEM analyses were performed to confirm that this procedure would not introduce any additional corrosion damage which may later affect MIC evaluation.

Preparation of Samples for Imaging

High magnification and high-resolution images were visualized using FE-SEM with a ZEISS SUPRA 55VP microscope (Carl Zeiss Microimaging, GmbH, Gottingen) to describe biofilm morphology and the coupons after the biofilm removal. This instrument was equipped with energy dispersive x-ray analysis (EDX) capabilities. To preserve EPS and biofilm structures, biofilms were fixed using Karmovsky's fixative (3.2% w/v paraformaldehyde, 2.5% w/w glutaraldehyde, 0.05M sodium 187 cocodylate) for 16 h. The samples immersed in distilled water (dH_2O) for a duration of 5 minutes each, with the purpose of eliminating the fixative. The process of ethanol (EtOH) dehydration consisted of sequential immersions in different ethanol concentrations: 5 minutes in 25% EtOH, followed by 5 minutes in 50% EtOH, then 5 minutes in 75% EtOH, 15 minutes in 95% EtOH, and finally two rounds of 45-minute immersions in 100% EtOH. The dehydrated samples followed a drying process utilizing a Tousimis Samdri-795 Critical Point Dryer (Tousimis Research Corporation, Rockland MD). The dried samples underwent a 30-second coating process with Iridium using an Emitech K575X Sputter Coater, then samples were preserved in vacuumed tubes until used.

Growth Parameter Measurements

Carbohydrate composition of biofilm cells was measured by a cysteine-sulfuric acid calorimetric assay as previously described (Brileya, 2014). Protein contents of biofilm cultures were measured using the Qubit Protein Assay Kit (Life Technologies, Eugene, Oregon, USA) end of 7, 9, 14-day experiment [33]. Biofilm mass was measured using the weight change before and after experiments.

Results and Discussion

In the CDC reactors, a significant and resilient formation of biofilm was detected on copper (101) and glass coupons over a period. The first experimental trial operated 7, 9, and 14 days, while the second experiment lasted for only 7 days. The second experiment was conducted with a total of four reactors, three with copper coupons and one with glass coupons as control. Biofilm development was quantified using protein assay, carbohydrate (cysteine-sulfuric acid) technique, and scanning electron microscopy.

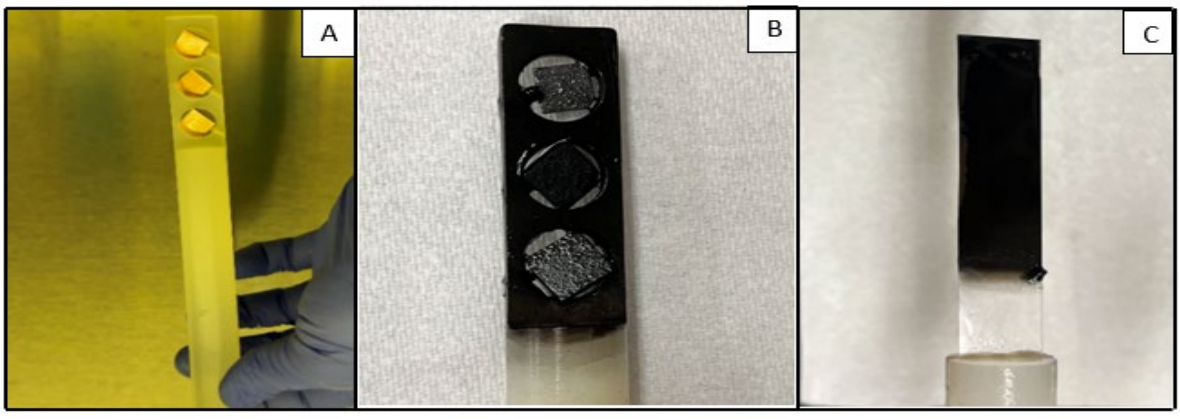


Figure 4. 2: Images of copper coupons that have initially undergone sterilization and then inserted into the coupon holder inside a laminar flow hood (A), followed by the exposure of these coupons to *O. alaskensis* G20 for a duration of 7 days (B), and the exposure of glass coupons to the bacterium for the same duration (C).

The biofilm mass to surface area ratio was determined by measuring a change in weight of the copper coupons before and after the experiment with *O. alaskensis* G20 biofilm. As seen in Figure 4.3., the growth of *O. alaskensis* G20 biofilms exhibits a progressive trend over time. The ratios of mass to surface area were found to be 6.38, 9.71, and 23.11 mg/cm^2 for days 7, 9, and 14, respectively. The biomass exhibited a significant growth of 52% and 262% on day 9 and day 14, respectively, in comparison to day 7.

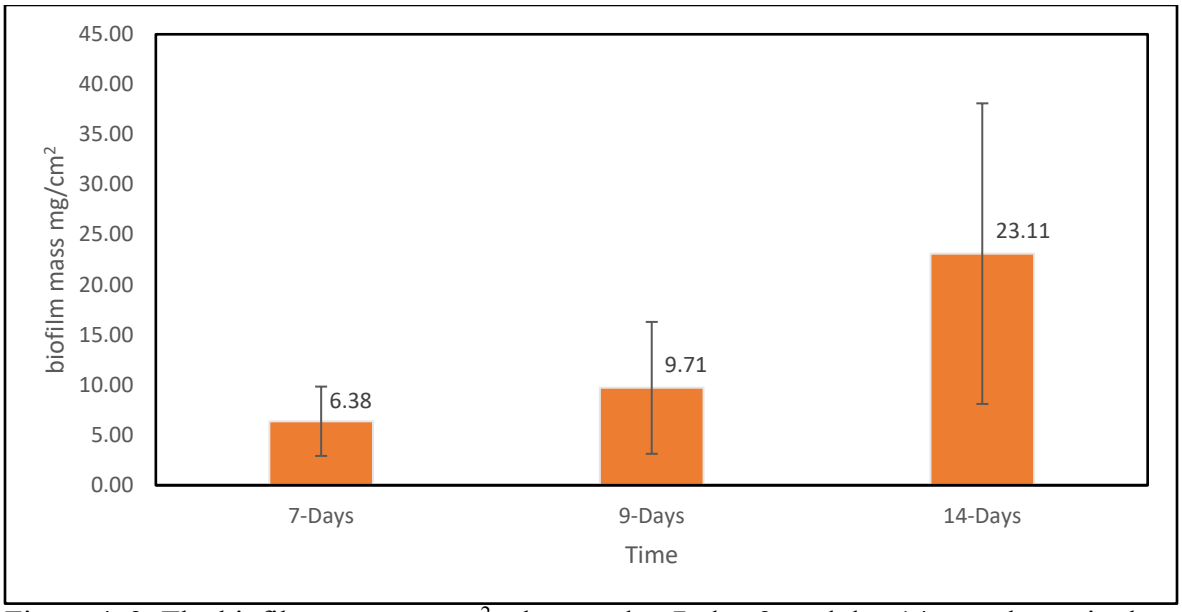


Figure 4. 3: The biofilm mass per cm^2 taken on day 7, day 9, and day 14 was shown in the columns, along with a 95% confidence range.

The protein/surface area (µg/ *cm*^{2}) (Figure 4.4) below represents the same trend as seen in (Figure 4.3). Three coupons, including two copper coupons and one glass coupon, were collected on day 7, day 9, and day 14 for the purpose of quantifying the protein content of *O. alaskensis* G20 biofilms. The average values for protein per unit surface on copper coupons area were 203.575 µg/cm^2, 282.14 µg/cm^2, and 379.29 µg/cm^2 for days 7, 9, and 14, respectively. The reported increases of 38% and 86% in protein measurements on day 9 and day 14, respectively,

compared to day 7, may be attributed to a continuous inflow of nutrients into the system and outflow of the planktonic cells. Protein content on glass coupons went up by roughly 32% and 102.5% for days 9 and 14, respectively, as compared to day 7. Similar growth was seen for hexose numbers on glass coupons, which increased 13.5% and 32% for days 9 and 14 when compared to day 7. At all time points, biofilms on copper surfaces had more protein and carbohydrate (6 to 7-fold) than glass coupons. It is interesting to note that protein levels increased (1.35x) between 9 and 14 days but the carbohydrate levels did not increase significantly on copper but continued to increase on glass. The carbohydrate to protein ratio was in the 0.9 to 1.2 µg/µg range for copper whereas the ratio was approximately 3 to 4 µg/µg for the glass coupons.

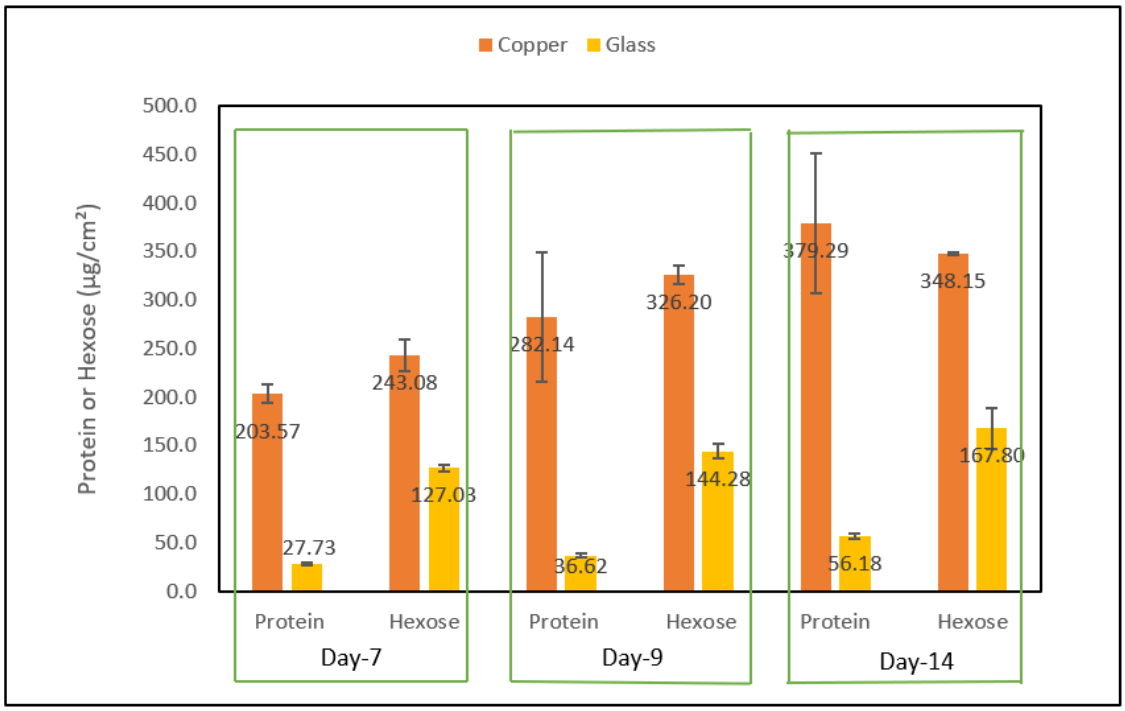


Figure 4. 4: Protein and hexose quantities of *O. alaskensis* G20 biofilms cultivated on copper and glass coupons (µg/cm^2) with 95% CI throughout a period of 7, 9, and 14 days inside CDC reactors.

The protein-to-surface area ratio of biofilms on glass is about 7 to 8 times lower compared to proteins found on copper coupons. The decrease in protein levels on glass surfaces may be attributed to the affinity of negatively charged G20 molecules towards positively charged copper metal surfaces, facilitating the formation of biofilms. In contrast, Krantz reported the protein and hexose quantities of G20 biofilms cultivated on 316 steel, 1018 steel, and glass coupons in LS4D EAL and EDL limited conditions inside CDC reactors. In the experimental conditions of EAL, the protein and hexose quantities seen on the glass coupon reached approximately 4 and 6 $\mu g/cm^2$ respectively for a period of 144 hours. Under identical experimental conditions, the quantities of protein and hexose on the surface of 316 steel were lower than glass. The protein content was around 2 $\mu g/cm^2$, while the hexose content was approximately 5 $\mu g/cm^2$. In contrast, when subjected to identical conditions, the quantities of protein and hexose on the surface of 1018 steel coupons were around 10 and 20 $\mu g/cm^2$, respectively (Krantz, et al., 2019). The outcomes of the EDL condition during a 144-hour were found to be similar to those of the EAL condition. Comparatively, the results suggest that biofilm development of G20 on copper is more aggressive in a BAL condition compared to 316, 1018 steel, and glass coupons under the EAL and EDL conditions.

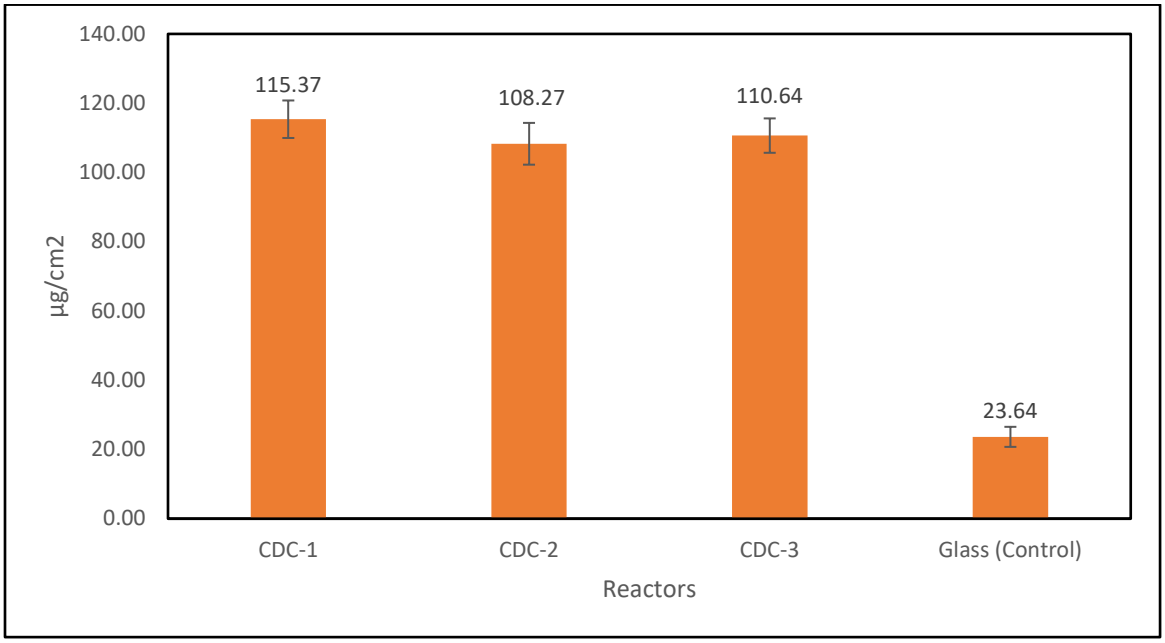


Figure 4. 5:. The protein-to-surface area ratio (µg/cm^2) was measured for three CDC reactors, as well as a control run (glass coupon) with % 95 confidence interval. For this experimental trial, identical inoculum and experimental settings were used, with four reactors being simultaneously operated. Note that the surface area of the copper was increased by a factor of two (56.4 cm^2) in comparison to the prior experiment in order to obtain more biomass for transcriptomic analysis.

Four CDC reactors were operated concurrently for a duration of 7 days, with three of them containing copper coupons and the other containing glass coupons. These reactors were subjected to identical growth conditions throughout the experiment. Three coupons were removed from the reactors, and then protein numbers were analyzed. The findings are shown in Figure 4.5, indicating that there were insignificant variations in protein levels observed among the reactors containing copper coupons. The average protein to surface area ratio was found to be 111.43 +/- 2.9 µg/cm^2. The protein quantities seen on glass coupons were about five times lower compared to the protein concentrations detected on copper coupons. A similar pattern was seen in the previous trial. For this experimental setting, hexose numbers weren't calculated due to my absence in the laboratory.

Corrosion Rate and Pit Depth Analysis

The corrosion rates for abiotic and biotic were calculated from the mass loss measurement, as per ASTM Standard G1-03, using equation 1 as previously described in chapter 3. Mass loss measurements were performed by weighing the coupons before exposure to bacteria and after cleaning with the Clark solution.

$$\text{Corrosion Rate}\left(\frac{\text{mm}}{\text{year}}\right) = \frac{8.76\times10^{4}\times\text{Mass loss(g)}}{\text{Area (cm}^2\text{)}\times\text{Time of exposure (hours)}\times\text{Density}\left(\frac{\text{g}}{\text{cm}^3}\right)} \quad \text{(Eq. 1)}$$

Table 4. 1: Copper coupon corrosion rates calculated after biotic and abiotic exposure to *O. alaskensis* G20 for 7 days in CDC reactors.

Factor	N	Corrosion rate (mm/year)	StDev	95% CI
Abiotic 7 days	3	0.025	0.0062	(0.0095, 0.0404)
Abiotic 9 days	3	0.028	0.0155	(-0.011, 0.067)
Abiotic 14 days	3	0.016	0.008	(-1.018, 1.676)
Biotic 7 days	2	0.016	0.0015	(0.002, 0.029)
Biotic 9 days	2	0.046	0.0088	(-0.034, 0.125)
Biotic 14 days	2	0.082	0.0309	(-0.195, 0.359)

*A significant outliner, 0.955mm/year, (0.01<P) was found in 14-day abiotic experiments and it was removed from statistical analysis

As seen in Table 4.1., in abiotic conditions, the average corrosion rate increased by 12% when compared to for day 9, as compared to day 7. The corrosion rate on day 14 demonstrated a significant outliner, 0.955mm/year, (0.01<P). When this number was removed from statistical analysis, the corrosion rate for abiotic day 14 dropped by 36% as compared to abiotic day 7. In

biotic experiments, the average corrosion rates dramatically increased by 187.5 and 412.5% for days 9 and 14 when compared to day 7.

The longer presence of coupons inside the reactors resulted in an increased occurrence of biocorrosion products on their surfaces. In addition, the removal of these products from the surface required a longer duration of cleaning time. It should be noted that a complete cleaning of the whole surfaces of the coupons was not achieved. It was observed that the coupon weight loss measurement is challenging in order to determine corrosion rates in trials, 9 and 14 days.

This may have been the reason that 7-day biotic corrosion rate was calculated 0.4074 +/- 0.058 mm/year under the static condition in previous chapter, 3. It is way higher than 7-day biotic corrosion rate, 0.025+/- 0.062 mm/year in reactors. Further experiments are required to understand if the presence of a passive layer of corrosion minerals on metals prevents the process of corrosion on the surface.

In their study, Wadood et al. performed an analysis of the electrochemical behavior of a copper alloy to investigate the impact of microbial presence on the corrosion kinetics of the metal. Their findings revealed that the presence of microbes on the surface of the copper alloy resulted in significant alterations to its corrosion kinetics. The difference in values between the biotic and abiotic experimental conditions is shown by Wadood in their graphical representation of the equivalent electric circuit and the fitting of the electrochemical impedance spectroscopy data model. The charge transfer resistance and biofilm/corrosion products film resistance exhibit greater values in systems including bacteria in comparison to those without bacterial presence (Wadood, et al., 2019). This phenomenon may be related to the development of a thick biofilm.

Wang et al. (2022) showed the presence of a biofilm blocks the transfer of charges from the surface of a copper alloy, resulting in an increased resistance to corrosive ions. This phenomenon causes a change in the corrosion potential towards a more noble direction, as shown by previous studies. The results of the Wang et al. study indicate that the presence of a bacterial biofilm on the surface of the alloy has the potential to enhance the corrosion resistance of Cu alloys (Wang, et al., 2022).

Corrosion pit depths on copper 101 surface were measured in CDC reactors and compared with static settings in order to investigate the interactions between bacteria and copper coupons both static and dynamic environments.

It is important to acknowledge that CDC reactors maintained a consistent supply of nitrogen. This can potentially decrease the concentration of hydrogen sulfide (H_2S) gas inside the reactors. Due to this factor, the pit depths have been reduced by only 20%.The measurement of pit depths in this study used the same methodology as that used in Chapter 3 for static environments. Pits were randomly selected on the coupon surfaces and a minimum of nine pits were evaluated for each surface finish. Multiple measurements (a minimum of three) were conducted on the same pit to minimize uncertainties introduced by the X-ray production statistics. The analysis revealed that the detected pittings on both surfaces under both dynamic and static settings, failed to show statistically significant differences ($p > 0.224$, Tukey's test). According to the data shown in the Table 4.2., the measurements for pit depth means were recorded as 4.33 µm and 5.23 µm for the static (7-day) and reactor (7-day) experiments, respectively.

Table 4. 2: Pit depth measurements performed on copper coupons with copper (101) after biotic exposure to *O. alaskensis* G20 for 7 days in static and reactor conditions.

Factor	N	Pit Depth Mean (µm)	StDev	95% CI
Static (7 days)	10	4.33	2.03	(2.77, 5.89)
Reactor (7 days)	9	5.23	1.15	(4.37, 6.09)

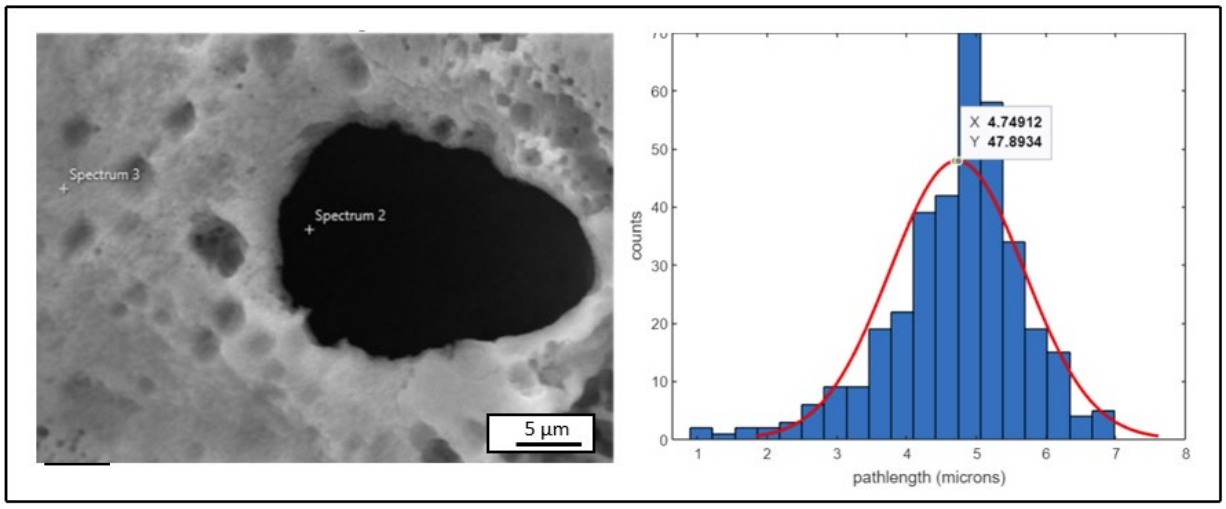


Figure 4. 6: The SEM image on the right shows the points at which EDX spectra were acquired in order to quantify the corrosion pit depths. The left image represents the outcome of MATLAB pit depth analyses. The integration of the EDX spectrums into MATLAB yielded a measurement of 4.7 microns of the pit.

Biofilm and Coupon Analysis Under FE-SEM

In order to analyze the morphology of biofilms, as well as the appearance of coupons in both biotic and abiotic reactors, high-resolution images were obtained using a ZEISS SUPRA 55VP microscope (Carl Zeiss Microimaging, GmbH, Gottingen). The coupons were examined after the removal of the biofilm in the biotic reactor, as well as after exposure to LS4D BAL medium for 7, 9, and 14 days in the abiotic reactors.

High-resolution images for biotic conditions (figures 4.7, 4.8, 4.9) showed mineral depositions on the surface. The minerals were deposited more intensely, as the reactor running time was increased.

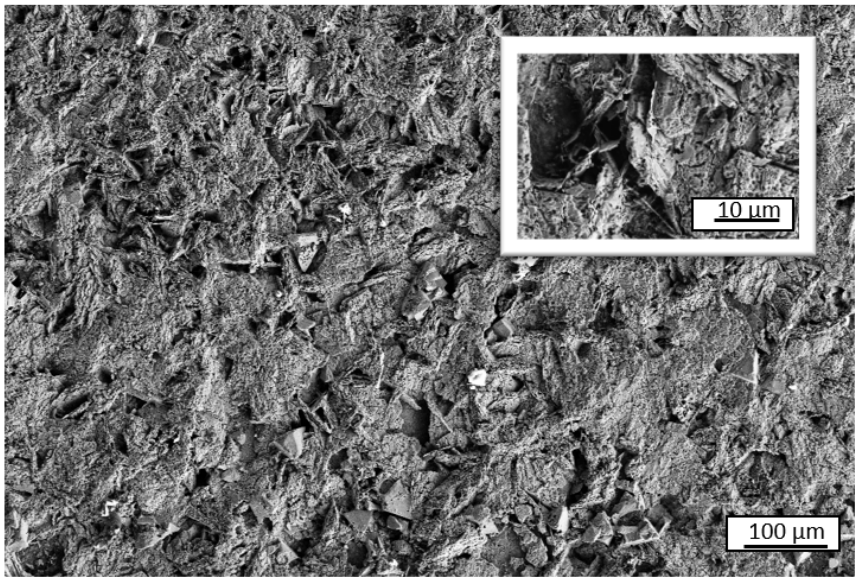


Figure 4.7: SEM image of a coupon that has undergone abiotic exposure in a reactor for a duration of 7 days.

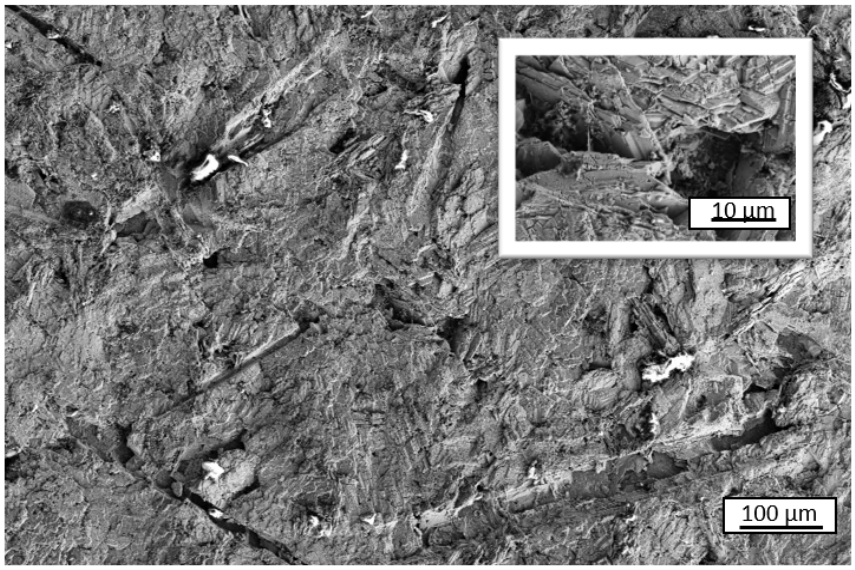


Figure 4. 8: SEM image of a coupon that has undergone abiotic exposure in a reactor for a duration of 9 days.

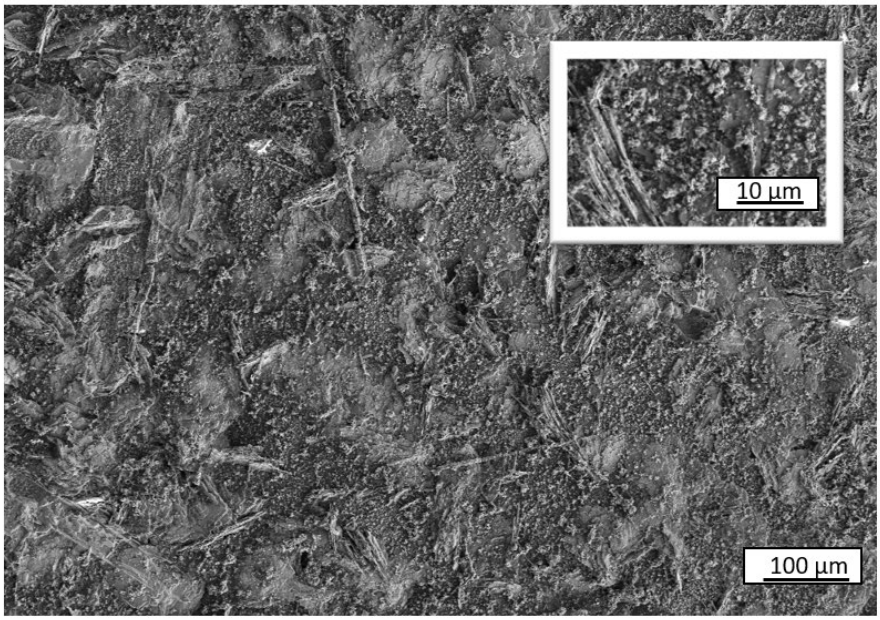


Figure 4. 9: SEM image of a coupon that has undergone abiotic exposure in a reactor for a duration of 14 days.

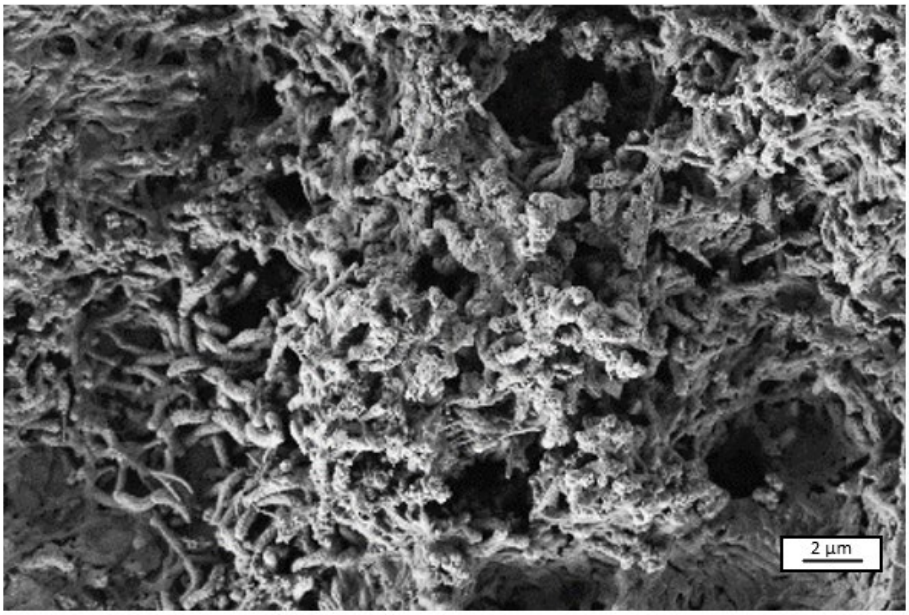


Figure 4. 10: SEM image of robust *O. alaskensis* G20 biofilm generated 7-day exposure in CDC reactor.

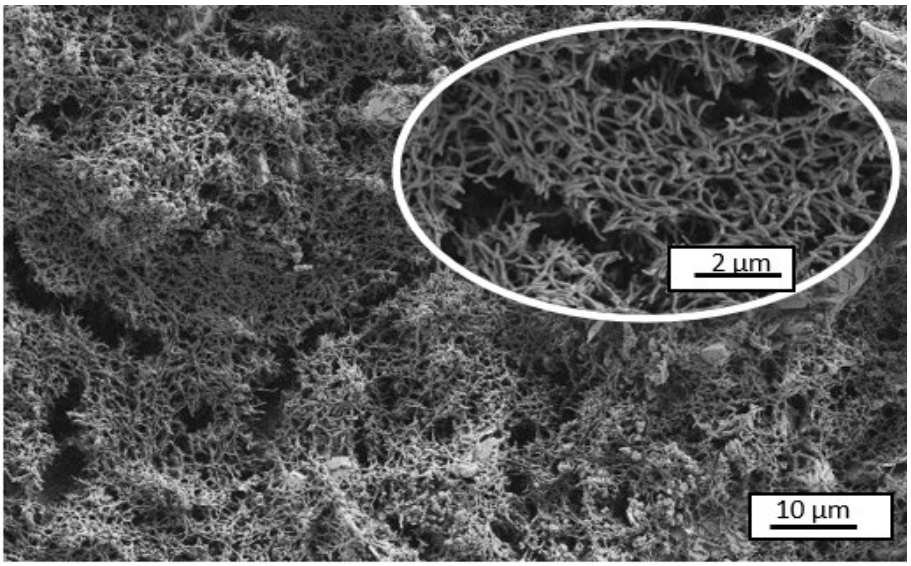


Figure 4. 11: Biofilm jungle inside CDC reactors. The image shows a SEM picture of the robust growth of *O. alaskensis* G20 biofilm on a coupon over a period of 7 days inside a CDC reactor, together with the corrosion products, Cu_2S, barely seen on the upper left and upper middle part of the picture.

The presence of corrosion precipitations in this image is hardly noticeable. The reason for this is because the surface was mostly occupied by *O. alaskensis* biofilm.

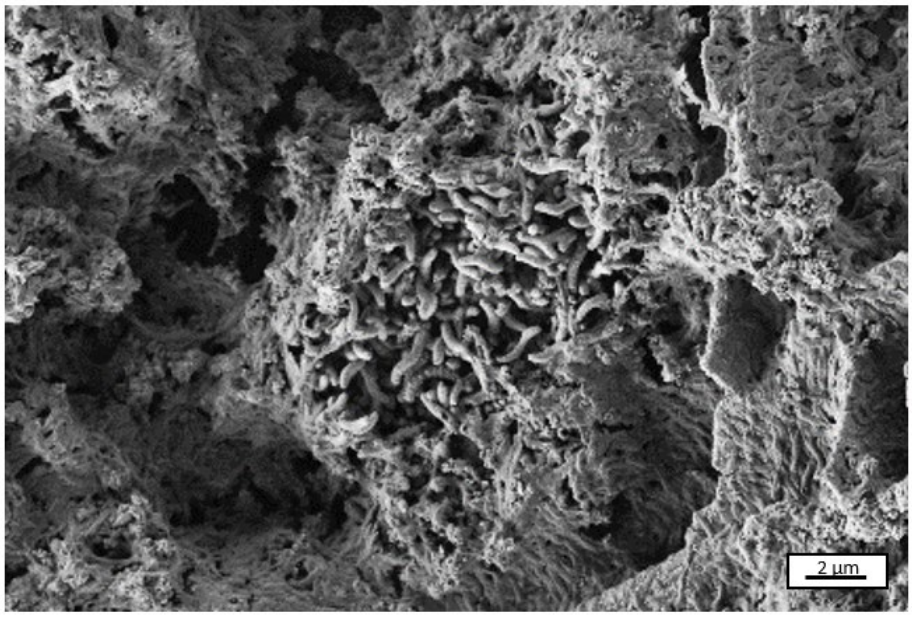


Figure 4. 12: SEM image of robust *O. alaskensis* G20 biofilm generated 9-day exposure in CDC reactor, together with the corrosion products, Cu_2S.

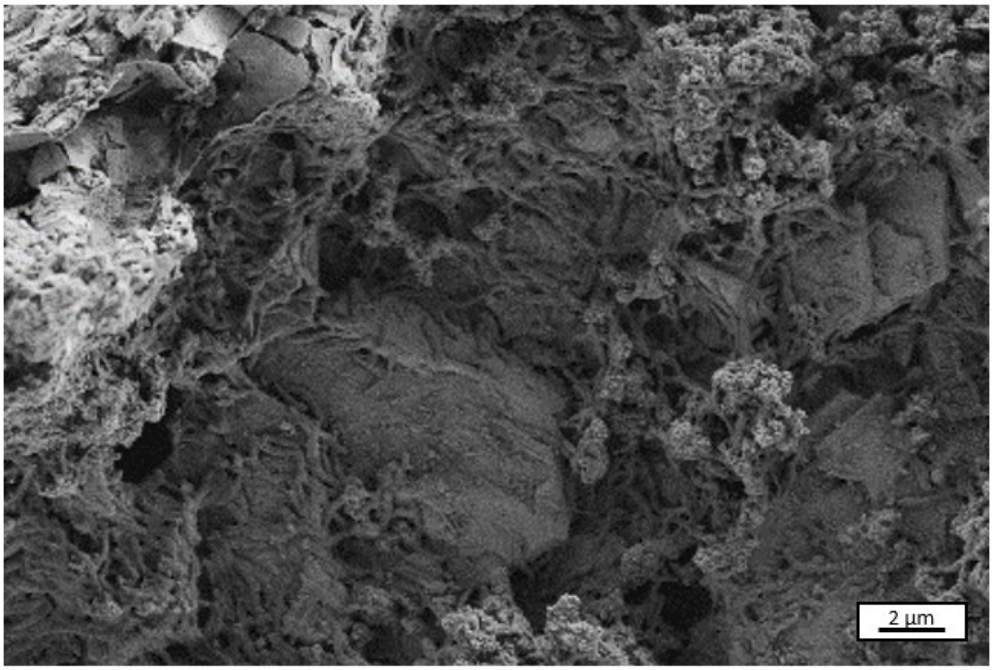


Figure 4. 13: SEM image of robust *O. alaskensis* G20 biofilm generated on deposited corrosion products, Cu_2S for 14-day exposure in CDC reactor.

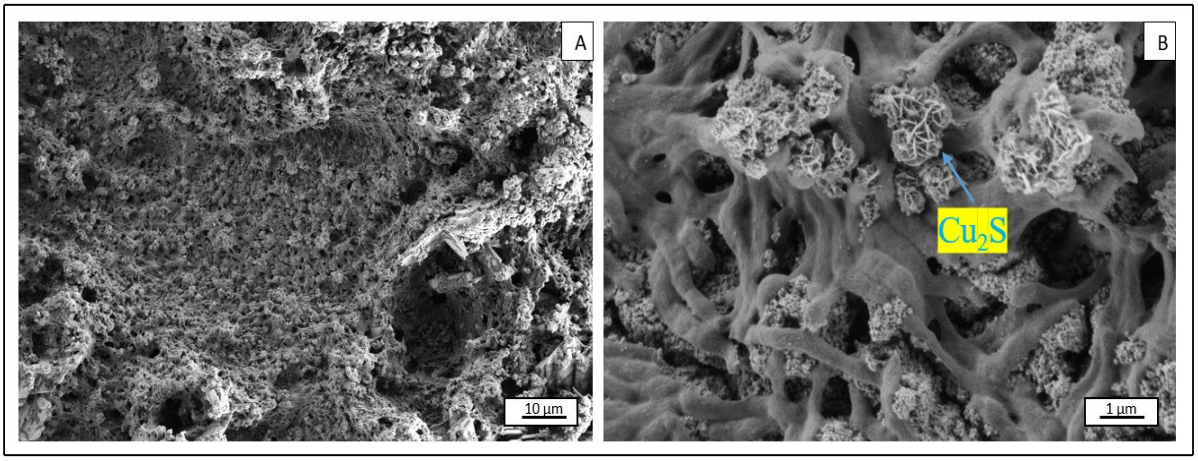


Figure 4. 14: SEM image (A) aggressive growth of *O. alaskensis* inside CDC reactor for 7 days, (B) a closer look of image A to robust *O. alaskensis* biofilm grown on copper and Cu_2S mineral as corrosion byproducts.

In the preceding chapter, Chapter 3, the X-ray diffraction technique was used to examine the crystalline nature of corrosion byproducts. Under static conditions, the XRD spectra revealed the presence of copper (I) sulfide (Cu_2S), often referred to as chalcocite. Two distinct crystal structures were identified, namely monoclinic (low chalcocite) and hexagonal (high chalcocite). Additionally, the identification of digenite Cu_xS with $x=1.79\text{-}1.84$ was observed. It may be inferred that a comparable crystalline structure is present in a continuous system, as shown by the similarity of SEM images obtained from both static and continuous settings.

Moreover, it was observed that the mineral layer exhibited a dense and impermeable structure on the surfaces of the copper (101) coupons under static conditions. I assume that this structure has similarities to the continuous system.

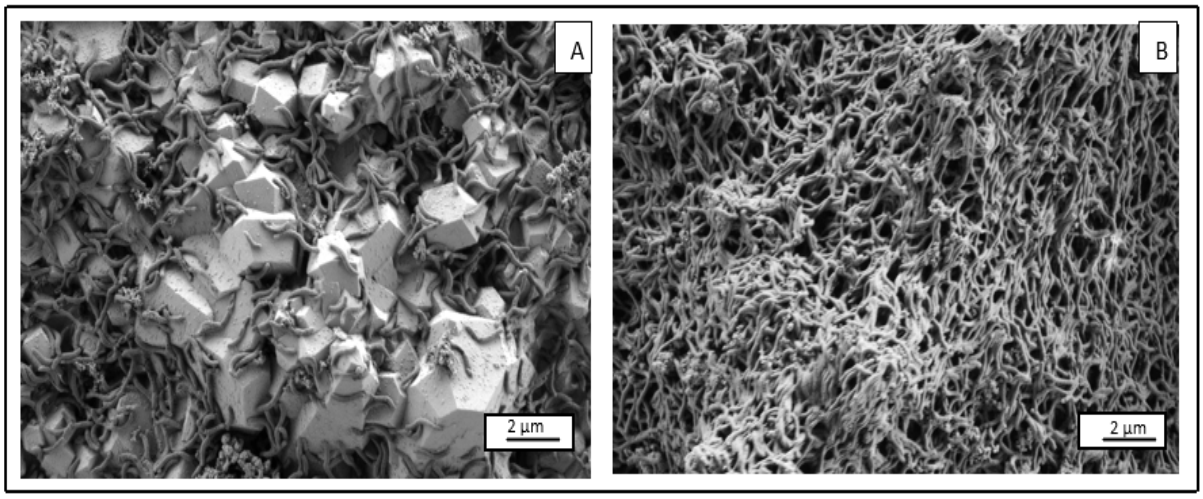


Figure 4. 15: Image (A) is G20 biofilms developed on deposited corrosion products a copper surface (101) under static condition, whereas the image (B) is the biofilm produced on an identical copper surface (101) in a CDC reactor for a duration of 7 days.

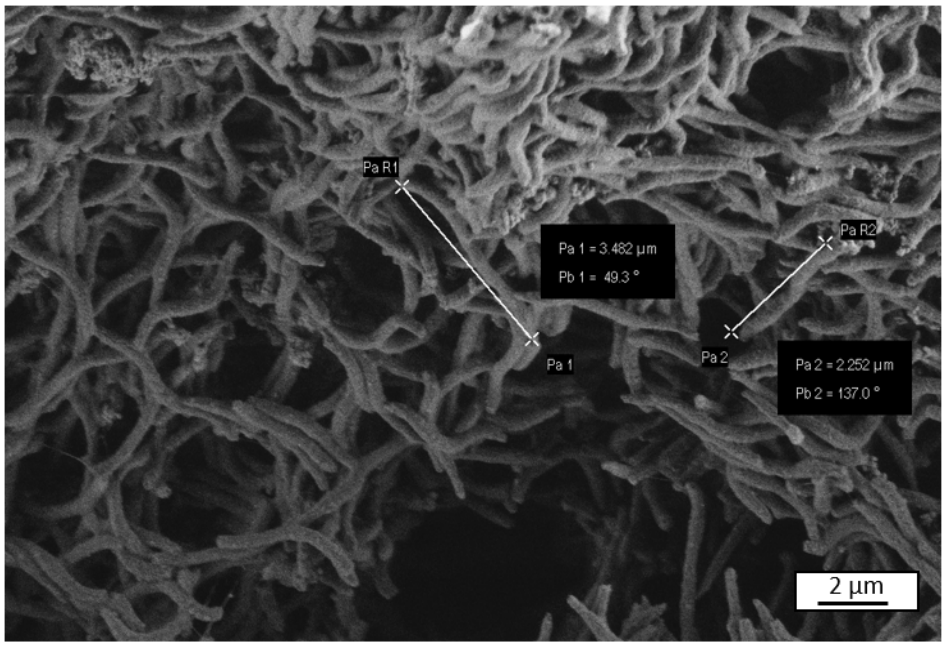


Figure 4. 16: Cells of *O. alaskensis* grown on a copper coupon for duration of 7 days inside CDC reactor.

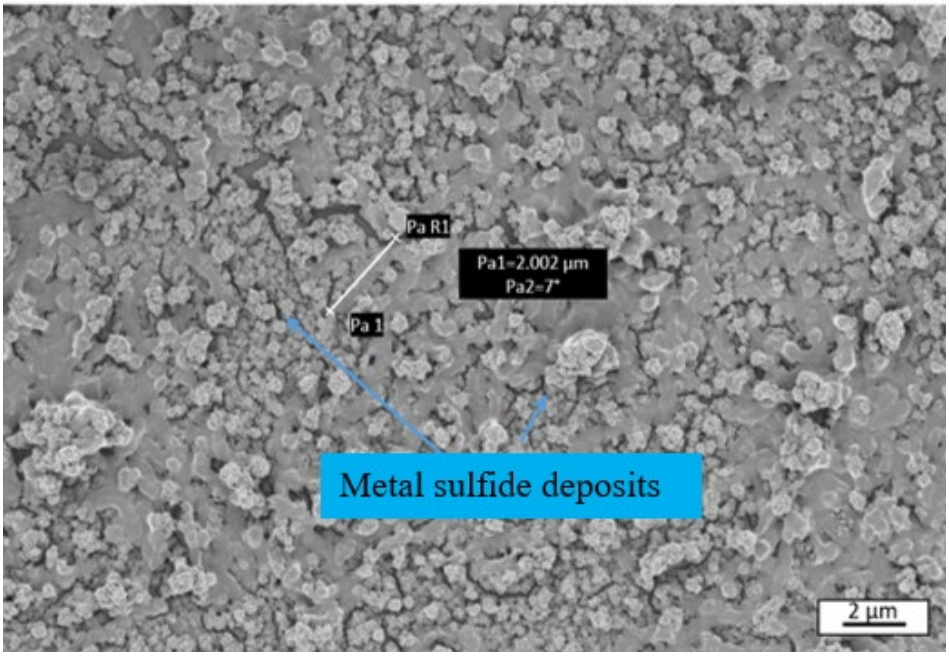


Figure 4. 17: Cells of *O. alaskensis* grown metal sulfide deposits on a glass coupon for a duration of 7 days inside a CDC reactor.

Cell lengths of *O. alaskensis* have been reported to range from 1.0 to 5.0 microns (Beech I. B., 1993). Based on SEM images in Figure 4.16 and 4.17, the bacterial cell length was shown to be within this range in the reactors. The lengths were around 2 microns on glass surfaces and 2.5 to 3.5 microns on copper surfaces. Compared to glass coupons, the cells on copper surfaces had longer lengths. Presumably, these phenotypic changes in G20 are the consequence of genotypic adaptations to copper stress.

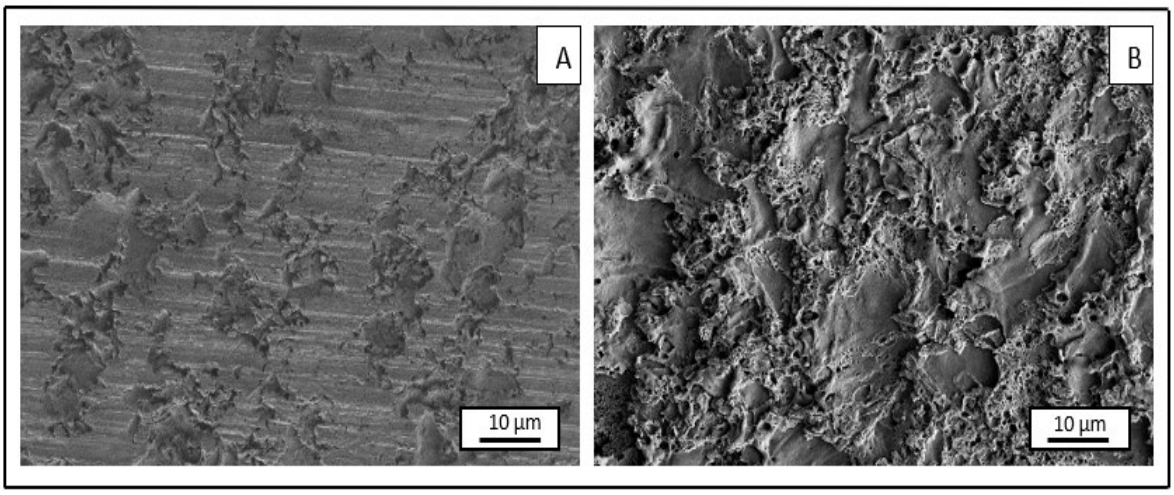


Figure 4. 18: SEM image (A) shows copper coupon surface before the bacterial exposure, image (B) shows the copper surface7-day bacterial exposure in the reactor and cleaned then sonicated it, soaked in 37% HCL.

Figure 4.18B above shows the corrosion of the copper surface towards the left. The noticed unidirectional corrosion morphology may perhaps be attributed to the rotational direction of the stirrer used inside the reactor.

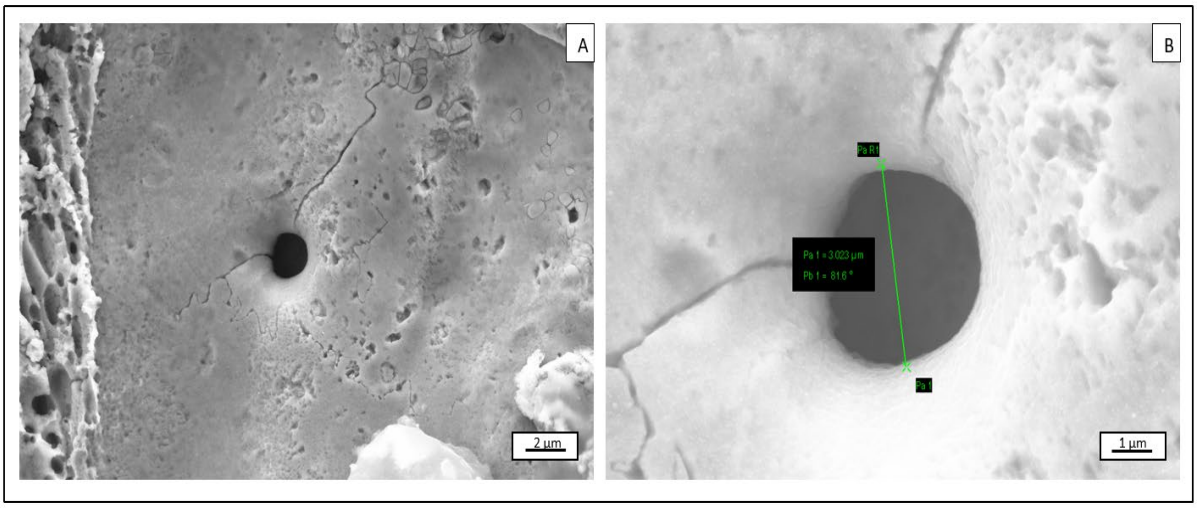


Figure 4. 19: SEM image (A) shows a localized pitting on the grain boundary at the end of 7 days exposure, (B) shows the diameter (3.023 µm) of the pit on the left image.

In their study, Sungur and Cotuk captured SEM images of galvanized steel test coupons acquired from a recirculating water system over a period of 10 months. Their findings revealed the presence of corrosion pits, characterized by diameters ranging from 15 to 16 micrometers (Ilhan-Sungur & Cotuk, 2009). The measured pitting diameter on a 10-month-old sample in recirculating water systems is larger (15-16 um) compared to the diameter (3 um) seen on a 7-day-old copper coupon in a CDC reactor as shown figure 4.19. It may be said that the presence of *O. alaskensis* G20 on copper (101) surfaces leads to a more accelerated corrosion process than the process on galvanized steel, even within a relatively little timeframe of 7 days.

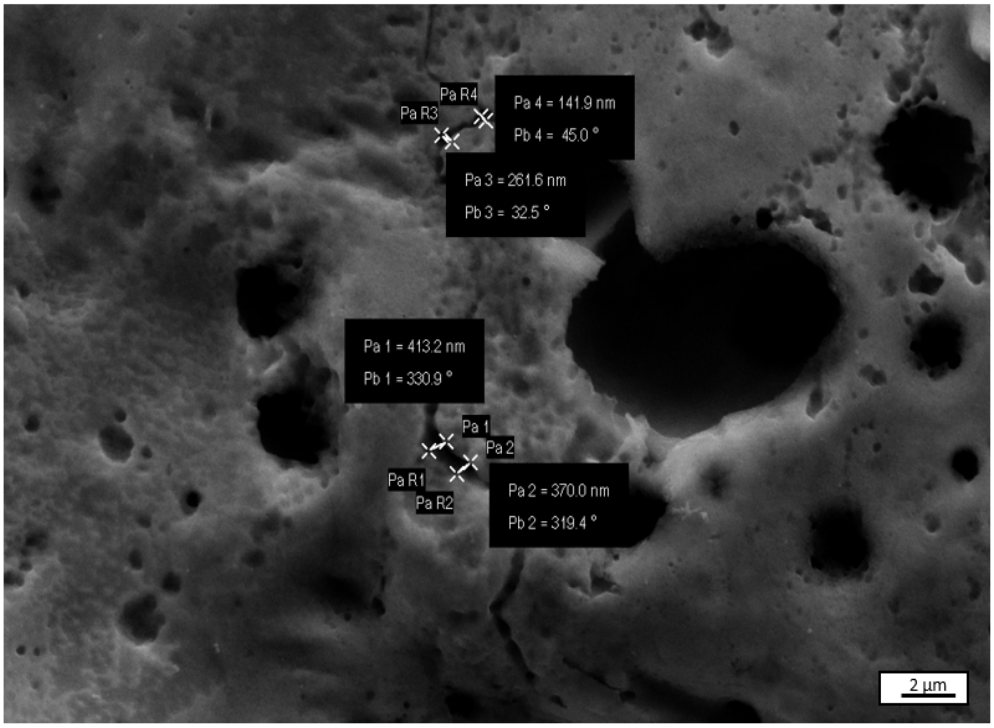


Figure 4. 20: SEM image of the wideness of intergranular corrosion measurements along with a crack on a copper coupon after 7-day exposure inside a CDC.

SEM images reveal the presence of intergranular corrosion fractures with widths ranging from 140 to 413 nm on copper surfaces in biotic and dynamic environments. As seen in figure

4.20, the occurrence of intergranular corrosion on copper surfaces may have accelerated by the existence of resilient biofilms of *O. alaskensis* G20 Biofilms have the ability to produce a conducive environment for corrosion by generating corrosive substances and establishing localized anaerobic conditions. The relationship between biofilms of *O. alaskensis* G20 and copper surfaces is intricate and includes multiple variables, including substrate concentrations, metal properties, grain size, grain boundary orientations and specific conditions of the system, such as whether it is static or dynamic, high or low temperature.

SRB attachment to metal surfaces is more likely to occur at grain boundaries, which are crystalline defects that separate grains with various orientations (Shifler, 2022). Because of the increased crystal defects, greater impurity levels, and bigger grain boundary energy, these random grain boundaries are electrically active (Nakajima, 2019). The bacteria may attract with this electrical active part and may subsequently accelerate localized corrosion. Another study, Trelewicz and Schuh, investigated the stability of binary nanocrystalline alloys and grain boundary segregation. They investigated how alloying changes the Gibbs free energy in polycrystals and created a free energy function. The article claims that elemental nanocrystalline metals like Ni, Cu, Al, and Pd, which show the development of grains at very low homologous temperatures, are the ones where the issue of nanostructure stability is most noticeable. These substances exist in a condition that is far from equilibrium, which is demonstrated within the framework of Gibbs' formalized thermodynamics. $dG = \gamma dA$, where γ is the grain boundary energy and G is the change in the Gibbs free energy with respect to the grain boundary area (A). According to this equation, the grain boundary energy (γ) and the change in the system's Gibbs free energy (dG) as a result of a change in the grain boundary area (dA) are proportional

(Trelewicz & Schuh, 2009). They clarified a basic idea in material thermodynamics, especially as it relates to grain boundaries in polycrystalline materials. The Gibbs free energy of the system will vary according to the energy associated with the grain boundaries if you change the area of the boundaries (for instance, by creating more or finer grains). If the grain boundary energy (γ) is positive, which is often the case, an increase in grain boundaries (dA is positive) results in an increase in the system's Gibbs free energy (dG is positive). This increase in free energy results from the system being less stable as a result of the energy required to expand or create new grain boundaries. To avoid bacterial adherents on grain boundaries, we will need lower grain boundary energy by reducing the grain boundary area on copper. Because a drop in the Gibbs free energy (dG is negative) would result from a reduction in the grain boundary area (dA is negative), suggesting a shift towards a more stable state and this could reduce the bacterial adhesion on copper surface.

Conclusion

This study conclusively demonstrates that the presence of *Oleidesulfovibrio alaskensis* G20 biofilms significantly accelerates the corrosion process on copper (101) polycrystalline surfaces, particularly in sulfate-rich flow-through systems where SRB are active. The experimental results reveal a robust and progressive increase in biofilm mass and protein content on copper over time, with notable increases in both days 9 and 14, indicating a heightened potential for biocorrosion. Corrosion rate analyses further confirm this trend, showing a dramatic rise in corrosion rates under biotic conditions as compared to abiotic scenarios. Notably, the presence of microbial biofilms influences the electrochemical behavior of copper and its alloys, potentially enhancing their corrosion resistance. Additionally, the study underscores intergranular

corrosion on copper surfaces, exacerbated by biofilm formation, particularly at grain boundaries with increased electrical activity due to crystalline defects. This research underscores the significance of managing biofilm formation and grain boundary characteristics in copper to mitigate corrosion risks in both industry and nature. This work demonstrates the ability to grow G20 biofilms on copper coupons (10mm x 10mm x 2mm, 47mm x 15mm x 2mm), as these size dimensions are important to couple growth dynamics and material characterization.

CHAPTER FIVE

CONCLUSION

Project Outcomes

Copper Toxicity on Oleidesulfovibrio alaskensis G20

This study initially aimed to quantitatively analyze the kinetic impact of Cu(II) toxicity on *Oleidesulfovibrio alaskensis* G20 in various growth mediums, LS4D BAL, EAL, EDL. The research successfully integrated the detrimental effects of Cu(II) into the kinetics of copper through mathematical expressions, offering a deeper understanding of its influence on bacterial growth. The results indicated a concentration-dependent toxicity of Cu(II), with increased copper concentrations leading to inhibited growth rates, diminished cell densities, and prolonged lag periods. Notably, the study revealed that in the EAL condition, cell densities increased at lower Cu(II) concentrations (6 and 12 μM), while higher concentrations (16 and 24 μM) drastically reduced cell densities and increased doubling times for all conditions. It can be said that *O. alaskensis* can tolerate copper toxicity better under limited substrate conditions, indicating a potential adaptive response to copper stress. In this study, the I_{50} values (concentration of Cu(II) causing 50% inhibition of bacterial growth) were also calculated for three mediums. The calculated I_{50} values 13.1, 13.87, and 11.31 μM for LS4D BAL, EAL, and EDL mediums, respectively. The study also measured the inhibition constants (K_i) for noncompetitive inhibitors under different growth conditions and the results were equivalent to I_{50} values since the inhibition constant is independent of substrate concentrations for noncompetitive inhibitors. When compared with previous *O. alaskensis* G20 may have a different tolerance level to copper

toxicity in LS4D BAL, EDL, EAL mediums compared to other SRB documented in earlier research in different mediums and environments. Previous studies commonly use undefined growth conditions (e.g,. yeast extract) that can greatly impact cellular responses to stresses, including heavy metals like copper. In addition, most previous studies attempt to estimate overall kinetic values without removing sulfides that are associated with SRB growth. The presence of the sulfides greatly impacts the initial cellular responses to heavy metals; therefore, the presented results represent initial cellular responses to copper in the absence of sulfides. These conditions can be viewed to simulate environmental conditions in which SRB growth has been minimal and/or the colonization of new niche space by SRBs.

Effect of Surface Finishing on Microbiologically Influenced Corrosion of Copper 101

In this study, the effects of varying surface roughness, achieved through metallographic grinding (400, 600, and 800 US grit) and polishing (3 µm diamond suspension), on the Microbiologically Influenced Corrosion (MIC) of copper 101 by *O. alaskensis* G20 were evaluated in collaboration with a PhD graduate student in the Material Science program. The study compared these finishes to as-received coupons over a one-week batch exposure. A significant change in corrosion rate was noted when surface roughness was altered from approximately 13 µm (as-received coupons) to about 0.06 µm (3 µm diamond suspension polished coupons). The corrosion rates were decreased when the coupon surface roughness was reduced. Notably, intergranular corrosion was observed in samples polished with diamond suspension. The similar trend fallowed for pit depth analysis. There was a statistically relevant decrease in pit depth across all finishes compared to the as-received samples, although no specific trend was discernable among the different surface finishes. Changes in surface

roughness affected the growth kinetics of the Cu_2S layer and its morphology, as well as pitting morphology. As-received, 400 US grit, and 3 μm diamond suspension polished coupons exhibited a dense Cu_2S layer indicative of rapid parabolic growth kinetics. In contrast, 600 and 800 US grit finished coupons showed a porous Cu_2S layer, suggesting slower linear growth kinetics. The 600 and 800 US grit finishes also developed a thin, compact, non-porous layer, varying in position based on the grit size. This layer's formation was associated with the chemical species in the pores of the adjacent layer and their diffusional flux. The developed mineral layer was identified as Cu_2S (chalcocite) in all coupons, with two different crystal structures detected: monoclinic (low chalcocite) and hexagonal (high chalcocite). The transition from low to high chalcocite, involving the oxidative dissolution of low chalcocite, was evidenced by the detection of digenite as an intermediate product.

Response of *Oleidesulfovibrio alaskensis* Biofilms Grown on Copper (101) in CDC Reactors

This study investigates the effects of *Oleidesulfovibrio alaskensis* G20 biofilms on the biocorrosion of copper (101) in dynamic (CDC reactor) environments. A significant and resilient formation of biofilm was observed on copper and glass coupons over periods of 7, 9, and 14 days. The biofilm development was quantified using protein assays, carbohydrate techniques, and visualized using SEM. The protein content on copper coupons increased significantly over time, with an 86% increase by day 14 compared to day 7. Hexose numbers also followed a similar trend. In contrast, biofilms on glass showed lower protein and hexose quantities, suggesting an affinity of the bacterial molecules towards copper surfaces. The study also investigated corrosion rates and pit depths in CDC reactors. Corrosion rates calculated from mass loss measurements indicated a dramatic increase in biotic conditions, particularly over longer

exposure periods. The biotic corrosion rates increased by 187.5% and 412.5% on days 9 and 14, respectively, compared to day 7. Pit depth measurements on copper surfaces under biotic conditions in CDC reactors were about 20% deeper than those under static conditions, indicating a more active corrosion process in dynamic environments. High-resolution SEM images showed robust biofilm growth and the presence of corrosion products such as Cu_2S. SEM images also showed unidirectional corrosion morphology on copper surfaces, possibly influenced by the rotational direction of the stirrer used in the CDC reactor.

This research provides valuable insights into the interaction between bacterial biofilms and metal surfaces, highlighting the impact of biofilm formation on corrosion rates and pit depths in dynamic environmental condition. The findings are crucial for understanding biocorrosion mechanisms and developing strategies to mitigate MIC in industrial and marine environments.

Funding Acknowledgements

This work was financially supported by the United States National Science Foundation (award #1920954) and the Center for Biofilm Engineering.

CHAPTER SIX

FUTURE WORK

Based on the findings and implications of the current research on the impact of *Oleidesulfovibrio alaskensis* G20 biofilms on the corrosion of copper, several directions for future experiments can be considered:

Extended Duration Studies

Conducting experiments over longer periods to observe the long-term effects of biofilm formation on copper corrosion inside CDC reactors and Balch tubes in steady condition. Longer experiment periods could help better understand how the chalcocite layer's growth kinetics and morphology develop over time. The chalcocite forms can be compared in CDC and Balch tubes. Measuring pit depths and corrosion rates could potentially provide a more comprehensive understanding of the progressive nature of MIC since MIC occurs in longer times. Furthermore, extended experiments would be helpful to observe biofilm development over time.

Variation in Environmental Conditions

This could also reveal how varying conditions affect biofilm characteristics and corrosion mechanisms. Investigating the impact of different substrate concentrations, basically using EAL and EDL mediums in CDC reactors and biofilm quantification, corrosion rate and pit depth analysis could help understand better sulfate reduction in the dynamic environments. Experiments could be conducted at the different temperatures and pH levels. Because some

research reported that corrosion at the various temperatures and pH levels showed different corrosion behavior for different SRB groups.

Different Bacterial Strains and Communities

Exploring the effects of other bacterial strains or mixed microbial communities on copper corrosion in CDC reactors. This would help in understanding the role of microbial diversity in MIC and the potential synergistic interactions among different species.

Cu^{+2} as Corrosion Inhibitor or Nano Glass Coating

Testing the efficacy of Cu^{+2} ions as biocorrosion inhibitor in preventing or minimizing biofilm-induced corrosion. The reactor study revealed a significant decrease in bacterial adhesion on glass surfaces in comparison to exposed copper surfaces. This observation has inspired the concept of using nano glass coatings to significantly reduce microbial adhesion and corrosion. Nano glass coated copper coupons could be potentially tested in the CDC reactors and in Balch tubes for steady conditions. These two potential corrosions preventing methods could lead to the development of more effective and practical strategies for combating MIC in industrial applications.

Genomic and Transcriptomic Analysis

Performing genomic and transcriptomic studies to understand the molecular mechanisms behind the biofilm formation of *O. alaskensis* G20 and its interaction with copper surfaces. This approach could identify specific genes and pathways involved in MIC. Three reactors including six rectangular shape of copper coupons (47mm x 15mm x 2mm) were already conducted for

transcriptomics analysis. The biofilm samples were removed at the end of 7 days and preserved in -80 for RNA-Seq in Fields Lab. However, due to my absence in the laboratory, the experiment hasn't been finished.

Electrochemical Characterization

Conducting in-depth electrochemical analyses to quantify the impact of biofilms on the electrochemical properties of copper. Techniques like electrochemical impedance spectroscopy (EIS) and potentiodynamic polarization could provide insights into the electrochemical processes driving corrosion in CDC reactors with *O. alaskensis* G20.

Advanced Imaging Techniques

Utilizing advanced microscopy and imaging techniques, such as atomic force microscopy (AFM) and confocal laser scanning microscopy (CLSM), to gain more detailed insights into the biofilm structure and its interaction with metal surfaces. Biofilm thickness can be measured over time inside CDC reactors. Testing copper and other metals with different surface properties pre- and post-growth with nanoAuger capabilities to better understand elemental nano-scale property effects on biofilm growth and corrosion in CDC reactors.

Real-world Application Studies

Testing the findings in real-world settings, such as in plumbing systems, marine environments, or industrial equipment where copper is commonly used. This would help in assessing the practical implications of the research. A comparable study may be conducted in CDC reactors and real-world conditions to mimic industrial applications and provide

more practical solutions, similar to the research conducted in Chapter 3 on static circumstances with different surface roughness levels (400, 600, 800 US grit, and 3 μm diamond suspension). These future experiments and works would not only enhance the understanding of MIC caused by *Oleidesulfovibrio alaskensis* G20 but also contribute to the broader field of corrosion science and biofilm research.

REFERENCES CITED

Abosrra, L., Ashour, A. F., Mitchell, S. C., & Youseffi, M. (2009). Corrosion of mild steel and 316L austenitic stainless steel with different surface roughness in sodium chloride saline solutions. *Simulation of Electrochemical Processes III*. https://doi.org/10.2495/ecor090161

Akonko, Saheed, Li, Y., D., Ziomek-Moroz, & M. (2005). Effects of cathodic protection on corrosive wear of 304 stainless steel. *Springer Link*, 405-410.

Alvarez, R. B., Martin, H. J., Horstemeyer, M. F., Chandler, Mei. Q., Williams, N., Wang, P. T., & Ruiz, A. (2010). Corrosion relationships as a function of time and surface roughness on a structural AE44 magnesium alloy. *Corrosion Science*, *52*(5), 1635–1648. https://doi.org/10.1016/j.corsci.2010.01.018

Ameh, S., E., Ikpeseni, C., S., Lawal, & S., L. (2017). A Review of Field Corrosion Control and Monitoring Techniques of the Upstream Oil and Gas Pipelines. *African Journals Online*.

Amendola, R., & Acharjee, A. (2022). Microbiologically Influenced Corrosion of Copper and Its Alloys in Anaerobic Aqueous Environments: A Review. *Frontiers*, Volume 13.

Angell, P., & Chamberlain, A. H. L. (1991). The role of extracellular products in copper colonisation. *International Biodeterioration*, *27*(2), 135–143. https://doi.org/10.1016/0265-3036(91)90005-c

Arghavanian, R., & Ahmadi, N. P. (2013). Electrodeposition of Ni–ZrO2 composite coatings and evaluation of particle distribution and corrosion resistance. *Surface Enginerring*, 649-654.

ASTM G1-03. (2017). Standard Practice for Preparing, Cleaning, and Evaluating Corrosion Test Specimens. *B. Stand*, *3*(2). https://doi.org/https://doi.org/10.1520/G0001-03R17E01

Avci, R., Davis, B. H., Wolfenden, M. L., Kellerman, L. R., Lucas, K., Martin, J., & Deliorman, M. (2015). A practical method for determining pit depths using X-ray attenuation in EDX spectra. *Corrosion Science*, 9-18.

Babich, H., & Stotzky, G. (1985). Heavy Metal Toxicity to Microbe-Mediated Ecologic Processes: A Review and Potential Application to Regulatory Policies. *Environmental Research* , 111-137.

Bard, A. J., Parsons, R., & Jordan, J. (2017). *Standard Potentials in Aqueous Solution*. https://doi.org/10.1201/9780203738764

Bard, P. a. (1986). The seismic response of two-dimensional sedimentary deposits with large vertical velocity gradients. *Bulletin of the Seismological Society of America,, 76(2)*, pp.343-366.

Barton, L. L., & Fauque, G. D. (2009). Biochemistry, physiology and biotechnology of sulfate-reducing bacteria. *Advances in Applied Microbiology*, 41-98.

Beech, B., I., Sunner, A., J., Hiraoka, & Kenzo. (2005). Microbe-surface interactions in biofouling and biocorrosion processes. *International Microbiology*.

Beech, I. B. (1993). *Oleidesulfovibrio alaskensis AL1 is an anaerobe, mesophilic, Gram-negative bacterium that was isolated from gravel material from soured oil reservoir.* Retrieved from BacDive: https://bacdive.dsmz.de/strain/4150

Beech, I. B., & Gaylarde, C. C. (1999). Recent advances in the study of biocorrosion: An overview. *Revista de Microbiologia*, *30*(3), 117–190. https://doi.org/10.1590/s0001-37141999000300001

Beech, I. B., & Sunner, J. (2004). Biocorrosion: towards understanding interactions between biofilms and metals. *Current Opinion in Biotechnology*, 181-186.

Bloch, K., Pardesi, K., Satriano, C., & Ghosh, S. (2021). Bacteriogenic Platinum Nanoparticles for Application in Nanomedicine. *Frontiers*.

Brandt, R. B., Laux, E. J., & Yates, S. W. (1987). Calculation of inhibitor Ki and inhibitor type from the concentration of inhibitor for 50% inhibition for Michaelis-Menten enzymes. *Biochemical Medicine and Metabolic Biology*, 344-349.

Brauer, J. I., Celikkol-Aydin, S., Sunner, J. A., Gaylarde, C. C., & Beech, I. B. (2017). Metabolomic imaging of a quaternary ammonium salt within a marine bacterial biofilm on Carbon Steel. *International Biodeterioration & Biodegradation*, *125*, 33–36. https://doi.org/10.1016/j.ibiod.2017.08.007

Brileya, K. A. (2014). Biofilm growth mode promotes maximum carrying capacity and community stability during product inhibition syntrophy. *frontiers in Microbiology, 5*, 693.

Büchler, M., & Schöneich, H.-G. (2009). Investigation of Alternating Current Corrosion of Cathodically Protected Pipelines: Development of a Detection Method, Mitigation Measures, and a Model for the Mechanism. *CORROSION The Journal of Science & Engineering*, 578-586.

Burstein, G. T., & Pistorius, P. C. (1995). Surface roughness and the metastable pitting of stainless steel in Chloride Solutions. *CORROSION*, *51*(5), 380–385. https://doi.org/10.5006/1.3293603

Canfiel, E, Don, Rosing, T, M., Bjerrum, & Christian. (2006). Early anaerobic metabolisms. *Philos Trans R Soc Lond B Biol Sci*, 1819-1336.

Canfield, D. E., & Teske, A. (1996). Late Proterozoic rise in atmospheric oxygen concentration inferred from phylogenetic and sulphur-isotope studies . *Nature*, 127–132.

Chaplin, M. F. (1986). Carbohydrate analysis - M. F. chaplin, J. F. Kennedy - Oxford ... https://global-oup-com.libproxy.ucl.ac.uk/academic/product/carbohydrate-analysis-9780199634491

Chen, J., Qin, Z., & Shoesmith, D. W. (2010). Kinetics of corrosion film growth on copper in neutral chloride solutions containing small concentrations of sulfide. *Journal of The Electrochemical Society*, *157*(10). https://doi.org/10.1149/1.3478570

Chen, J., Qin, Z., & Shoesmith, D. W. (2011). Long-term corrosion of copper in a dilute anaerobic sulfide solution. *Electrochimica Acta*, *56*(23), 7854–7861. https://doi.org/10.1016/j.electacta.2011.04.086

Chen, J., Qin, Z., & Shoesmith, D. W. (2014). Key parameters determining structure and properties of sulphide films formed on Copper Corroding in anoxic sulphide solutions. *Corrosion Engineering, Science and Technology*, *49*(6), 415–419. https://doi.org/10.1179/1743278214y.0000000188

Chen, J., Qin, Z., Martino, T., & Shoesmith, D. W. (2017). Non-uniform film growth and micro/macro-galvanic corrosion of copper in aqueous sulphide solutions containing chloride. *Corrosion Science*, *114*, 72–78. https://doi.org/10.1016/j.corsci.2016.10.024

Chen, J., Qin, Z., Wu, L., Noël, J. J., & Shoesmith, D. W. (2014). The influence of sulphide transport on the growth and properties of copper sulphide films on copper. *Corrosion Science*, *87*, 233–238. https://doi.org/10.1016/j.corsci.2014.06.027

Chen, S., Wang, P., & Zhang, D. (2014). Corrosion behavior of copper under biofilm of sulfate-reducing bacteria. *Corrosion Science*, *87*, 407–415. https://doi.org/10.1016/j.corsci.2014.07.001

Cheng, Y.-C., & Prusoff, W. H. (1973). *Biochemical Pharmacology*, 3099-3108.

Cheng, Y.-C., & Prusoff, W. H. (1973). "Relationship between the inhibition constant (KI) and the concentration of inhibitor which causes 50 per cent inhibition (I50) of an enzymatic reaction. *Pergamon Press*, 3099-3108.

Clark, M. H. (2006.). Temporal transcriptomic analysis as Desulfovibrio vulgaris Hildenborough transitions into stationary phase during electron donor depletion. . *Applied and environmental microbiology, , 72(8),* , pp.5578-5588.

Dennis, E., & Garrelfs, J. (2014). Corrosion of Iron by Sulfate-Reducing Bacteria: New Views of an Old Problem. *Applied and Environmental Microbiology*, 1226 - 1236.

Dou, W., Jia, R., Jin, P., Liu, J., Chen, S., & Gu, T. (2018). Investigation of the mechanism and characteristics of copper corrosion by sulfate reducing bacteria. *Corrosion Science*, *144*, 237–248. https://doi.org/10.1016/j.corsci.2018.08.055

Dou, W., Pu, Y., Han, X., Song, Y., Chen, S., & Gu, T. (2020). Corrosion of CU by a sulfate reducing bacterium in anaerobic vials with different headspace volumes. *Bioelectrochemistry*, *133*, 107478. https://doi.org/10.1016/j.bioelechem.2020.107478

Duarte, A. G., Catarino, T., White, G. F., Lousa, D., Neukirchen, S., Soares, C. M., . . . Pereira, I. A. (2018). An electrogenic redox loop in sulfate reduction reveals a likely widespread mechanism of energy conservation. *nature communications*.

Enning, D., & Garrels, J. (2014). Corrosion of iron by sulfate-reducing bacteria: new views of an old problem. *Applied Environmental Microbiology*, 1226-1236.

Era, Y., Dennis, J. A., Horsfall, L. E., & Wallace, S. (2022). Palladium Nanoparticles from Desulfovibrio alaskensis G20 Catalyze Biocompatible Sonogashira and Biohydrogenation Cascades. *ACS Publications*, 2446–2452.

Fatah, Martin, Ismail, C, M., Wahjoedi, A, B., . . . Sulistyo, E. e. (2019). Pitting Depth Prediction Caused by SRB using Empirical Equation. *Rekayasa Mesin*, 37-43.

Fernandez, V. M., Rua, M. L., Reyes, P., Cammack, R., & Hatchikian, C. (1989). Inhibition of Desuvovibrio gigas hydrogenase with copper salts and other metal ions. *Eur. J. Biochem.*, 449-454.

Fitz, R. M., & Cypionka, H. (1991). Generation of a proton gradient in Desuifovibrio vulgaris . *Archives of Microbiology*, 444-448.

Flanagan, D. M. (2023). *USGS science for a changing world*. Retrieved from USGS National Minerals Information Center : https://www.usgs.gov/centers/national-minerals-information-center/copper-statistics-and-information

Flemming, H. a. (2010). The biofilm matrix. . *Nature reviews microbiology,, 8(9),* , pp.623-633.

Franco, L. S., & Fields, M. (2018). Cr (VI) reduction and physiological toxicity are impacted by resource ratio in Desulfovibrio vulgaris. . *Applied microbiology and biotechnology,* , pp.2839-2850.

Gámez-Espinosa, Erasmo, Barberia-Roque, Leyanet, Obid, Folashade, O., . . . Cecilia, e. a. (2020). Antifungal applications for nano-additives synthesized with a bio-based approach. *Advances in Natural Sciences: Nanoscience and Nanotechnology*, 11 015019.

Geesey, G. G., Mittelman, M. W., Iwaoka, T., & Griffiths, P. R. (1986). Role of Bacterial Exopolymers in the Deterioration of Metallic Copper Surfaces. *Perform*, *25*, 37–40.

Gomes, B., I., Simones, Manuel, Simoes, & al., L. C. (2020). Copper Surfaces in Biofilm Control. *nanomaterials MDPI*, 10(12): 2491.

Grzesik, W., Kruszynski, B., & Ruszaj, A. (2010). Surface integrity of machined surfaces. *Surface Integrity in Machining*, 143–179. https://doi.org/10.1007/978-1-84882-874-2_5

Gu, T. (2012). New Understanding of Biocorrosion Mechanism and their Classifications. *Journal of Microbial & Biochemical Technology*, 4:4.

Guibaud, G., Tixier, N., Bouju, A., & Baudu, M. (2003). Relation between extracellular polymers' composition and its ability to complex CD, Cu and Pb. *Chemosphere*, *52*(10), 1701–1710. https://doi.org/10.1016/s0045-6535(03)00355-2

Güngör, N. D., Çotuk, A., & Dışpınar, D. (2015). The effect of desulfovibrio sp.. Biofilms on corrosion behavior of copper in sulfide-containing solutions. *Journal of Materials Engineering and Performance*, *24*(3), 1357–1364. https://doi.org/10.1007/s11665-015-1388-2

Harrison, J., Joe, Ceri, Howard, Turner, & Raymond J., e. a. (2007). Multimetal resistance and tolerance in microbial biofilms. *nature reviews microbiology*, 928-938.

Huang, Guangtuan, Chan, Kwong-Yu, Fang, & P., H. H. (2004). Microbiologically Induced Corrosion of 70Cu-30Ni Alloy in Anaerobic Seawater. *Journal of The Electrochemical Society*.

Ilhan-Sungur, E., & Cotuk, A. (2009). Microbial corrosion of galvanized steel in a simulated recirculating cooling tower system. *Corrosion Science*, 161-171.

Javaherdashti, R. (1999). A review of some characteristics of MIC caused by sulfate-reducing bacteria: Past, present and future. *Anti-Corrosion Methods and Materials*, *46*(3), 173–180. https://doi.org/10.1108/00035599910273142

Javaherdashti, R., & Akvan, F. (2019). Chapter 5 - Innovation, Uncertainty, and FMEA-MIC and FCP-MIC. In R. Javaherdashti, & F. Akvan, *Failure Modes, Effects and Causes of Microbiologically Influenced Corrosion* (pp. 175-212). Perth, Australia: Elsevier.

Javed, M. A. (2016). MICROBIOLOGICALLY INFLUENCED CORROSION OF COPPER AND ITS ALLOYS – A REVIEW. *Conference: Corrosion and Prevention 2016* (pp. Paper 84 - Page 1). Auckland: Corrosion & Prevention 2016.

Kalajahi, S. T. (2020). Green mitigation of microbial corrosion by copper nanoparticles. *Environmental Science and Pollution Research* , 40537–40551.

Keller, K. L., Rapp-Giles, B. J., Semkiw, E. S., Porat, I., Brown, S. D., & Wall, J. D. (2014). New Model for Electron Flow for Sulfate Reduction in Desulfovibrio alaskensis G20. *Applied and Environmental Microbiology*.

King, F., Chen, J., Qin, Z., Shoesmith, D., & Lilja, C. (2017). Sulphide-transport control of the corrosion of copper canisters. *Corrosion Engineering, Science and Technology*, *52*(sup1), 210–216. https://doi.org/10.1080/1478422x.2017.1300363

King, F., Christina, L., Vahanen, & Marjut, E. A. (2013). Progress in the understanding of the long-term corrosion behaviour of copper canisters. *Journal of Nuclear Materials*, 228-237.

Kinzler, K., Gehrke, T., Sand, & W., e. a. (2003). Bioleaching—a result of interfacial processes caused by extracellular polymeric substances (EPS). *Hydrometallurgy*, 83-88.

Klonowska, A. C. (2008.). Hexavalent chromium reduction in Desulfovibrio vulgaris Hildenborough causes transitory inhibition of sulfate reduction and cell growth. *Applied microbiology and biotechnology*, 78, pp.1007-1016.

Koch, G., Varney, J., Thompson, N., Moghissi, O., Gould, M., & Payer, J. (2016). *International Measures of Preventation, Application, and Economics of Corrosion Technologies Study.* Houston: NACE International.

Koch, H, Gerhardus, Brongers, P.H, M., Thompson, . . . Neil. (2002). *Corrosion Costs And Preventive Strategies In The United States.* Houston: NACE International.

Kokalj, Anton, Peljhan, Sebastijan, Finsgar, Matjaz, . . . Ingrid. (2010). What Determines the Inhibition Effectiveness of ATA, BTAH, and BTAOH Corrosion Inhibitors on Copper? *JACS*, 16657–16668.

Korte, H. L., Fels, S. R., Christensen, G. A., Price, M. N., Kuehl, J. V., Zane, G. M., . . . Wall, J. D. (2014). Genetic basis for nitrate resistance in Desulfovibrio strains. *Frontiers in Microbiology*, 5: 153.

Krantz, G. P., Lucas, K., Wunderlich, E. L., Hoang, L. T., Avci, R., Siuzdak, G., & Fields, M. W. (2019). Bulk phase resource ratio alters carbon steel corrosion rates and endogenously-produced extracellular electron transfer mediators in a sulfate-reducing biofilm. *Biofouling*, 35(6).

Kuehl, J. V., Price, M. N., Ray, J., Wetmore, K. M., Esquivel, Z., Kazakov, A. E., . . . Deutschbauer, A. (2014). Functional Genomics with a Comprehensive Library of Transposon Mutants for the Sulfate-Reducing Bacterium Desulfovibrio alaskensis G20. *American Society for Microbiology*, Volume 5 Issue 3 .

Kuever, J. (2014). The Family Desulfobacteraceae. In E. Rosenberg, E. F. DeLong, S. Lory, E. Stackebrandt, & F. Thompson, *The Prokaryotes* (pp. 45-73). r Heidelberg New York Dordrecht London: Springer.

Kumar Tripathi, P. S. (2022). Transcriptomics and Functional Analysis of Copper Stress Response in the Sulfate-Reducing Bacterium Desulfovibrio alaskensis G20. . *International Journal of Molecular Sciences*.

Kumar, P., & Nagarajan, R. (2011). An elegant room temperature procedure for the precise control of composition in the Cu–S System. *Inorganic Chemistry*, *50*(19), 9204–9206. https://doi.org/10.1021/ic201133a

Kumar, K. C., & Rao, B. V. (2016). Mitigation of microbially influenced corrosion of Cu–Ni (90/10) alloy in a seawater environment. *Research on Chemical Intermediates*, 5807-5823.

Lane, R. A. (2005). *Under the Microscope: Understanding, Detecting, and Preventing Microbiologically Influenced Corrosion* . NY: ASM International.

Leavitt, D., W., Flynn, M., T., Suess, K., M., & Bradley, A. S. (2016). Transhydrogenase and Growth Substrate Influence Lipid Hydrogen Isotope Ratios in Desulfovibrio alaskensis G20. *Frontiers*.

Lee, W., Lewandowski, Z., Nielsen, P. H., & Hamilton, W. A. (1995). Role of sulfate-reducing bacteria in corrosion of Mild Steel: A Review. *Biofouling*, *8*(3), 165–194. https://doi.org/10.1080/08927019509378271

Little, B. J., Blackwood, D. J., Hinks, J., Lauro, F. M., Marsili, E., Okamoto, A., Rice, S. A., Wade, S. A., & Flemming, H.-C. (2020). Microbially influenced corrosion—any progress? *Corrosion Science*, *170*, 108641. https://doi.org/10.1016/j.corsci.2020.108641

Little, B. J., & Lee, J. L. (2009). MICROBIOLOGICALLY INFLUENCED CORROSION. In B. J. Little, & J. L. Lee, *MICROBIOLOGICALLY INFLUENCED CORROSION* (pp. 1-42). Wiley Online Library.

Little, B. J., & Lee, J. S. (2009). Microbiologically Influenced Corrosion. In *Kirk-Othmer Encyclopedia of Chemical Technology.* Wiley Online Library.

Little, B. J., & Lee, J. S. (2009). *MICROBIOLOGICALLY INFLUENCED CORROSION.* Wiley Online Library.

Little, Brenda, J., Lee, Jason, & S. (2009). *MICROBIOLOGICALLY INFLUENCED CORROSION.* Wiley Online Library.

Little, Brenda, Wagner, Pat, Jacobus, & John. (1988). The Impact of Sulfate-Reducing Bacteria on Welded Copper-Nickel Seawater Piping Systems. *Materials Selection & Design*, 57-61.

Little, Brenda, Wagner, Patricia, Angell, Peter, . . . David. (1996). *International Biodeterioration & Biodegradation*, 159-162.

Liu, H., Gu, T., Zhang, G., Cheng, Y., Wang, H., & Liu, H. (2016). The effect of Magneticfield on biomineralization and corrosion behavior of carbon steel induced by iron-oxidizing bacteria. *Corrosion Science*, *102*, 93–102. https://doi.org/10.1016/j.corsci.2015.09.023

Liu, Hongwei, Liu, Haixian, Zhang, & Yuxuan, e. a. (2020). Galvanic Corrosion Due to a Heterogeneous Sulfate Reducing Bacteria Biofilm. *Coatings, MDPI*, 10(11), 1116.

Liu, Tiehui, Liu, Huiguo, Hu, Y., Zhou, L., & Zheng, B. e. (2009). Growth characteristics of thermophile sulfate-reducing bacteria and its effect on carbon steel. *Materials and Corrosion*, 218-224.

Lower, S. (2023). *Chemistry LibreTexts*. Retrieved from 16.8: Electrochemical Corrosion: https://chem.libretexts.org/Bookshelves/General_Chemistry/Chem1_(Lower)/16%3A_Electrochemistry/16.08%3A_Electrochemical_Corrosion

Mansfeld, F., & Little, B. (1992). Microbiologically influenced corrosion of copper-based materials exposed to natural seawater. *Electrochimica Acta*, 2291-2297.

Mansfield, E., & Sowards, J. W. (2015). Findings and Recommendations from the NIST Workshop on Alternative Fuels and Materials: Biocorrosion. *Journal of Research of the National Institute of Standards and Technology*, 28-36.

Matcor. (2023). *MATCOR, Inc*. Retrieved from Resources - Cathotic Protection: https://www.matcor.com/resources/cathodic-protection-systems/

Mehta-Kolte, M. G., Stoeva, M. K., Mehra, A., Redford, S. A., Youngblut, M. D., Zane, G., . . . Coates, J. D. (2019). Adaptation of Desulfovibrio alaskensis G20 to perchlorate, a specific inhibitor of sulfate reduction. *Applied Microbiology International*, 1395-1406.

Metals, D. T. (2022, April). *Copper: An Ancient Metal*. Retrieved from Dartmouth Toxic Metals Superfund Research Program: https://sites.dartmouth.edu/toxmetal/more-metals/copper-an-ancient-metal/

Müller, Leopold, A., Kjeldsen, Urup, K., Rattei, Thomas, . . . Alexander, e. a. (2015). Phylogenetic and environmental diversity of DsrAB-type dissimilatory (bi)sulfite reductases. *The ISME Journal Multidciplinary of Microbial Ecology*, 1152–1165.

Muthukumar, N., Rajasekar, A., Ponmariappan, S., Mohanan, S., Maruthamuthu, S., Muralidharan, S., . . . Raghavan, M. (2003). Microbiologically influenced corrosion in petroleum product pipelines--a review. *Indian J Exp Biol*, 1012-22.

Muyzer, G., & Stams, A. J. (2008). The ecology and biotechnology of sulphate-reducing bacteria. *Nature Reviews*, 441-454.

Nakajima, K. (2019). Basic growth and crystallographic quality of Si crystals for solar cells. In K. Nakajima, *Crystal Growth of Si Ingots for Solar Cells Using Cast Furnaces* (pp. 1-61). Elsevier.

Odler, Martin, Kmošek, J., Fikrle, Marek, Kochergina, Y., & V.Erban. (2021). Arsenical copper tools of Old Kingdom Giza craftsmen: First data. *Journal of Archaeological Science: Reports*, Volume 36.

Okabe, S., Nielsen, H., P., Jones, L., W., . . . G., W. (1995). *Water Research*, 571-578.

Okabe, S., Nielsen, P. H., Jones, W. L., & Characklis, W. G. (1994). SULFIDE PRODUCT INHIBITION OF DESULFOVIBRIO DESULFURICANS IN BATCH AND CONTINOUS CULTURES. *Pergamon*.

Okabe, S., Nielsen, P., Jones, W., & Characklis, W. (1995). Sulfide product inhibition of Desulfovibrio desulfuricans in batch and continuous cultures. *Water Research*, 571-578.

Okabe, S., Nielsen, P.H., Jones, W.L., . . . W.G. (1995). Sulfide product inhibition of Desulfovibrio desulfuricans in batch and continuous cultures. *Water Research*, 571-578.

Ollik, K., & Lieder, M. (2020). Review of the Application of Graphene-Based Coatings as Anticorrosion Layers. *MDPI*.

Omajali, J. B., Mikheenko, I. P., Merroun, M. L., Wood, J., & Macaskie, L. E. (2015). Characterization of intracellular palladium nanoparticles synthesized by Desulfovibrio desulfuricans and Bacillus benzeovorans. *Journal of Nanoparticle Research*.

Ossai, C. I. (2012). Advances in Asset Management Techniques: An Overview of Corrosion Mechanisms and Mitigation Strategies for Oil and Gas Pipelines. *Internationally Scholarly Notices*.

Otrelo-Cardoso, A. R., Nair, R. R., Correia, M. A., Rivas, M. G., & Santos-Silva, T. (2014). TupA: A Tungstate Binding Protein in the Periplasm of Desulfovibrio alaskensis G20. *Inernational Journal of Molecular Sciences*, 11783-11798.

Peck, S. C., Denger, K., Burrichter, A., Irwin, S. M., Balskus, E. P., & Schleheck, D. (2019). A glycyl radical enzyme enables hydrogen sulfide production by the human intestinal bacterium Bilophila wadsworthia. *Proc Natl Acad Sci U S A*, 3171–3176.

Perrin, D. D. (1982). *Ionisation Constants of Inorganic Acids and Bases in Aqueous Solution* (2nd ed.). Pergamon Press Ltd.

Pope, D. H., & Morris, I. E. A. (1995). Some experiences with microbiologically influenced corrosion of pipelines, Mater. *Perform*, *34*. https://doi.org/https://doi.org/10.2172/793996

Postgate, J. R. (1979). *The sulphate-reducing bacteria.* London: Cambridge University Press 1979.

Price, M. N., Ray, J., Wetmore, K. M., Kuehl, J. V., Bauer, S., Deutschbauer, A. M., & Arkin, A. P. (2014). The genetic basis of energy conservation in the sulfate-reducing bacterium Desulfovibrio alaskensis G20. *Frontiers*.

Puigdomenech, I., & Taxen, C. (1970, January 1). *Thermodynamic data for copper. implications for the corrosion of copper under repository conditions*. inis.iaea.org. http://inis.iaea.org/Search/search.aspx?orig_q=RN%3A32010691

Puigdomenech, I. a. (2000). Thermodynamic data for copper. Implications for the corrosion of copper under repository conditions (No. SKB-TR--00-13). *Swedish Nuclear Fuel and Waste Management Co*.

Rabus, Ralf, Hansen, A., T., Widdel, & Friedrich, e. a. (2013). Dissimilatory Sulfate- and Sulfur-Reducing Prokaryotes. In E. Rosenberg, E. F. Delong, S. Lory, E. Stackebrandt, & F. Thompson, *The Prokaryotes* (pp. 309-404). r Heidelberg New York Dordrecht London: Springer.

Rey, F. E., Faith, J. J., Bain, J., Muehlbauer, M. J., Stevens, R. D., Newgard, C. B., & Gordon, J. I. (2010). Dissecting the in Vivo Metabolic Potential of Two Human Gut Acetogens. *Journal of Biological Chemistry*, 2082–22090.

Rickard, D. (2012). *Sulfidic Sediments and Sedimentary Rocks.* Amsterdam: Elsevier .

Roberta, A., & Amit, A. (2022). Microbiologically Influenced Corrosion of Copper and Its Alloys in Anaerobic Aqueous Environments: A Review. *Frontiers in Microbiology*.

Roy, A. S., Sharma, A., Thapa, B. S., Pandit, S., Lahiri, D., Nag, M., . . . Mubarak, M. S. (2022). Microbiomics for enhancing electron transfer in an electrochemical system. *frontiers in Microbiology*.

Sani, Kumar, R., Peyton, M., B., Brown, & al., L. T. (2001). Copper-Induced Inhibition of Growth of Desulfovibrio desulfuricans G20: Assessment of Its Toxicity and Correlation with Those of Zinc and Lead. *Applied and Environemntal Microbiology*, 4765-4772.

Sani, R. K., Geesey, G., & Peyton, B. M. (2001). Assessment of lead toxicity to Desulfovibrio desulfuricans G20: influence of components of lactate C medium. *Advances in Environmental Research*, 269-276.

Sarioğlu, F., Javaherdashti, R., & Aksöz, N. (1997). Corrosion of a drilling pipe steel in an environment containing sulphate-reducing bacteria. *International Journal of Pressure Vessels and Piping*, *73*(2), 127–131. https://doi.org/10.1016/s0308-0161(97)00022-7

Sherif, M., E.-S., Erasmus, M., R., Comins, & D., J. (2008). Inhibition of copper corrosion in acidic chloride pickling solutions by 5-(3-aminophenyl)-tetrazole as a corrosion inhibitor. *Corrosion Science*, 3439-3445.

Shifler, D. A. (2022). Localized Corrosion. In D. A. Shifler, *LaQue's Handbook of Marine Corrosion* (pp. 63-121). John Wiley & Sons, Inc.

Singhbabu, Y. N., s, Sivakumar, B., Singh, J. K., Bapari, H., Pramanick, A. K., & Sahu, R. K. (2015). Efficient anti-corrosive coating of cold-rolled steel in a seawater environment using an oil-based graphene oxide ink. *Nanoscale*, 8035-8047.

Song, Young-Chae, Piak, Cheon, B., Shin, Sik, H., . . . Jin, S. (1998). Influence of electron donor and toxic materials on the activity of sulfate reducing bacteria for the treatment of electroplating wastewater. *Water Science and Technology*, 187-194.

Syed, A., Zeyad, M. T., Shahid, M., Elgorban, A. M., Alkhulaifi, M. M., & Ansari, I. A. (2021). Heavy Metals Induced Modulations in Growth, Physiology, Cellular Viability, and Biofilm Formation of an Identified Bacterial Isolate. *ACS OMEGA*, 25076–25088.

Sykopra, Miroslav, Kreislova, Katerina, Pokorny, & Petr, e. a. (2020). Corrosion of historic grey cast irons: indicative rates, significance, and protection. *International Journal of Computational Methods and Experimental Measurements*, 162-174.

Talha, M., Ma, Y., Kumar, P., Lin, Y., & Singh, A. (2019). Role of protein adsorption in the Bio Corrosion of metallic implants – a review. *Colloids and Surfaces B: Biointerfaces*, *176*, 494–506. https://doi.org/10.1016/j.colsurfb.2019.01.038

Temple, K. L., & Le Roux, N. W. (1964). Syngenesis of sulfide ores; sulfate-reducing bacteria and copper toxicity. *Economic Geology*, 271-278.

Trelewicz, J. R., & Schuh, C. A. (2009). Grain boundary segregation and thermodynamically stable binary nanocrystalline alloys. *MIT Libraries*.

Trevors, J. T., & Cotter, C. M. (1990). *Review Copper toxicity and uptake in microorganisms*.

Utgikar, P., V., Tabak, H., H., Haines, R., J., . . . Rakesh. (2003). Quantification of toxic and inhibitory impact of copper and zinc on mixed cultures of sulfate-reducing bacteria†. *Biotechnology and Bioengineering*, 306–312.

Venzlaff, H., Enning, D., Srinivasan, J., Mayrhofer, K. J., Hassel, A. W., Widdel, F., & Stratmann, M. (2013). Accelerated cathodic reaction in microbial corrosion of iron due to direct electron uptake by sulfate-reducing bacteria. *Corrosion Science*, 88-96.

Wadood, Zeshan, H., Rajasekar, Aruliah, Farooq, Ameeq, . . . Nasim, A. (2019). Biocorrosion inhibition of Cu70:Ni30 by Bacillus subtilis strain S1X and Pseudomonas aeruginosa strain ZK biofilms. *Journal of Basic Micriobiology*, 243-252.

Wagner, P., & Little, B. (1993). *Impact of Alloying on Microbiologically Influenced Corrosion-A Review*.

Wall, D, J, Rapp-Giles, B, & Rousset. (1993). Characterization of a small plasmid from Desulfovibrio desulfuricans and its use for shuttle vector construction. *Journal of Bacteriology*, 4121-4128.

Wang, P., & Cai, D. (2020). Preparation of Graphene-Modified Anticorrosion Coating and Study on Its Corrosion Resistance Mechanism. *International Journal of Photoenergy*.

Wang, D., Liu, J., Jia, R., Dou, W., Kumseranee, S., Punpruk, S., Li, X., & Gu, T. (2020). Distinguishing two different microbiologically influenced corrosion (MIC) mechanisms using an electron mediator and hydrogen evolution detection. *Corrosion Science*, *177*, 108993. https://doi.org/10.1016/j.corsci.2020.108993

Wang, H., Ju, L.-K., Castaneda, H., Cheng, G., & Zhang Newby, B. (2014). Corrosion of carbon steel C1010 in the presence of iron oxidizing bacteria acidithiobacillus ferrooxidans. *Corrosion Science*, *89*, 250–257. https://doi.org/10.1016/j.corsci.2014.09.005

Wang, Y., Zhang, R., Duan, J., Shi, X., Zhang, Y., Guan, F., . . . Hou, B. (2022). Extracellular Polymeric Substances and Biocorrosion/Biofouling: Recent Advances and Future Perspectives. *International Journal of Molecular Sciences*.

Wen, Sun, Lida, Wang, Tingting, Wu, . . . Guichang, e. a. (2015). Inhibited corrosion-promotion activity of graphene encapsulated in nanosized silicon oxide. *Lournal of Materials Chemistry A*.

Wei, S. H., Xu, Q., Huang, B., Zhao, Y., Yan, Y., & Noufi, R. (2012). tability and Electronic Structures of CuxS Solar Cell Absorbers: Preprint, in: IEEE Photovolt. Spec. Conf. Austin, TX.

Whitney, J. C., Hay, L. D., Li, C., Eckford, P. D., Robinson, H., Amaya, M. F., . . . Howell, P. L. (2011). Structural basis for alginate secretion across the bacterial outer membrane. *Proceedings of the National Academy of Sciences of the United States of America*, 13083-13088.

Xiang, T., Han, Y., Guo, Z., Wang, R., Zheng, S., Li, S., . . . Dai, X. (2018). Fabrication of Inherent Anticorrosion Superhydrophobic Surfaces on Metals. *ACS Sustainable Chemistry & Engineering*, 5598–5606.

Xie, Minwei, Alsina, A., M., Yuen, J., Packman, . . . Gaillard, J.-F. (2019). Effects of resuspension on the mobility and chemical speciation of zinc in contaminated sediments. *Journal of Hazardous Materials*, 300-308.

Yang, Y., & Cheng, Y. F. (2017). Factors Affecting the Performance and Applicability of SrTiO3 Photoelectrodes for Photoinduced Cathodic Protection. *The Electrochemical Society*.

Yao, W.-L., Lin, J. C., Salamanca, E., Pan, Y.-H., Tsai, P.-Y., Leu, S.-J., Yang, K.-C., Huang, H.-M., Huang, H.-Y., & Chang, W.-J. (2020). Er,CR:YSGG laser performance improves biological response on titanium surfaces. *Materials*, *13*(3), 756. https://doi.org/10.3390/ma13030756

Yoda, I., Koseki, H., Tomita, M., Shida, T., Horiuchi, H., Sakoda, H., & Osaki, M. (2014). Effect of surface roughness of biomaterials on Staphylococcus epidermidis adhesion. *BMC Microbiology*, *14*(1). https://doi.org/10.1186/s12866-014-0234-2

Yu, P., Wang, C., Zhou, J., Jiang, L., Xue, J., & Li, W. (2016). Influence of surface properties on adhesion forces and attachment of*streptococcus mutans*to zirconia*in vitro*. *BioMed Research International*, *2016*, 1–10. https://doi.org/10.1155/2016/8901253

Yuan, S., Liang, B., Zhao, Y., & Pehkonen, S. O. (2013). Surface Chemistry and corrosion behaviour of 304 stainless steel in simulated seawater containing inorganic sulphide and sulphate-reducing bacteria. *Corrosion Science*, *74*, 353–366. https://doi.org/10.1016/j.corsci.2013.04.058

Zhang, Y., Zhao, H., Qian, L., Sun, M., Lv, X., Zhang, L., Petersen, J., & Qiu, G. (2020). A brief overview on the dissolution mechanisms of sulfide minerals in acidic sulfate environments at low temperatures: Emphasis on electrochemical cyclic voltammetry analysis. *Minerals Engineering*, *158*, 106586. https://doi.org/10.1016/j.mineng.2020.106586

Zhang, L., Yu, X., Sun, H., Ge, Y., Wang, C., Li, L., . . . Gao, Q. (2023). Corrosion Behavior on 20# Pipeline Steel by Sulfate-Reducing Bacteria in Simulated NaCl Alkali/Surfactant/Polymer Produced Solution. *ACS Publications*, 13955–13966.

Zhang, W., Lee, S., McNear, K. L., Chung, T. F., Lee, S., Lee, K., . . . Yang, C. (2014). Use of graphene as protection film in biological environments. *Scientific reports*.

Zheng, S., Bawazir, M., Dhall, A., Kim, H.-E., He, L., Heo, J., & Hwang, G. (2021). Implication of surface properties, bacterial motility, and hydrodynamic conditions on bacterial surface sensing and their initial adhesion. *Frontiers in Bioengineering and Biotechnology*, *9*. https://doi.org/10.3389/fbioe.2021.643722

Zhu, Y., X., Lubeck, John, II, K., & al., J. J. (2003). Characterization of Microbial Communities in Gas Industry Pipelines. *Applied and Environmental Microbiology*.

Zuo, Y., Wang, H., & Xiong, J. (2002). The aspect ratio of surface grooves and metastable pitting of stainless steel. *Corrosion Science*, *44*(1), 25–35. https://doi.org/10.1016/s0010-938x(01)00039-7

APPENDICES

APPENDIX A

TABULATED DATA FROM COPPER TOXICITY

Table A. 1: It represents Oleidesulfovibrio alaskensis G20 cultures grown in LS4D BAL (60L:30S) in copper free tubes and in the presence of 6 µM copper ions (Cu^{+2}) for 7 days.

				0 µM Cu^{+2}					**6 µM Cu^{+2}**				
Date	**Sampling Time**	**Time (h)**	**Δh (h)**	**Tube 1**	**Tube 2**	**Tube 3**	**Average**	**StD**	**Tube 1**	**Tube 2**	**Tube 3**	**Average**	**StD**
11/9/2021	4:00 PM	0.00	0	0.058	0.056	0.062	0.059	0.003	0.062	0.066	0.061	0.063	0.003
11/9/2021	8:30 PM	4.50	4.5	0.077	0.091	0.083	0.084	0.007	0.049	0.052	0.046	0.049	0.003
11/10/2021	12:30 AM	8.50	4	0.103	0.109	0.118	0.110	0.008	0.05	0.054	0.055	0.053	0.003
11/10/2021	8:00 AM	16.00	7.5	0.228	0.219	0.231	0.226	0.006	0.051	0.055	0.05	0.052	0.003
11/10/2021	12:00 PM	20.00	4	0.421	0.355	0.393	0.390	0.033	0.049	0.053	0.048	0.050	0.003
11/10/2021	6:00 PM	26.00	6	0.822	0.764	0.817	0.801	0.032	0.043	0.054	0.05	0.049	0.006
11/10/2021	11:30 PM	31.50	5.5	1.047	1.053	1.059	1.053	0.006	0.044	0.055	0.057	0.052	0.007
11/11/2021	11:00 AM	43.00	11.5	1.16	1.203	1.194	1.186	0.023	0.042	0.056	0.092	0.063	0.026
11/11/2021	3:00 PM	47.00	4	1.203	1.23	1.206	1.213	0.015	0.045	0.057	0.133	0.078	0.048
11/12/2021	12:00 PM	68.00	21	1.18	1.17	1.195	1.182	0.013	0.037	0.048	1.304	0.463	0.728
11/14/2021	4:00 PM	120.00	52	1.088	1.111	1.126	1.108	0.019	0.04	0.05	1.319	0.470	0.736
11/15/2021	4:00 PM	144.00	24	1.08	1.097	1.11	1.096	0.015	0.036	0.071	1.301	0.469	0.720
11/18/2021	10.30 AM	211		1.064	1.092	1.098	1.084	0.0181	0.034	1.293	1.309	0.8786	0.731

Table A. 2: It represents *Oleidesulfovibrio alaskensis* G20 cultures grown in LS4D BAL (60L:30S) in the presence of 12 and 16 µM for 7 days.

				12 µM Cu^{+2}					**16 µM Cu^{+2}**				
Date	**Sampling Time**	**Time (h)**	**Δh (h)**	**Tube 1**	**Tube 2**	**Tube 3**	**Average**	**StD**	**Tube 1**	**Tube 2**	**Tube 3**	**Average**	**StD**
11/9/2021	4:00 PM	0.00	0	0.041	0.041	0.044	0.042	0.005	0.063	0.061	0.063	0.062	0.001
11/9/2021	8:30 PM	4.50	4.5	0.044	0.098	0.051	0.064	0.004	0.055	0.056	0.053	0.055	0.002
11/10/2021	12:30 AM	8.50	4	0.047	0.145	0.047	0.080	0.003	0.062	0.06	0.058	0.060	0.002
11/10/2021	8:00 AM	16.00	7.5	0.046	0.332	0.047	0.142	0.002	0.059	0.062	0.054	0.058	0.004
11/10/2021	12:00 PM	20.00	4	0.055	1.009	0.048	0.371	0.005	0.058	0.056	0.062	0.059	0.003
11/10/2021	6:00 PM	26.00	6	0.061	1.128	0.05	0.413	0.002	0.061	0.057	0.056	0.058	0.003
11/10/2021	11:30 PM	31.50	5.5	0.351	1.273	0.041	0.555	0.006	0.063	0.056	0.054	0.058	0.005
11/11/2021	11:00 AM	43.00	11.5	1.224	1.238	0.043	0.835	0.005	0.062	0.058	0.051	0.057	0.006
11/11/2021	3:00 PM	47.00	4	1.234	1.246	0.033	0.838	0.014	0.058	0.06	0.055	0.058	0.003
11/12/2021	12:00 PM	68.00	21	1.33	1.24	0.032	0.838	0.007	0.051	0.05	0.049	0.050	0.001
11/14/2021	4:00 PM	120.00	52	1.213	1.29	0.032	0.836	0.003	0.049	0.049	0.07	0.056	0.012
11/15/2021	4:00 PM	144.00	24	1.25	1.34	0.032	0.842	0.002	0.045	0.049	0.567	0.220	0.300
11/18/2021	10.30 AM	211		1.23	1.31	0.032		0.002	0.044	0.046	1.286	0.458	0.716

Table A. 3: It represents *Oleidesulfovibrio alaskensis* cultures grown in LS4D BAL (60L:30S) in the presence of 24 μM for 7 days.

Date	**Sampling Time**	**Time (h)**	**Delta T**	**Tube 1**	**Tube 2**	**Tube 3**	**Average**	**StD**
11/9/2021	**4:00** PM	**0.00**	0	**0.061**	**0.059**	**0.06**	**0.060**	**0.001**
11/9/2021	8:30 PM	4.50	4.5	0.06	0.057	0.056	0.058	0.002
11/10/2021	12:30 AM	8.50	4	0.065	0.061	0.059	0.062	0.003
11/10/2021	8:00 AM	16.00	7.5	0.06	0.058	0.061	0.060	0.002
11/10/2021	12:00 PM	20.00	4	0.065	0.059	0.057	0.060	0.004
11/10/2021	6:00 PM	26.00	6	0.061	0.063	0.061	0.062	0.001
11/10/2021	11:30 PM	31.50	5.5	0.059	0.06	0.059	0.059	0.001
11/11/2021	11:00 AM	43.00	11.5	0.06	0.064	0.058	0.061	0.003
11/11/2021	3:00 PM	47.00	4	0.056	0.073	0.06	0.063	0.009
11/12/2021	12:00 PM	68.00	21	0.048	0.055	0.057	0.053	0.005
11/14/2021	4:00 PM	120.00	52	0.046	0.051	0.048	0.048	0.003
11/15/2021	4:00 PM	144.00	24	0.048	0.052	0.05	0.050	0.002
11/18/2021	10.30 AM	211		0.043	0.047	0.048	0.046	0.002645751

Table A. 4: It represents Oleidesulfovibrio alaskensis cultures grown in LS4D EAL (50L:10S) in copper free and the presence of 6 µM Cu^{+2} tubes for 7 days.

				0 µM Cu^{+2}					**6 µM Cu^{+2}**				
Date	**Sampling time**	**Time (h)**	**Δh (h)**	**Tube 1**	**Tube 2**	**Tube 3**	**Average**	**StD**	**Tube 1**	**Tube 2**	**Tube 3**	**Average**	**StD**
11/9/2021	4:00 PM	0.00	0	0.064	0.051	0.057	0.057	0.007	0.06	0.052	0.073	0.062	0.011
11/9/2021	8:30 PM	4.50	4.5	0.105	0.076	0.073	0.085	0.018	0.056	0.054	0.066	0.059	0.006
11/10/2021	12:30 AM	8.50	4	0.148	0.121	0.1	0.123	0.024	0.061	0.078	0.083	0.074	0.012
11/10/2021	8:00 AM	16.00	7.5	0.374	0.353	0.192	0.306	0.100	0.075	0.102	0.087	0.088	0.014
11/10/2021	12:00 PM	20.00	4	0.624	0.565	0.357	0.515	0.140	0.08	0.184	0.1	0.121	0.055
11/10/2021	6:00 PM	26.00	6	0.638	0.717	0.752	0.702	0.058	0.09	0.359	0.107	0.185	0.151
11/10/2021	11:30 PM	31.50	5.5	0.644	0.691	0.824	0.720	0.093	0.142	0.794	0.146	0.361	0.375
11/11/2021	11:00 AM	43.00	11.5	0.632	0.675	0.79	0.699	0.082	0.592	0.88	0.477	0.650	0.208
11/11/2021	3:00 PM	47.00	4	0.643	0.691	0.836	0.723	0.100	0.832	0.892	0.843	0.856	0.032
11/12/2021	12:00 PM	68.00	21	0.601	0.643	0.776	0.673	0.091	0.7	0.825	0.892	0.806	0.097
11/14/2021	4:00 PM	120.00	52	0.572	0.6	0.697	0.623	0.066	0.806	0.762	0.871	0.813	0.055
11/15/2021	4:00 PM	144.00	24	0.584	0.625	0.731	0.647	0.076	0.801	0.798	0.856	0.818	0.033
11/18/2021	10:30 AM	211		0.595	0.595	0.693	0.627	0.056	0.8	0.78	0.864	0.814	0.043

Table A. 5: It represents *Oleidesulfovibrio alaskensis* G20 cultures grown in LS4D EAL (50L:10S) in the presence of 12 and 16 µM Cu^{+2} tubes for 7 days.

				12 µM Cu^{+2}					**16 µM Cu^{+2}**				
Date	**Sampling time**	**Time (h)**	**Δh (h)**	**Tube 1**	**Tube 2**	**Tube 3**	**Average**	**StD**	**Tube 1**	**Tube 2**	**Tube 3**	**Average**	**StD**
11/9/2021	4:00 PM	0.00	0	0.057	0.046	0.063	0.055	0.009	0.052	0.05	0.054	0.052	0.002
11/9/2021	8:30 PM	4.50	4.5	0.058	0.046	0.053	0.052	0.006	0.062	0.057	0.054	0.058	0.004
11/10/2021	12:30AM	8.50	4	0.08	0.05	0.062	0.064	0.015	0.067	0.058	0.057	0.061	0.006
11/10/2021	8:00 AM	16.00	7.5	0.059	0.053	0.061	0.058	0.004	0.071	0.054	0.055	0.060	0.010
11/10/2021	12:00 PM	20.00	4	0.064	0.047	0.06	0.057	0.009	0.074	0.057	0.064	0.065	0.009
11/10/2021	6:00 PM	26.00	6	0.068	0.067	0.064	0.066	0.002	0.076	0.049	0.059	0.061	0.014
11/10/2021	11:30 PM	31.50	5.5	0.075	0.089	0.075	0.080	0.008	0.091	0.055	0.068	0.071	0.018
11/11/2021	11:00 AM	43.00	11.5	0.123	0.166	0.132	0.140	0.023	0.136	0.056	0.058	0.083	0.046
11/11/2021	3:00 PM	47.00	4	0.159	0.294	0.164	0.206	0.077	0.182	0.058	0.064	0.101	0.070
11/12/2021	12:00 PM	68.00	21	0.951	0.85	0.985	0.929	0.070	0.741	0.143	0.159	0.348	0.341
11/14/2021	4:00 PM	120.00	52	0.955	0.82	0.894	0.890	0.068	0.79	0.905	0.93	0.875	0.075
11/15/2021	4:00 PM	144.00	24	0.923	0.779	0.849	0.850	0.072	0.782	0.872	0.893	0.849	0.059
11/18/2021	10:30AM	211		0.917	0.799	0.85	0.855	0.059	0.807	0.86	0.861	0.842	0.030

Table A. 6: It represents *Oleidesulfovibrio alaskensis* G20 cultures grown in LS4D EAL (50L:10S) in the presence 24 µM Cu^{2+} tubes for 7 days.

24 µM Cu^{+2}								
Date	Samplig time	Time **(h)**	Delta **T**	Tube **1**	Tube **2**	Tube **3**	Average	StD
11/9/2021	4:00 PM	0.00	0	0.059	0.053	0.054	0.055	0.003
11/9/2021	8:30 PM	4.50	4.5	0.063	0.064	0.061	0.063	0.002
11/10/2021	12:30 AM	8.50	4	0.067	0.063	0.07	0.067	0.004
11/10/2021	8:00 AM	16.00	7.5	0.061	0.059	0.073	0.064	0.008
11/10/2021	12:00 PM	20.00	4	0.065	0.059	0.071	0.065	0.006
11/10/2021	6:00 PM	26.00	6	0.065	0.06	0.093	0.073	0.018
11/10/2021	11:30 PM	31.50	5.5	0.068	0.061	0.124	0.084	0.035
11/11/2021	11:00 AM	43.00	11.5	0.06	0.061	0.22	0.114	0.092
11/11/2021	3:00 PM	47.00	4	0.073	0.06	0.365	0.166	0.172
11/12/2021	12:00 PM	68.00	21	0.058	0.055	0.716	0.276	0.381
11/14/2021	4:00 PM	120.00	52	0.181	0.051	0.679	0.304	0.331
11/15/2021	4:00 PM	144.00	24	0.845	0.054	0.704	0.534	0.422
11/18/2021	10:30 AM			0.81	0.061	0.74	0.537	0.413711

Table A. 7: It represents *Oleidesulfovibrio alaskensis* G20 cultures grown in LS4D EDL (15L:50S) in copper free and the presence of 6 µM Cu^{2+} tubes for 7 days.

				0 µM Cu^{+2}					**6 µM Cu^{+2}**				
Date	**Sampling time**	**Time (h)**	**Δt (h)**	**Tube 1**	**Tube 2**	**Tube 3**	**Average**	**StD**	**Tube 1**	**Tube 2**	**Tube 3**	**Average**	**StD**
11/9/2021	4:00 PM	0.00	0	0.041	0.058	0.056	0.0517	0.0093	0.06	0.055	0.06	0.058	0.003
11/9/2021	8:30 PM	4.50	4.5	0.061	0.089	0.079	0.0763	0.0142	0.075	0.06	0.055	0.063	0.010
11/10/2021	12:30 AM	8.50	4	0.097	0.107	0.115	0.1063	0.0090	0.076	0.062	0.054	0.064	0.011
11/10/2021	8:00 AM	16.00	7.5	0.248	0.214	0.327	0.2630	0.0580	0.078	0.066	0.06	0.068	0.009
11/10/2021	12:00 PM	20.00	4	0.478	0.376	0.576	0.4767	0.1000	0.08	0.072	0.061	0.071	0.010
11/10/2021	6:00 PM	26.00	6	0.577	0.599	0.604	0.5933	0.0144	0.105	0.088	0.071	0.088	0.017
11/10/2021	11:30 PM	31.50	5.5	0.579	0.592	0.596	0.5890	0.0089	0.165	0.1	0.094	0.120	0.039
11/11/2021	11:00 AM	43.00	11.5	0.591	0.571	0.61	0.5907	0.0195	0.589	0.28	0.323	0.397	0.167
11/11/2021	3:00 PM	47.00	4	0.608	0.599	0.619	0.6087	0.0100	0.649	0.586	0.584	0.606	0.037
11/12/2021	12:00 PM	68.00	21	0.583	0.6	0.608	0.5970	0.0128	0.694	0.772	0.704	0.723	0.042
11/14/2021	4:00 PM	120.00	52	0.482	0.546	0.581	0.5363	0.0502	0.623	0.721	0.651	0.665	0.050
11/15/2021	4:00 PM	144.00	24	0.47	0.548	0.539	0.5190	0.0427	0.608	0.665	0.623	0.632	0.030
11/18/2021	10.30 AM			0.521	0.545	0.533	0.5330	0.0120	0.605	0.684	0.632	0.640	0.040

Table A. 8: It represents *Oleidesulfovibrio alaskensis* G20 cultures grown in LS4D EDL (15L:50S) in the presence of 12 and 16 µM Cu^{+2} tubes for 7 days.

				12 uM Cu^{+2}					**16 uM Cu^{+2}**				
Date	**Sampling time**	**Time (h)**	**Δt (h)**	**Tube 1**	**Tube 2**	**Tube 3**	**Average**	**StD**	**Tube1**	**Tube2**	**Tube3**	**Average**	**StD**
11/9/2021	4:00 PM	0.00	0	0.063	0.069	0.059	0.064	0.005	0.068	0.044	0.068	0.060	0.014
11/9/2021	8:30 PM	4.50	4.5	0.068	0.066	0.06	0.065	0.004	0.064	0.041	0.061	0.055	0.013
11/10/2021	12:30 AM	8.50	4	0.065	0.074	0.065	0.068	0.005	0.063	0.045	0.069	0.059	0.012
11/10/2021	8:00 AM	16.00	7.5	0.068	0.077	0.066	0.070	0.006	0.071	0.046	0.047	0.055	0.014
11/10/2021	12:00 PM	20.00	4	0.073	0.078	0.066	0.072	0.006	0.062	0.042	0.044	0.049	0.011
11/10/2021	6:00 PM	26.00	6	0.076	0.092	0.064	0.077	0.014	0.07	0.046	0.044	0.053	0.014
11/10/2021	11:30 PM	31.50	5.5	0.1	0.093	0.068	0.087	0.017	0.061	0.041	0.042	0.048	0.011
11/11/2021	11:00 AM	43.00	11.5	0.172	0.148	0.11	0.143	0.031	0.073	0.041	0.045	0.053	0.017
11/11/2021	3:00 PM	47.00	4	0.333	0.303	0.145	0.260	0.101	0.066	0.044	0.043	0.051	0.013
11/12/2021	12:00 PM	68.00	21	0.698	0.762	0.606	0.689	0.078	0.126	0.028	0.04	0.065	0.053
11/14/2021	4:00 PM	120.00	52	0.691	0.738	0.693	0.707	0.027	0.693	0.02	0.017	0.243	0.389
11/15/2021	4:00 PM	144.00	24	0.639	0.709	0.659	0.669	0.036	0.696	0.027	0.03	0.251	0.385
11/18/2021	10.30 AM			0.625	0.688	0.66	0.658	0.032	0.717	0.02	0.015	0.251	0.404

Table A. 9 : It represents *Oleidesulfovibrio alaskensis* G20 cultures grown in LS4D EDL (15L:50S) in the presence 24 µM Cu^{+2} tubes for 7 days

				24 uM Cu^{+2}				
Date	Sampling time	Time **(h)**	Delta **T**	Tube **1**	Tube **2**	Tube **3**	Average	StD
11/9/2021	4:00 PM	0.00	0	0.042	0.04	0.045	0.042333	0.002517
11/9/2021	8:30 PM	4.50	4.5	0.038	0.036	0.053	0.042333	0.009292
11/10/2021	12:30 AM	8.50	4	0.037	0.04	0.063	0.046667	0.014224
11/10/2021	8:00 AM	16.00	7.5	0.035	0.042	0.06	0.045667	0.012897
11/10/2021	12:00 PM	20.00	4	0.033	0.035	0.063	0.043667	0.016773
11/10/2021	6:00 PM	26.00	6	0.035	0.037	0.069	0.047	0.019079
11/10/2021	11:30 PM	31.50	5.5	0.033	0.036	0.106	0.058333	0.041308
11/11/2021	11:00 AM	43.00	11.5	0.041	0.038	0.294	0.124333	0.146943
11/11/2021	3:00 PM	47.00	4	0.039	0.037	0.536	0.204	0.287522
11/12/2021	12:00 PM	68.00	21	0.033	0.034	0.975	0.347333	0.543576
11/14/2021	4:00 PM	120.00	52	0.034	0.034	0.887	0.318333	0.49248
11/15/2021	4:00 PM	144.00	24	0.029	0.034	0.81	0.291	0.449474
11/18/2021	10.30 AM			0.029	0.034	0.855	0.306	0.475455

Maximum Growth Rate Calculations

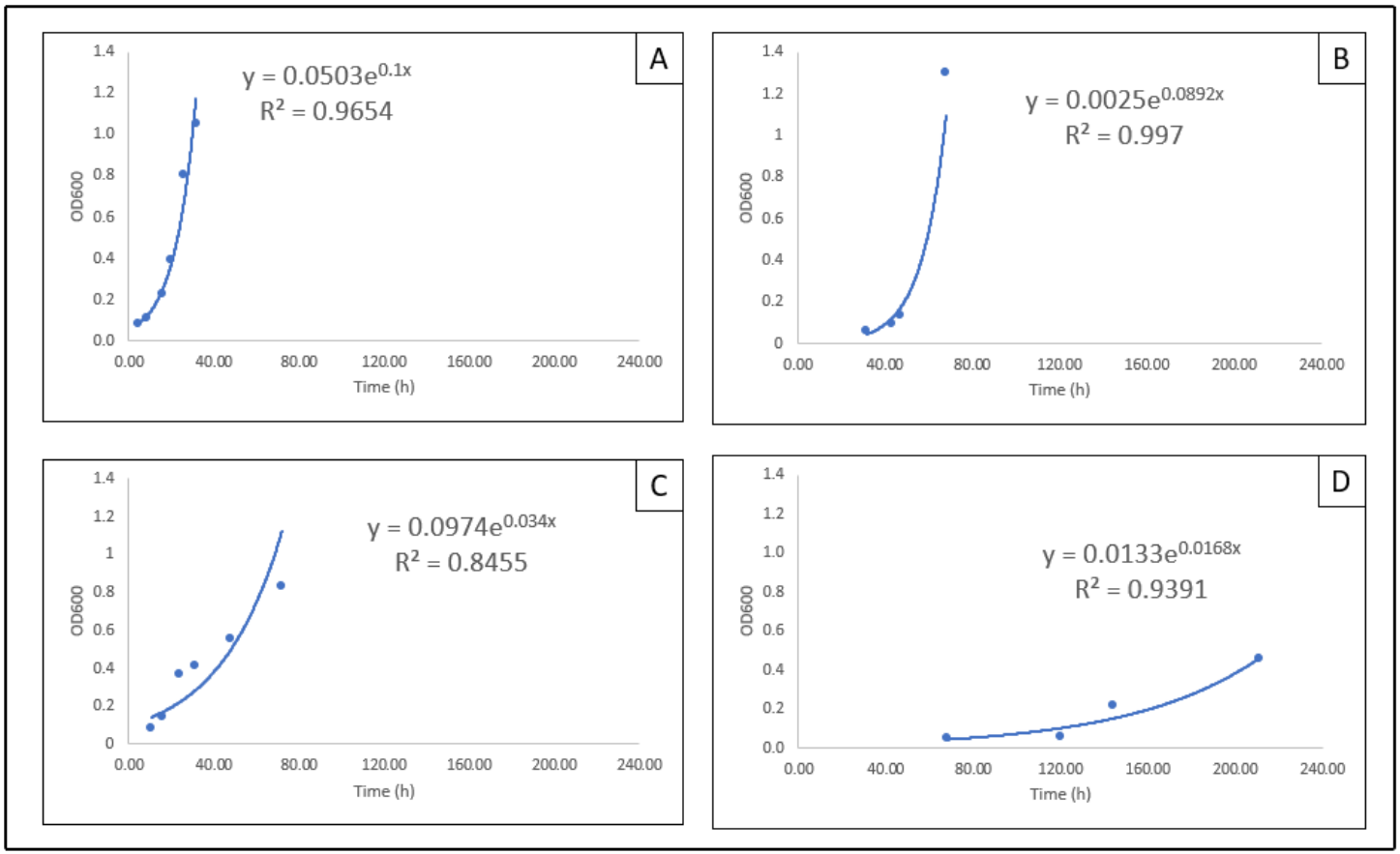


Figure A. 1: The exponential plots of growth (A) copper-free, (B) 6 µM of Cu(II) ions, (C) 12 µM of Cu(II) ions, (D) 16 µM of Cu(II) ions in LS4D-BAL medium. The cultures didn't show growth in the presence of 24 µM of Cu(II) ions in LS4D-BAL medium. $Y=Ae^{\mu x}$, each µ value refers to specific growth rate.

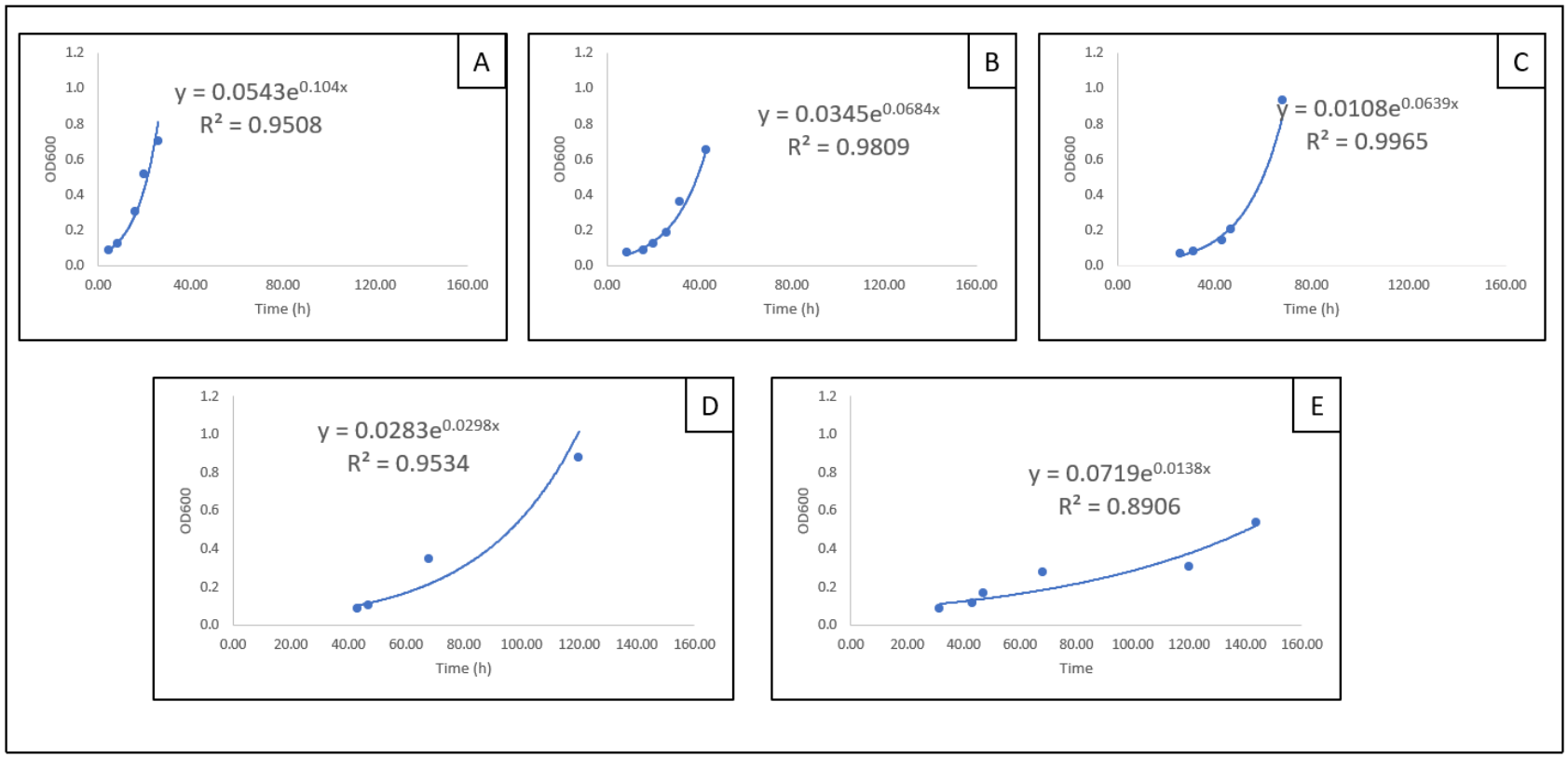


Figure A. 2: The exponential plots of growth of (A) copper-free, (B) 6 µM of Cu(II) ions, (C) 12 µM of Cu(II) ions, (D) 16 µM of Cu(II) ions and (E) 24 µM of Cu(II) ions in LS4D-EAL medium. $Y=Ae^{\mu x}$, each µ value refers to specific growth rate.

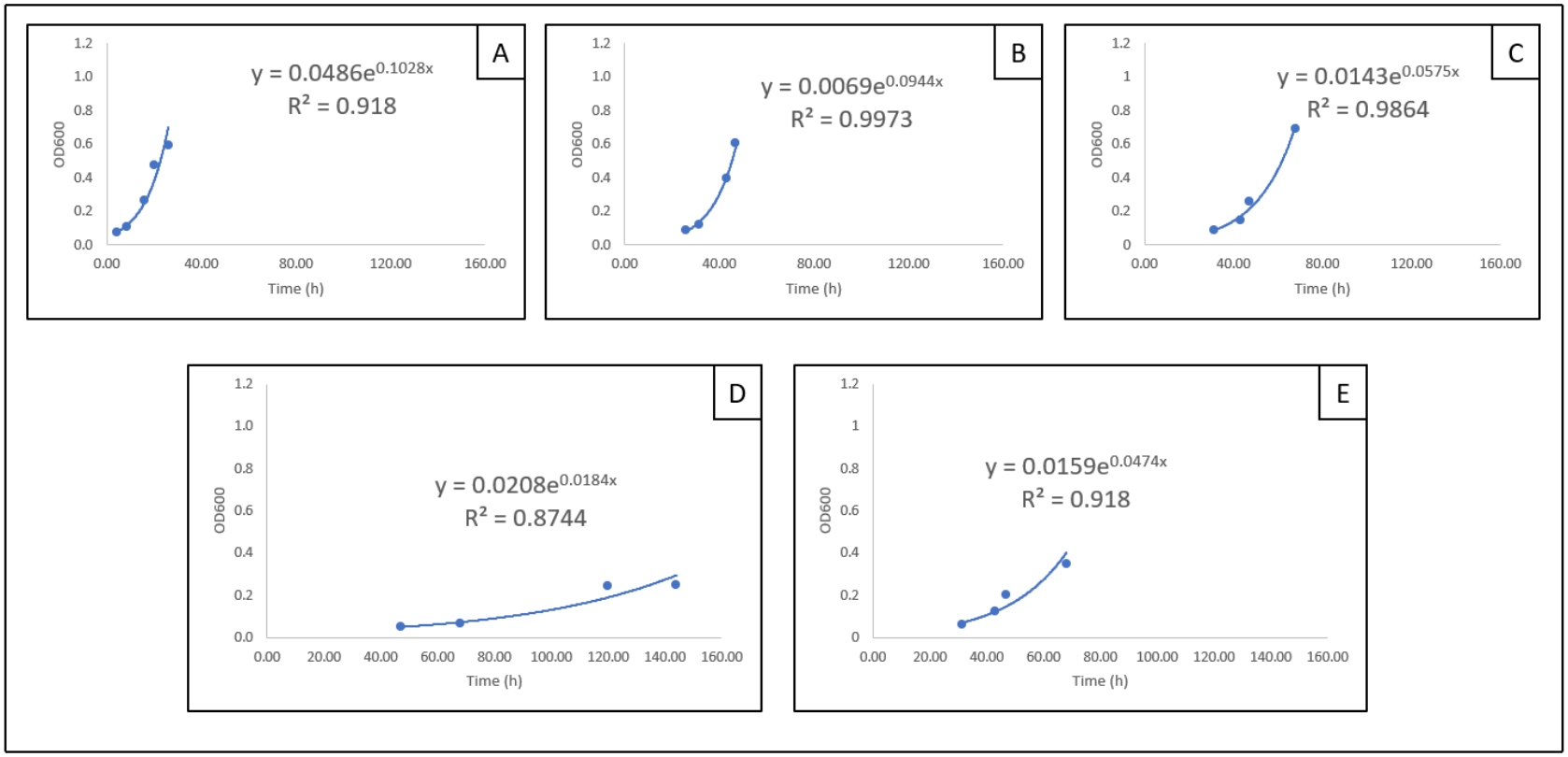


Figure A. 3: The exponential plots of growth of (A) copper-free, (B) 6 µM of Cu(II) ions, (C) 12 µM of Cu(II) ions, (D) 16 µM of Cu(II) ions and (E) 24 µM of Cu(II) ions in LS4D-EDL medium. $Y=Ae^{\mu x}$, each µ value refers to specific growth rate.

Cell Doubling Time

$$td = \frac{\ln(2)}{\mu}$$

For EAL copper-free culture;

$td = \frac{\ln(2)}{0.104}$ = 6.66 h, where μ=0.104

Can *Olediosulfovibrio alaskensis* G20 synthesize metal nanoparticles?

O. alaskensis has been shown to have the ability to synthesize metal nanoparticles, including palladium nanoparticles. These studies highlight the biogenic synthesis of metal nanoparticles by *O. alaskensis* and their potential applications. The nanoparticles produced by *O. alaskensis* have been found to be small, uniformly sized, and composed of various platinum group metals (Bloch, Pardesi, Satriano, & Ghosh, 2021; Omajali, Mikheenko, Merroun, Wood, & Macaskie, 2015; Era, Dennis, Horsfall, & Wallace, 2022). These findings suggest that *O. alaskensis* has the capability to interact with metal ions and facilitate their conversion into nanoparticles. *O. alaskensis* may produce copper metal within cells in the presence of copper ions in electron acceptor-limited and electron donor-limited environments, according to this study.

A summer research project was performed in the Imaging and Chemical Analysis Laboratory (ICAL) at MSU. The project involved a Research Experience for Undergraduates (REU) student named Dane Mansfield, researcher Bret Davis from ICAL, and myself. The objective of the project was to investigate the bio-trapping of *O. alaskensis* on steel coupons. This was achieved by functionalizing the surface of the coupons with a positively charged layer of amine groups. The aim was to observe whether bacteria would colonize the functionalized

surface and create a distinct corrosive environment due to the electrostatic attraction between the net charge on the gram-negative bacteria and the functionalized coupon surface.

Bret Davis and Dane Mansfield summarized the outcomes below:

1.There was a greater deposition of biomineralized layer seen on the functionalized surface in comparison to the control surface.

2.Localized and deeper corrosion pits on the control surface was observed.

3.The presence of additional biomineral layers on the sample has the potential to function as a protective barrier against corrosion.

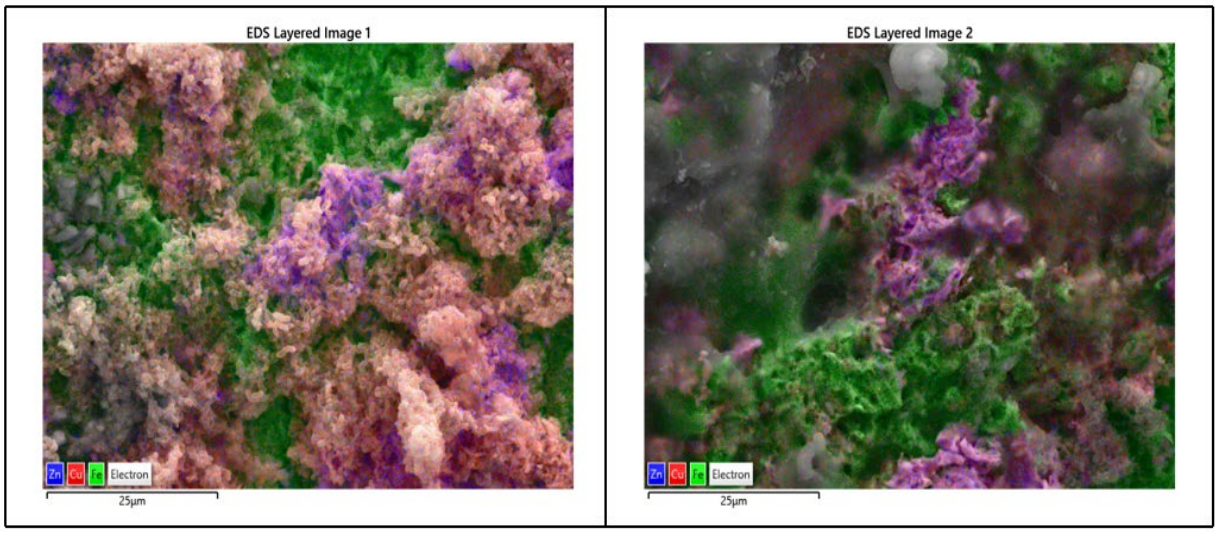


Figure A. 4: EDS layered image 1 (the unfunctionalized surface- control) and EDS layered image 2 (functionalized surface) show thick mat of biominerals including copper, zinc and iron (Images taken by Bret Davis and Dane Mansfield).

In addition to the main hypothesis, we have identified an additional observation that has the potential to contribute to the rise of a new subfield within the corrosion research and support the results from previous research on metal synthesizing property of *O. alaskensis*. The

unexpected high levels of Cu and Zn on the unfunctionalized coupons were seen, but this occurrence did not appear on the functionalized surfaces. Because the bacteria were trapped on a steel surface and predominantly interacted with it, iron was mostly recognized on functionalized surface as a deposited metal as seen Figure 3. Since these elements are only present in trace levels in the system between LS4D medium and the steel composition, it seems likely that the bacteria would scavenge and re-deposit them. Based on what is shown in Figure A.4 and the accompanying EDX spectra, it can be inferred that the bacteria exhibit a higher tendency for scavenging copper ions compared to iron and zinc ions. This may be explained a tungstate binding protein, TupA, in the periplasm of *O. alaskensis* G20. Tungstate is a copper-interacting molecule, and the presence of TupA reveals a possible link between *O. alaskensis* G20 and copper-related activities (Otrelo-Cardoso, Nair, Correia, Rivas, & Santos-Silva, 2014). The final cell density increase in the presence of copper ions in the presence of substrate-limited conditions might be a consequence of the bacteria feeling hungry, and this hunger could possibly stimulate metabolism of TupA protein and metal synthesis process.

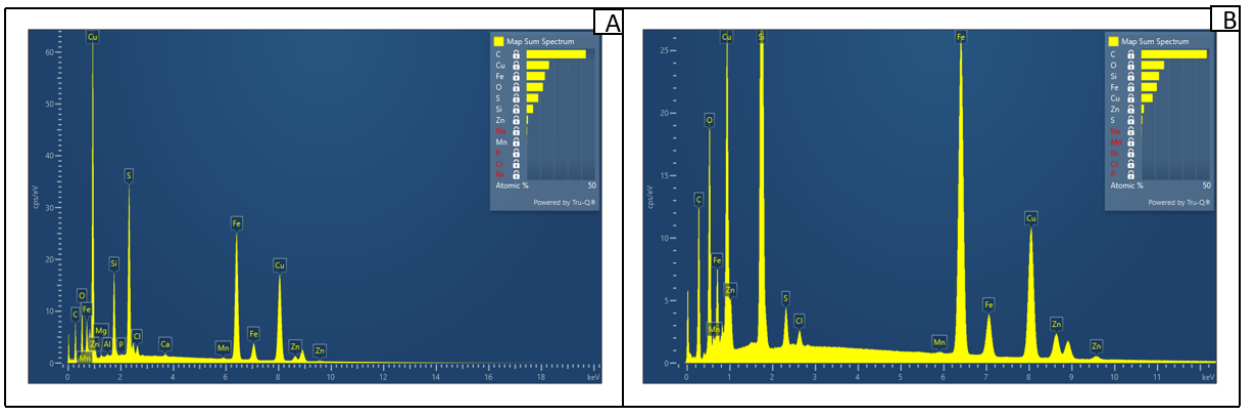


Figure A.5: The EDX chemical analysis of unfunctionalized surface of steel, control (A) and the functionalized surface (B) where the bacteria trapped to the surface.

APPENDIX B

TABULATED PITTING ANALYSIS DATA FROM EFFECTS OF SURFACE ROUGHNESS ON MICROBIOLOGICALLY INFLUENCED CORROSION (MIC) OF COPPER (101) BY OLEIDESULFOVIBRIO ALASKENSIS G20

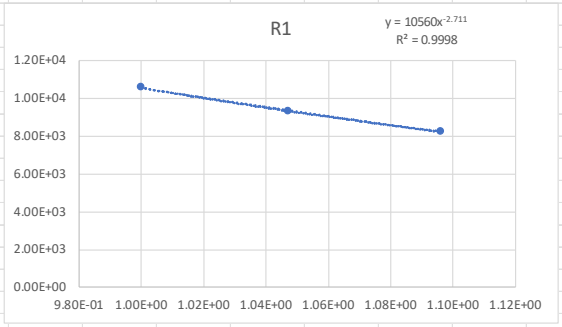
Pit Depths MATLAB Code

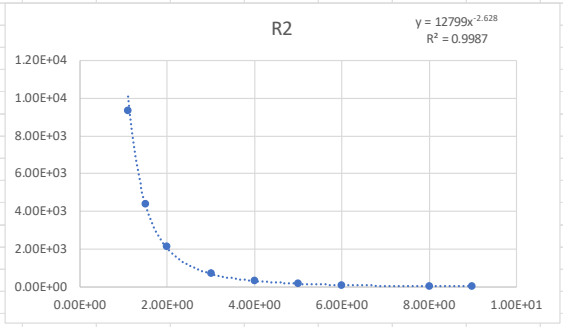
```
% Here is a program to calcualate the attenuation of x-rays through the
% copper from deep within a pit.
% The x-ray pathlength is calcuated from tabulated values of the mass -
% attenuation coeffectient (mu - from NIST) and experimental values of
% x-ray intensity as a function of energy from the pit and surface (control).
clear;clc;close all;
% load the pit spectrum.  Name the variable "pit" / i.e. load('pit.txt')
% load the control spectrum.  Name the variable "control"
pit=load('Spectrum600 2.2.txt'); control=load('Spectrum600 2.1.txt');
% load the energy axis
eV = 1000*control(:,1);
% extract the counts per second
pit=pit(:,2); control=control(:,2);
% Livetime of 100 sec for all pits, so no normalization
% Get Live time from EMSA spectrum file
% pit_LiveTime=27.166282654;
% control_LiveTime=8.223842621;
% Normalize spectra to counts per second
% pit=pit./(pit_LiveTime*10);
% control=control./(control_LiveTime*10);
% define a range over which to average the pathlength
S = 3500; % in eV
F = 5000;
% number of bins to make the histogram with
bins = 10;
% Trim the control of zeroes
ind1 = find(control);
% Trim the hole of zeroes
ind2 = find(pit);
% Make a vector of the indices of points where neither background nor hole
% signal is zero
k = 1;
for j = 1:numel(ind1)
 for i = 1:numel(ind2)
   if ind1(j) == ind2(i)
   ind(k) = ind1(j);
   k = k+1;
   end
 end
end
ind = ind';
pit = pit(ind);
```

```
control = control(ind);
eV = eV(ind);
% Now take the quotient of the background intensity and hole intensity
Q = control./pit;
% Now, give the mass-attenuation coefficient for copper (numbers are
% extrapolated from data in the range of 1:20 keV)
% reference:
% http://physics.nist.gov/PhysRefData/XrayMassCoef/ElemTab/z26.html
rho = 8.96; % density of copper grams per centimeter cubed
range = find(eV>1096);
a = range(1);
mu(1:a) = (rho*1.0560e-4)*((1e-6)*eV(1:a)).^(-2.711);
range = find(eV>8979);
b = range(1);
mu(a+1:b) = (rho*1.2799e-4)*((1e-6)*eV(a+1:b)).^(-2.628);
c = numel(eV);
mu(b+1:c) = (rho*9.3121e-4)*((1e-6)*eV(b+1:c)).^(-2.641);
mu = mu';
% Calculate the X-ray pathlength in microns
PL = sin(.61)*(log(Q)./mu)*1e4;
plot(eV,control,'-g')
hold on
plot(eV,pit,'-r')
plot(eV,PL,'-b')
xlabel('eV');
ylabel('A.U. (spectra), microns (path length)');
legend('control','pit','path length');
title('raw data');
% lower limit: where signal from hole becomes good
range = find(eV > S);
s = range(1);
% upper limit: where lower limit of Cu signal begins
range = find(eV > F);
f = range(1);
figure
histfit(PL(s:f))
title('histogram of pathlength over averaged range')
xlabel('pathlength (microns)')
ylabel('counts')
```

Copper mass attenuation coefficient

		keV	u/p	
1.00E-03		1.00E+00	1.06E+04	R1
1.05E-03		1.05E+00	9.31E+03	
1.10E-03		1.10E+00	8.24E+03	
1.10E-03		1.10E+00	9.35E+03	R2
1.50E-03		1.50E+00	4.42E+03	
2.00E-03		2.00E+00	2.15E+03	
3.00E-03		3.00E+00	7.49E+02	
4.00E-03		4.00E+00	3.47E+02	
5.00E-03		5.00E+00	1.90E+02	
6.00E-03		6.00E+00	1.16E+02	
8.00E-03		8.00E+00	5.26E+01	
8.98E-03		8.98E+00	3.83E+01	
8.98E-03		8.98E+00	2.78E+02	R3
1.00E-02		1.00E+01	2.16E+02	
1.50E-02		1.50E+01	7.41E+01	
2.00E-02		2.00E+01	3.38E+01	





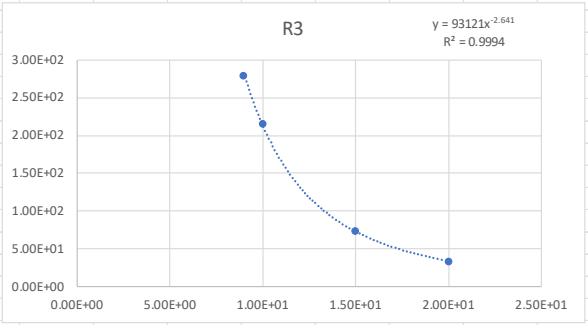


Figure B. 1. Copper mass attenuation coefficients.

Table B. 1:The average of three pit depths for each pitting measurement for all coupons.

	Pit depth 1 (µm)	Pit depth 2 (µm)	Pit depth 3 (µm)	Pit depth 4 (µm)	Pit depth 5 (µm)	Pit depth 6 (µm)	Pit depth 7 (µm)	Pit depth 8 (µm)	Pit depth 9 (µm)	Pit depth 10 (µm)
As received	2.204 +/- 0.483	4.970+/- 0.710	4.156 +/- 1.198	2.026 +/- 0.314	6.627 +/- 3.255	1.261 +/- 0.298	4.202 +/- 0.227	5.362+/- 0.489	5.84 +/- 0.484	6.494 +/- 0.520
400 US Grit	0.469 +/- 0.061	2.138+/- 0.067	1.342 +/- 0.133	2.755 +/- 0.024	2.253 +/- 0.085	1.602 +/- 0.107	1.980 +/- 0.253	1.527+/- 0.261	2.076 +/-0.266	2.591 +/- 0.168
600 US Grit	0.840 +/- 0.225	0.180+/- 0.068	2.705 +/- 0.648	0.215 +/- 0.105	0.397 +/- 0.132	1.478 +/- 0.376	1.023 +/- 0.347	0.611+/- 0.100	0.815 +/- 0.497	0.661 +/- 0.297
800 US Grit	2.631 +/- 0.135	2.697+/- 0.113	3.027 +/- 0.147	1.547 +/- 0.145	1.109 +/- 1.054	1.875 +/- 1.062	1.407 +/- 0.523	0.331+/- 0.239	2.050 +/- 0.733	1.411 +/- 0.151
3-micron	1.510 +/- 0.119	0.411+/- 0.021	0.394 +/- 0.286	0.780 +/- 0.377	1.262 +/- 0.190	2.029+/- 0.086	3.207 +/- 0.205	2.161+/- 0.224	1.068 +/- 0.120	0.939+/- 0.057

Table B. 2:The maximum and average pit depths differed among the groups, as received (control), 400 US Grit, 600 US Grit, 800 US Grit, and fine 3-micron diamond polished.

Copper Coupons	Max pit depths (µm)	Average pit depths (µm)
As Received (control)	6.413 -/+ 0.455	4.314 -/+ 0.86
400 US Grit	2.730 -/+ 0.040	1.874 -/+ 0.086
600 US Grit	2.162 -/+ 0.826	0.892 -/+ 0.707
800 US Grit	3.127 -/+ 0.199	1.809 -/+ 0.779
3-micron	2.623 -/+ 0.597	1.376 -/+ 0.834

SEM Images from Pitting Analysis

As-Received

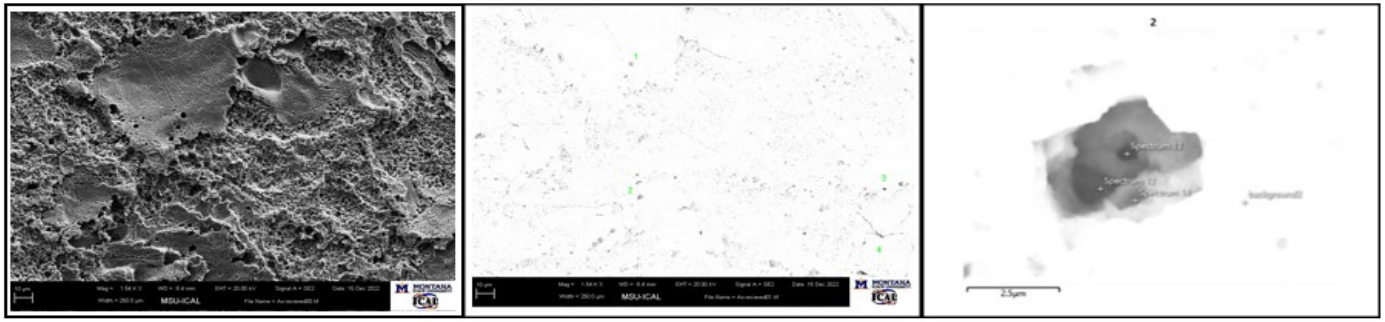


Figure B. 2: (Left) image was captured from an 600 US grit coupon. The brightness and contrast of this image were adjusted in order to identify the maximum pits, which are the darkest points in the center image. (Right) additionally, one of the pits was magnified to collect spectrums using EDX for further investigation of pitting.

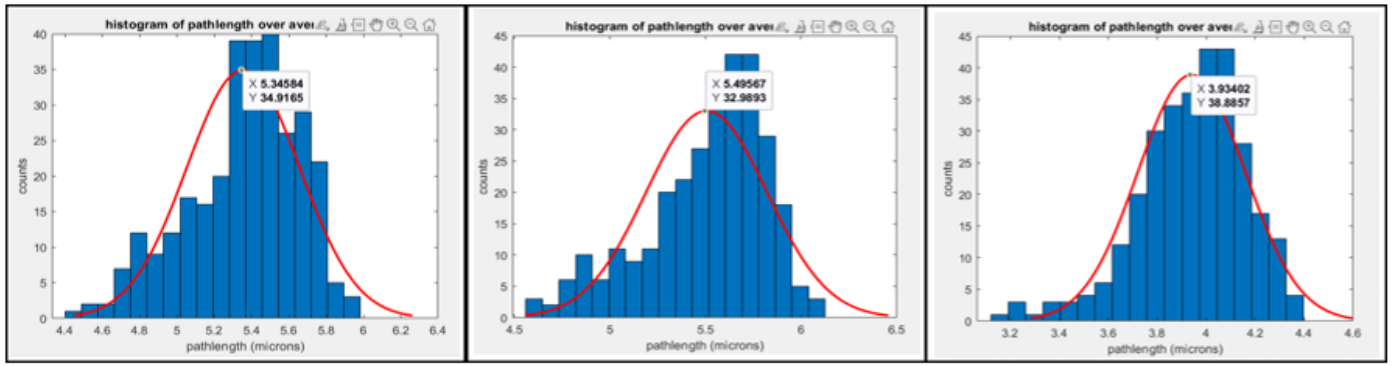


Figure B. 3: MATLAB was used to show measured pitting depths from a single pit. The X values represent pit depths from a spectrum. The first graph on the left was examined using spectrum 13, the center graph was from spectrum 12, and the right graph was from spectrum 14 in Figure B.2, right image.

400 US Grit

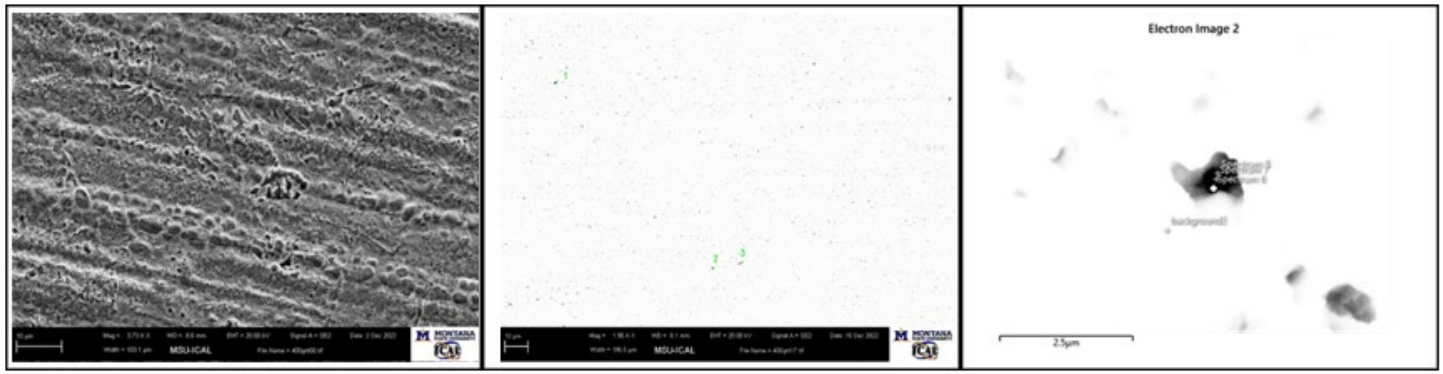


Figure B. 4: (Left) image was captured from an 400 US grit coupon. The brightness and contrast of this image were adjusted in order to identify the maximum pits, which are the darkest points in the center image. (Right) additionally, one of the pits was magnified to collect spectrums using EDX for further investigation of pitting.

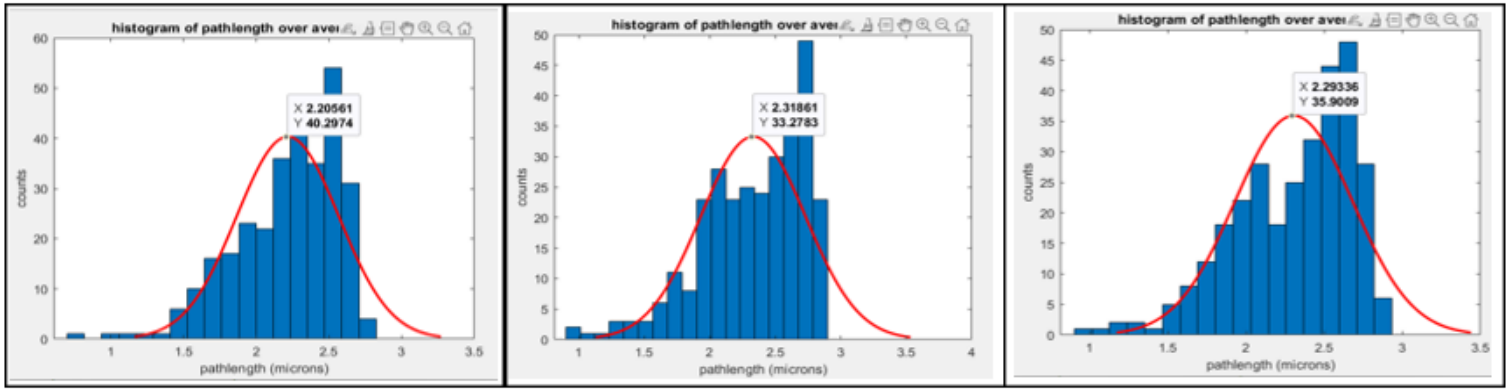


Figure B. 5:MATLAB was used to show measured pitting depths from a single pit. The X values represent pit depths from a spectrum. The first graph on the left was examined using spectrum 5, the center graph was from spectrum 7, and the right graph was from spectrum 6 above in Figure B.4, right image.

600 US Grit

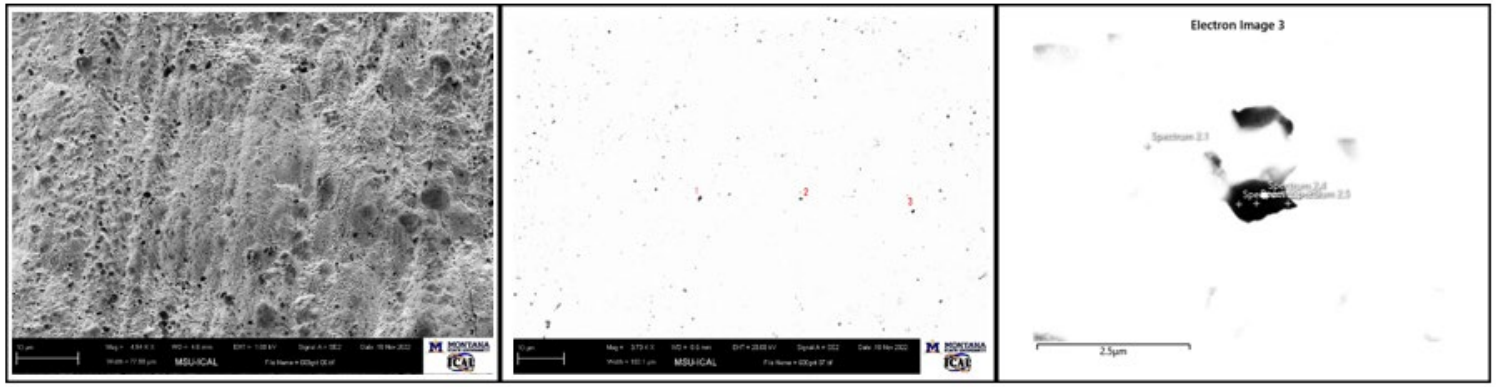


Figure B. 6:(Left) image was captured from an 600 US grit coupon. The brightness and contrast of this image were adjusted in order to identify the maximum pits, which are the darkest points in the center image. (Right) additionally, one of the pits was magnified to collect spectrums using EDX for further investigation of pitting.

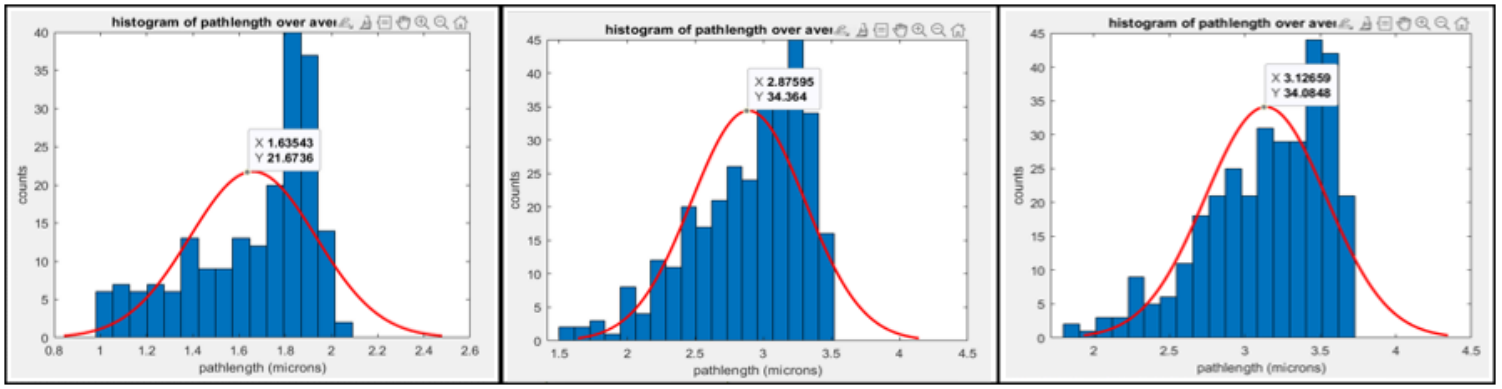


Figure B. 7: MATLAB was used to show measured pitting depths from a single pit. The X values represent pit depths from a spectrum. The first graph on the left was examined using spectrum 2.4, the center graph was from spectrum 2.3, and the right graph was from spectrum 2.5 in Figure B.6, right image.

800 US Grit

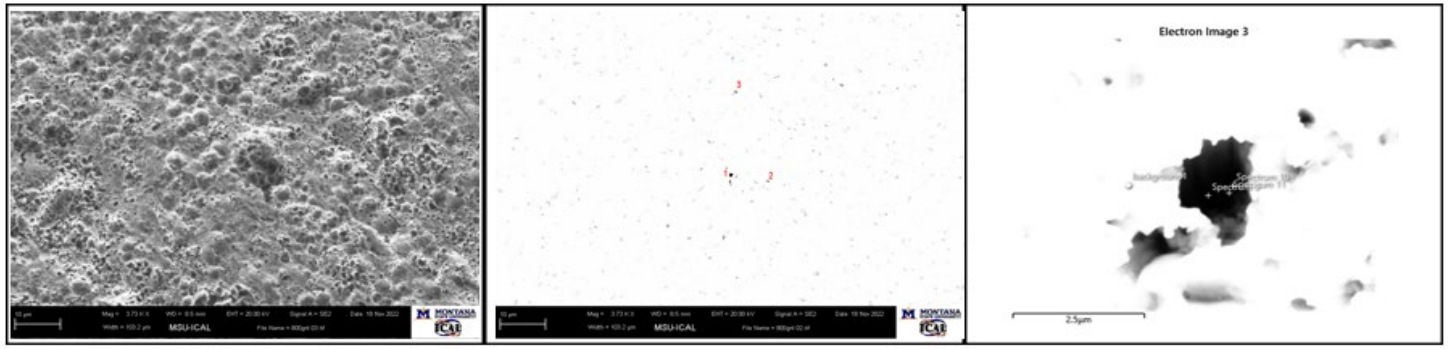


Figure B. 8: (Left) image was captured from an 800 US grit coupon. The brightness and contrast of this image were adjusted in order to identify the maximum pits, which are the darkest points in the center image. (Right) additionally, one of the pits was magnified to collect spectrums using EDX for further investigation of pitting.

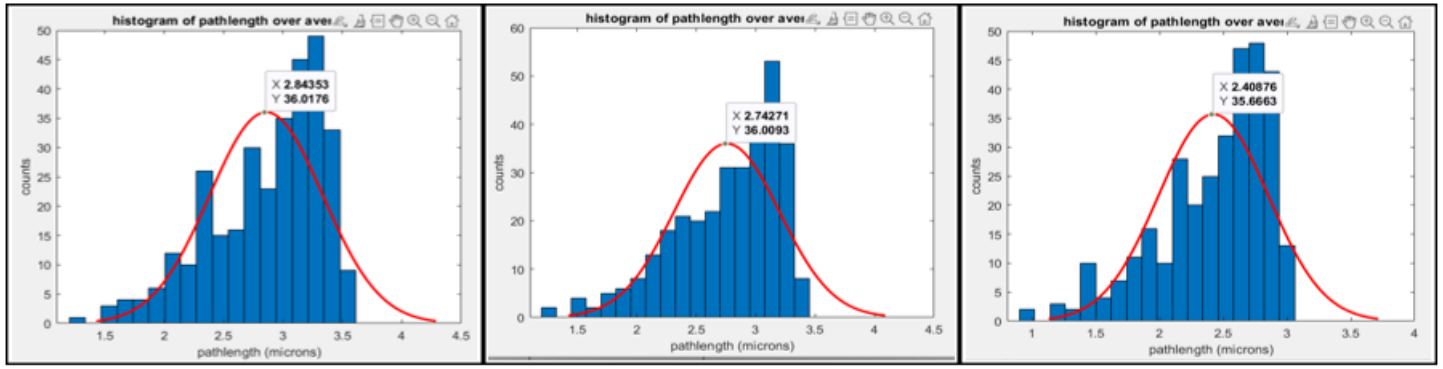


Figure B. 9: MATLAB was used to show measured pitting depths from a single pit. The X values represent pit depths from a spectrum. The first graph on the left was examined using spectrum 8, the center graph was from spectrum 11, and the right graph was from spectrum 10 in Figure B.8, right image.

3-micron Diamond Suspension

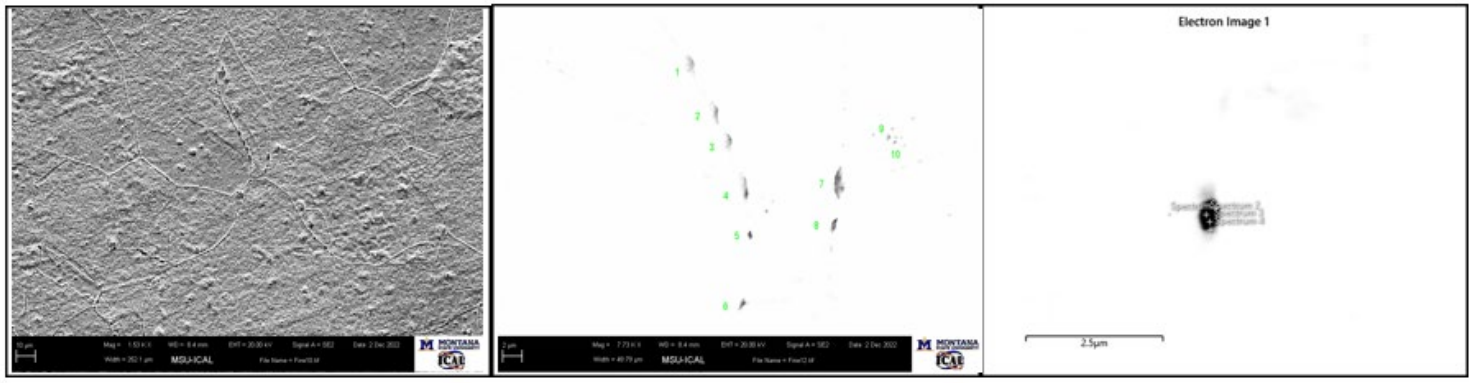


Figure B. 10: (Left) image was captured from an 3-micron diamond suspension surface finish. The brightness and contrast of this image were adjusted in order to identify the maximum pits, which are the darkest points in the center image. (Right) additionally, one of the pits was magnified to collect spectrums using EDX for further investigation of pitting.

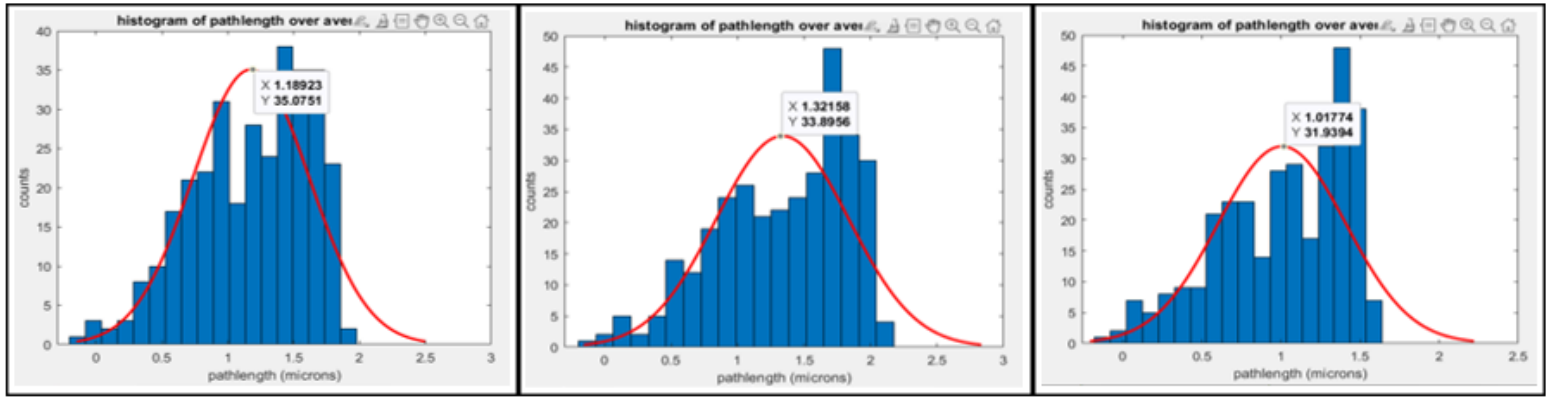


Figure B. 11: MATLAB was used to show measured pitting depths from a single pit. The X values represent pit depths from a spectrum. The first graph on the left was examined using spectrum 2, the center graph was from spectrum 3, and the right graph was from spectrum 4 in Figure B.10, right image.

APPENDIX C

CU(II) DISSOLUTION TO BALCH TUBES AND CDC REACTORS

Sigma Aldrich Copper Assay Kit (Catalog Number MAK 127) was used to measure copper ions dissolved in abiotic tubes. Once the coupons were placed into the medium tubes, 0.3 mL of sample was removed anoxically using a needle and 1 mL syringe from each tube as t_0 . Samples were collected every 8 hours for 48 hours, then every 24 hours until the end of the experiment. The absorbance (359 nm) of the samples was measured using a Thermo Scientific, Genesys 10S UV-VIS Spectrophotometer.

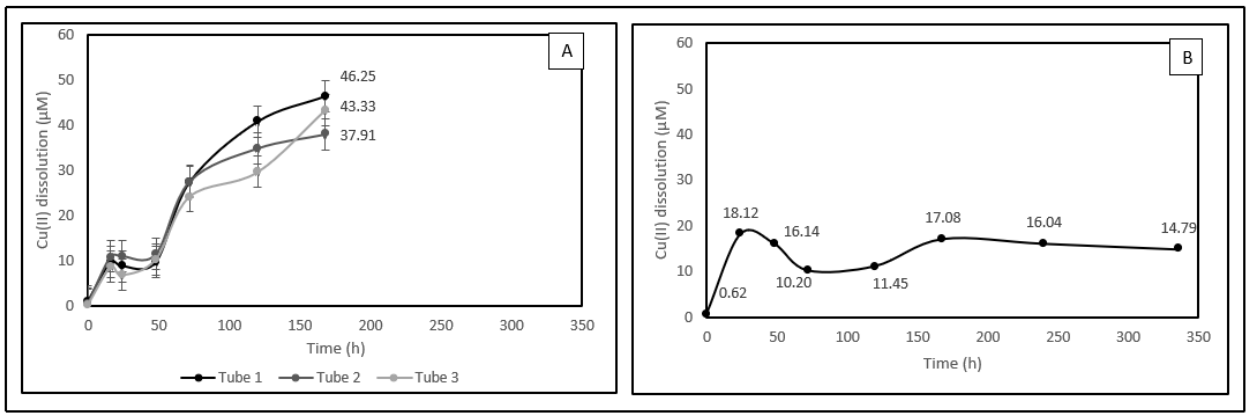


Figure C. 1:The dissolution of Cu(II) under abiotic static conditions was measured using two experimental setups: copper coupons with a total surface area of 1.52 cm^2 and 15 mL medium tubes (A), and a CDC reactor with a total copper surface area of 25.2 cm2 and 400 mL medium (B).

The copper dissolutions to medium (15 mL) in static abiotic systems were measured at an average of 42.5 µM from a total of 1.52 cm^2 copper surface. On the other hand, Cu(II) dissolutions were measured as approximately 15µM and 30 µM for experiment 1 and experiment 2 respectively. The protein numbers are changed depending on the copper coupon surface area to

Table C. 1: The comparison of Cu(II) dissolution (μM), Surface area of the coupons (cm^2), volume of medium (mL), Protein/surface area of biofilms and protein content of planktonic cells from the static condition.

Experiments	Coupon surface area (cm^2)	Volume (mL)	Surface area(m^2)/Volume(mL)	Cu(II) dissolution(μM)	Protein/surface area
Static condition	1.52	15	0.101	43	80.25 (planktonic)
CDC Exp1	25.2	400	0.063	15	203.57 (biofilm)
CDC Exp 2	56.4	400	0.141	30-35	114.42(biofilm)

APPENDIX D

BIOINFORMATICS STUDY

Biofilms in CDC reactors are formed more intense than in static condition. Also, it can be seen that the cell extension in the reactors comparing to static condition. This phenotypical change could be caused by genotypical changes. We know that flagellins known as hook proteins are expected to be up-regulated in reactors compared to static conditions since the flagellins play as a jointer between the cells and improve biofilm formations and intense biofilms were observed in the reactors. Our colleagues in the School of Mines, South Dakota observed G20 cell extension in static conditions (Kumar Tripathi, 2022). However, we haven't seen the cell extensions in static conditions. On the hand, we observed cell extension in the reactor biofilms. However, Cu(II) concentration in the reactors medium wasn't as high as in static conditions due to the flow. Because Cu(II) flows to the effluent.

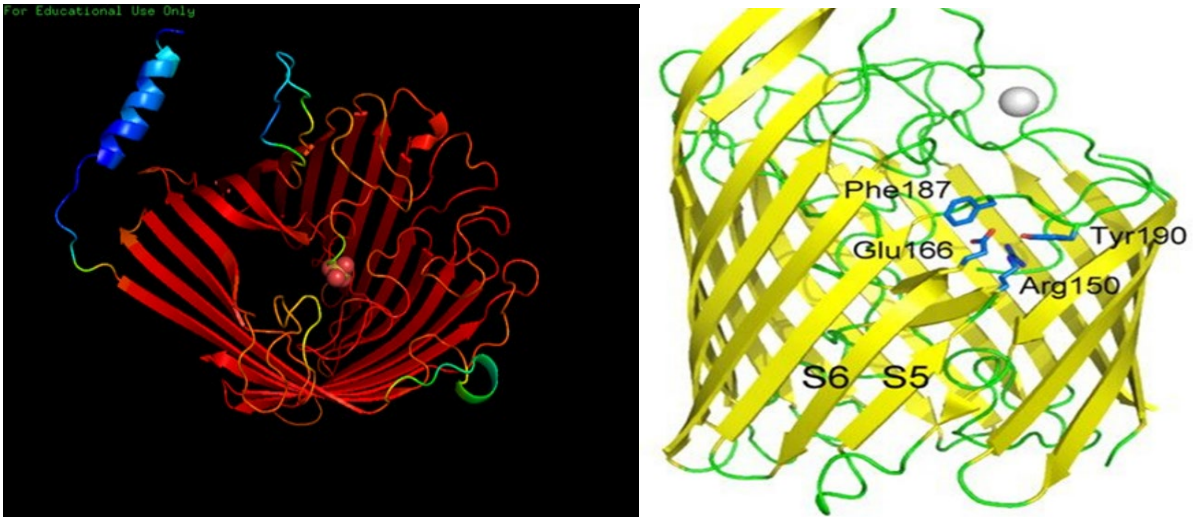


Figure D. 1 AlgE on G20 membrane modelled using Pymol (left), AlgE on Pseudomonas aeruginosa membrane(right), (Whitney, et al., 2011).

Diffusion of copper ions through the EPS matrix and active transport by bacterial cells are two important mechanisms for the transport of copper ions.The diffusion of copper into SRB biofilms is a complex process that is influenced by several factors. One of the most important

factors is the physicochemical properties of the biofilm matrix. The biofilm matrix is composed of extracellular polymeric substances (EPS), which are highly hydrated and contain many functional groups that can interact with metal ions. The EPS matrix can act as a barrier, slowing the diffusion of copper into the biofilm. However, the EPS matrix can also facilitate the diffusion of copper by promoting the formation of CuS and other copper-containing compounds. Copper is a common antimicrobial agent that is often used to control bacterial growth in various settings. However, the efficacy of copper is reduced in biofilms due to the presence of the EPS matrix, which acts as a barrier to copper diffusion. AlgE is a protein found in the EPS matrix of biofilms that has been shown to play a role in metal transport.

Dde_1010, a down-regulated and unfunctionalized protein (Kumar Tripathi, 2022) was functionalized as ALgE protein and could be responsible for biofilm formation and sulfate/copper transporter. The Dde_1010 protein was modeled by combining the results from different databases (Dali, microbes online, String), PyMol. Tyr190 and Phe 187 are unique residues to AlgE (Whitney, et al., 2011). These two conserved residues are linked to Dde_1010 using PyMol. Therefore, Dde_1010 was functionalized as AlgE. I anticipate that this protein should be down-regulated in the biofilms growing with high copper stress in CDC reactors due to the damage of G20 cells.